The proton, pion and omega final state produced by 11.7 Gev pions in hydrogen

Afzal, Muhammad

THE PROTON, PION AND OMEGA

FINAL STATE PRODUCED BY

11.7 GeV PIONS IN HYDROGEN

A thesis presented

by

Muhammad Afzal

for the

Degree of Doctor of Philosophy

at the

University of Durham

February, 1974

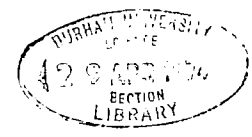

ABSTRACT

This thesis contains an account of the $p\omega\pi^+$ final state produced by the interaction of 11.7 GeV/c π^+ mesons in a bydrogen bubble chamber.

1 event for 4-prong DST = 0.17 μb.

The total cross sections for 4-prong $1C\pi^o$ events and for the $p\omega\pi^+$ final state respectively are 1.31 ± 0.13 mb and 0.134 ± 0.013 mb. These cross sections vary as a power of incident momentum with exponents of 0.82 and 1.41 respectively.

For the reaction $\pi^+p \longrightarrow \omega\Delta^{++}$, values of mass and width of the Δ^{++} and total cross-section $\sigma(\pi^+p \longrightarrow \omega\Delta^{++})$ respectively are 1234 ± 8 MeV/c^2, 122 ± 32 MeV/c^2 and 53 ± 10 μb. The cross-section decreases with the incident momentum as p_{inc}^{-n} with n = 1.85. The $d\sigma/d|t|$ and $d\sigma/d|t'|$ distributions show dips at $|t|$ (or $|t'|$) ≈ 0 and ≈ 0.6 (GeV/c)^2. The slope of the differential cross sections is ≈ 4 GeV^{-2}. The predictions on the density matrix elements disagree with the experimental results. There are dips at $|t|$ ≈ 0 and ≈ 0.5 (GeV/c)^2 for the natural parity contribution and a dip appears at $|t|$ ≈ 0.2 (GeV/c)^2 for the unnatural component. Most of the values of the double statistical tensors are compatible with zero. A qualitative theoretical discussion of the results is presented.

For the reaction $\pi^+p \longrightarrow pB^+$, values of mass, width and total cross-section of the B^+ respectively are 1235 ± 12 MeV/c^2, 120 ± 48 MeV/c^2 and 21 ± 6 μb. The cross-section decreases with the incident momentum as p_{inc}^{-n} with n about 1.5. The slope of the differential cross-section is ≈ 4 GeV^{-2}. The helicity amplitude for the ω^o, $|F_o|^2$ = 0.09 ± 0.07 which disagrees with the prediction of a simple quark model. The values of $\langle J_z^2 \rangle$ favour $J^P = 1^+$ or 2^+ but disfavour J = 3 for the B. Assuming $J^P = 1^+$ assignment, the density matrix elements show that the B^+ is weakly aligned both in the t-- and the s-channel helicity frames.

There is no evidence for the production of the higher mass Δ^{++} or higher mesons decaying into $\omega\pi^+$ or any resonance decaying into ωp.

PREFACE

This thesis is an account of the work carried out by the author whilst at the University of Durham and is concerned mainly with the $p\omega\pi^+$ final state produced by 11.7 GeV/c positive pions in hydrogen. The experiment described here is part of a larger experiment on the interaction of 11.7 GeV/c positive pions with protons which was being carried out by the High Energy Nuclear Physics Group of the University in collaboration with similar groups in Genova, Milano, Hamburg and Saclay. The author joined the Group after the initial exposure of the chamber and after a considerable amount of measurement of the film had been made and the data reduced.

The author has been concerned with the independent analysis of the $p\omega\pi^+$ final state with special emphasis to the quasi-two-body processes. The specific contributions by his collaborators are indicated in the text.

CONTENTS

LIST OF FIGURES

LIST OF TABLES

CHAPTER 1

STUDY OUTLINE AND DATA COLLECTION

1.1 Introduction

The existences of almost all the elementary particles have been established by observing the results of collisions of those already known, with nuclear targets, the most useful and easily used target being the proton. The current measurements of the intrinsic properties of the known particles are summarised in data tables [1]. Besides the photon, the particles divide naturally into a small group called leptons (electrons, muons and neutrinos) which interact through the weak interaction and a very large group called hadrons which interact through strong nuclear forces. The experimental study of π^+ meson collisions on protons in this thesis is concerned with six types of known hadrons, the pion, proton, ω^o and ρ mesons, the B meson and Δ baryon. The relevant properties are summarised in Table (1.1).

Table (1.1)

The particle properties

Particle	Mass(MeV)	τ(sec)	Γ(MeV)	Spin	Parity	Isospin(I)	G-Parity
$\pi^{\pm}$-meson	140	2.6×10^{-8}	0	0	-	1	-
π^o-meson	135	$\sim10^{-16}$	7.8±0.9eV	0	-		-
ρ-meson	770±5	-	146±10	1	-	1	-
ω^o-meson	783.8±0.3	-	9.8±0.5	1	-	0	-
B^+-meson	1237±10	-	120±20	1	+	1	+
Proton(p)	938	∞	0	1/2	+	1/2	
Δ^{++}	1230-1236	-	110-122	3/2	+	3/2	

The proton and the π mesons have long enough lifetimes for their direct detection to be possible. The ω^o and B^+ mesons and the Δ^{++} are hadrons for which strong decay channels to other hadrons are possible with lifetimes $\sim 10^{-23}$ sec. and hence no apparatus is capable of detecting them directly. They decay respectively as:

$$\omega^o \longrightarrow \pi^+\pi^-\pi^o \quad (\sim 90\%) \text{ ,}$$
$$\longrightarrow \pi^o\gamma \quad (\sim 10\%) \text{ ;}$$
$$B^+ \longrightarrow \omega^o\pi^+ \text{ ;}$$
$$\Delta^{++} \longrightarrow p\pi^+ \text{ .}$$

The very short lifetimes imply that the masses of these particles should not have sharply defined values. The mass distribution takes the form of a Breit Wigner function (see Section 2.3) and hence such unstable particles are usually called resonances. In Table (1.1) it is the full width at half height (Γ) of the Breit Wigner function corresponding to the resonance that is entered rather than the life-time (τ). The intrinsic parity of a hadron is important since the net parity of a system of colliding hadrons is conserved in strong interactions. The same is true of the isospin I and G-parity which are listed in the table. The total charge multiplicity of a particle is (2I+1). The other conserved quantum numbers, baryon number and hypercharge, which are useful to assign to hadrons are not listed in the table.

Experimentally the resonances cannot be detected directly. The basic interaction being studied in this thesis is:

$$\pi^+p \longrightarrow p\omega^o\pi^+ \text{ .}$$

The ω^o meson, however, decays instantaneously as far as any apparatus is concerned mainly into three pions ($\pi^+\pi^-\pi^o$). Hence the reaction that is detected appears as:

$$\pi^+ p \longrightarrow p\pi^+\pi^+\pi^-\pi^o .$$

With such a multiplicity of particles in the final state, the detecting system either has to be a high complex spark chamber array or as in the present case, a hydrogen bubble chamber.

Any experiment in high energy physics these days is likely to take a number of years to complete. A bubble chamber experiment requires teams of experts to operate the chamber, and design the beams of particles to which it is exposed. The extraction of data and its analysis is normally carried out by collaboration of many people working in different institutions. The author joined the team† working on the present experiment after the initial exposure of the chamber and after a considerable amount of the film had been measured and the data reduced. The rest of this Chapter is devoted to a summary of the process that results in obtaining data from a film analysis system with particular reference to that used in Durham. In the later chapters the detailed independent analysis done by the author of the $p\omega^o\pi^+$ final state produced by 11.7 GeV/c π^+ mesons colliding with protons is presented. A number of the results obtained in the thesis have already been published [2,3] by the collaborating laboratories, and there are sometimes differences between the two sets. These differences are never large enough to consider either determination of a quantity to be erroneous, and should rather be taken as an illustration of the variation that occurs when two different but equally reasonable schemes of analysis are applied to the same raw data. A comparison table of the published results and those obtained in this thesis is given in Appendix A.

---

†This was a collaboration of members of laboratories in Genova, Milano, Hamburg, Saclay and Durham.

1.2 The Beam, Bubble Chamber and Film Production

The exposure of the CERN 2m hydrogen bubble chamber to 11.7 GeV/c positive pions took place in July, 1966, using the U_3 beam at CERN. About 180,000 pictures were taken for this experiment.

In this Section the U_3 beam, the bubble chamber and the film production will be described.

1.2.1 The U_3 beam

The U_3 beam was constructed in the east experimental area of the CERN proton synchroton to supply the CERN 2m hydrogen bubble chamber with reasonably pure beams of pions and kaons at different momenta up to 20 GeV/c. The beam uses RF separators because they are more effective at higher incident energies such as in this experiment. The beam can be divided into three stages. Firstly, the particles lying within a particular momentum range are selected. Secondly, the mass analysis is done and lastly the momentum is redefined before entry into the chamber.

The detailed description of the beam is given by Lazeyras, P. [4] and Bernard et al. [5]. A brief description is given below. The layout and schematic diagram of the 165.5 m long beam is shown in Fig. (1.1). The protons in the synchroton at about 20 GeV/c are extracted by fast ejection and impinge on a copper target of dimensions 2x1x150 mm^3. The angular acceptance is defined by the horizontal and vertical collimators, C_1 and C_2. The four lenses Q_1-Q_4 focus the beam on to the collimator C_4 and give it sufficient magnitification in the vertical plane to give it an angular opening of about 1 mr in the centre of RF_1 separator. The collimator C_3 defines the vertical angular acceptance. The components B_1, B_2, C_4, Q_5, B_3 and B_4 produce a momentum-analysed and dispersion-free beam. The momentum analysis

SCHEMATIC DIAGRAM OF U_3 BEAM LAYOUT

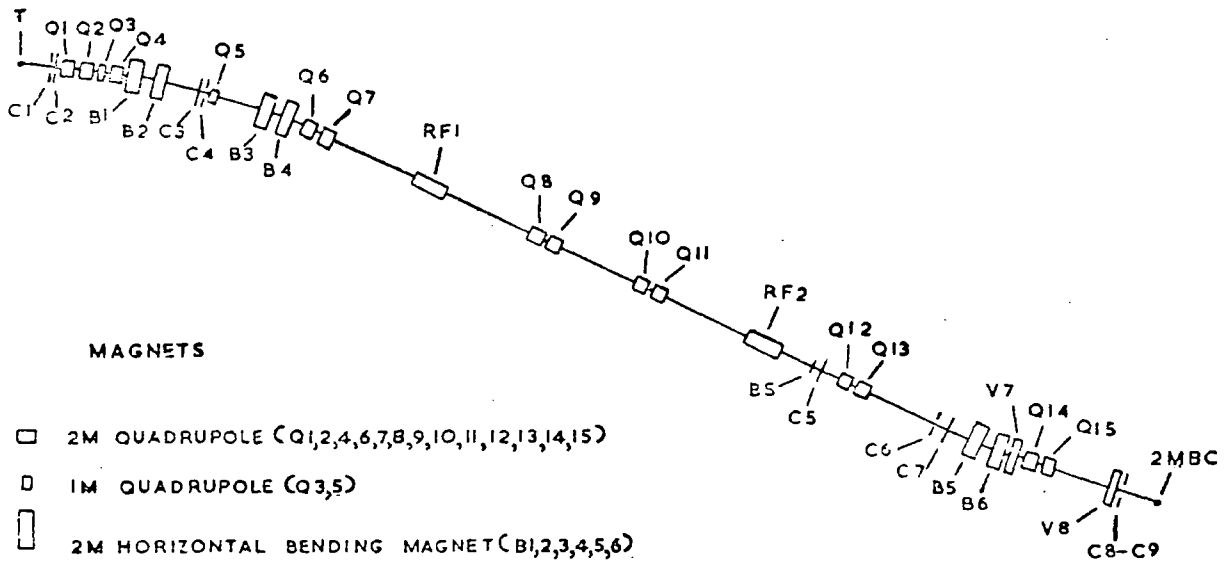

MAGNETS

- 2M QUADRUPOLE (Q1,2,4,6,7,8,9,10,11,12,13,14,15)
- 1M QUADRUPOLE (Q3,5)
- 2M HORIZONTAL BENDING MAGNET (B1,2,3,4,5,6)
- 1M VERTICAL BENDING MAGNET (V7,8)

COLLIMATORS

- HORIZONTAL COLLIMATOR (C1,4,6,8-9)
- VERTICAL COLLIMATOR (C2,3,5,7)
- BEAM STOPPER (BS)

SEPARATORS

- RADIOFREQUENCY SEPARATOR (RF1,2)

T = TARGET

BC = BUBBLE CHAMBER

FIG. 1.1

takes place at C_4, called the momentum slit. The quadrupole Q_5 acts as a field lens and B_1, B_2, B_3 and B_4 are the bending magnets.

The doublet Q_6-Q_7 images the target in both the horizontal and the vertical planes at the first RF cavity RF_1. The two doublets Q_8-Q_9 and Q_{10}-Q_{11}, placed between RF_1 and RF_2, produce the images in RF_2.

In RF_2 the deflection of unwanted particles is cancelled by deflection in the opposite direction while that of wanted particles is doubled by choice of a suitable phase difference as they travel between RF_1 and RF_2. The unwanted particles are thus stopped by the beam stopper. In practice the height of beam stopper is made somewhat bigger than the theoretical value to account for imperfections and tolerances in the system. The section of the beam following RF_2 redefines the momentum and refocusses the beam. Finally, the vertical magnets V_7 and V_8 steer the beam into the bubble chamber.

1.2.2 The bubble chamber

Figure (1.2) shows the CERN 2-metre bubble chamber where the exposure took place. It consists of aluminium casting of dimensions $200 \times 51 \times 60 cm^3$ with front and back windows of plane glass. It was filled with liquid hydrogen for this experiment, under a pressure of about 6 atmospheres and at a temperature of about $27^{\circ}K$ which is just sufficient to prevent boiling.

The chamber is surrounded by large electromagnets which maintained an almost uniform magnetic field of about 17 Kgauss throughout the chamber. The magnetic field is normal to the windows of the chamber.

The four cameras in different positions are arranged to photograph the chamber. Fiducial marks are engraved on the inner

2 METRE C.E.R.N. BUBBLE CHAMBER (HORIZONTAL SECTION)

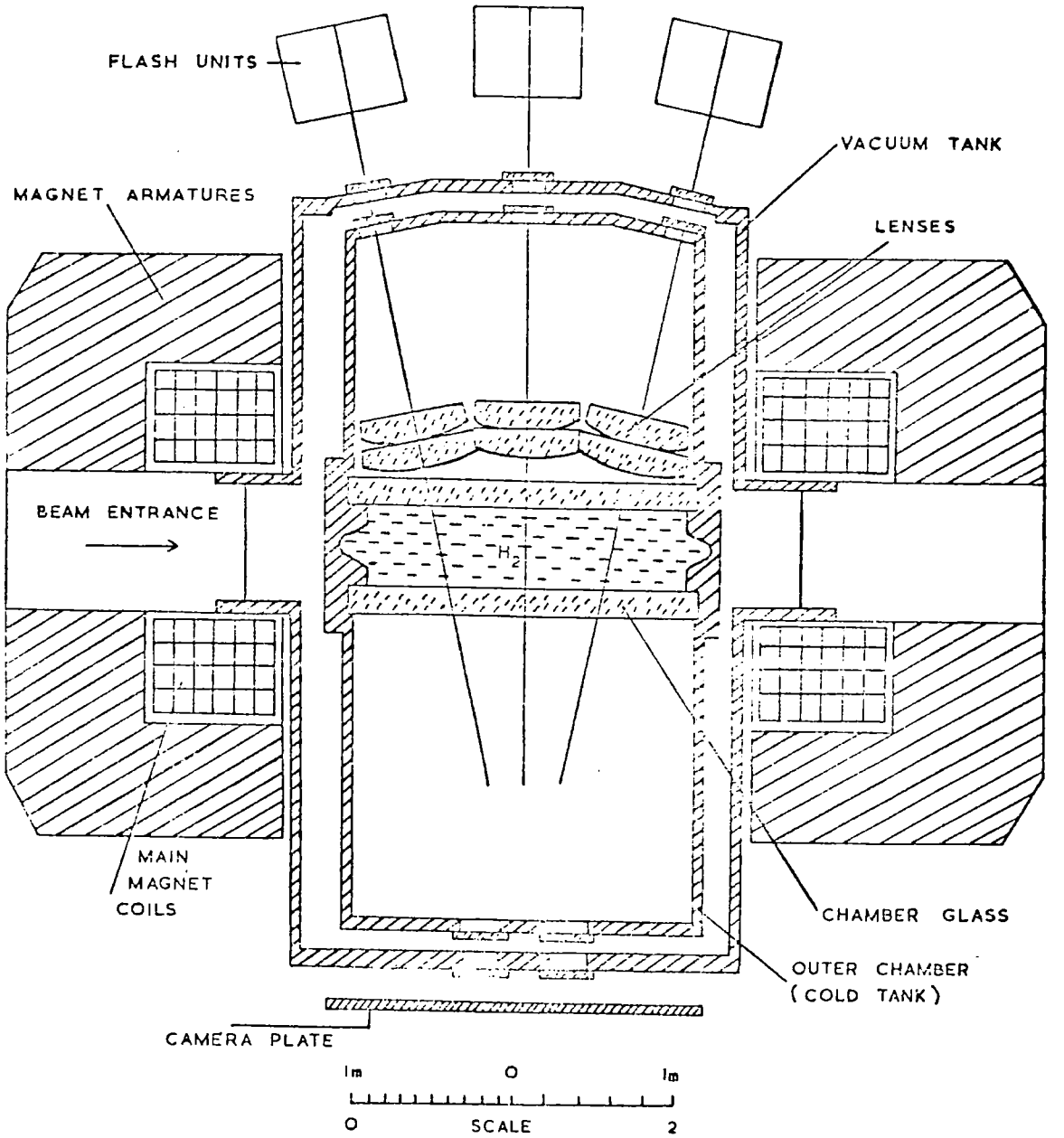

FIG. 1.2

sides of the front and back windows and these provide a coordinate system independent of the photographic system.

The through illumination uses three flash tubes with filters for wavelengths in the range 4200-4600Å.

The four cameras are mounted in an array with their axes perpendicular to the chamber windows and their positions are localised as shown in Fig.(1.3). The average focal length of objectives is 182.3 mm with an aperture of f/32 which gives a depth of focus covering the whole chamber from front to back.

Each camera sees through a set of three windows arranged in such a way that the total deviation of light is not more than 0.15±0.1 mr.

1.2.3 The film production

The operation cycle as shown in Fig.(1.4) is designed such that the charged particles passing through the chamber leave a trail of bubbles to be photographed.

Initially the pressure is kept just sufficient to prevent the boiling of liquid and when it is suddenly reduced from 6.5 to 2.8 atmospheres, the liquid (hydrogen in this experiment) is superheated. The timing of the expansion cycle is so arranged that the beam of particles from the accelerator is allowed to enter the chamber when the pressure is minimum and the chamber is most sensitive. They cause ionisation and spontaneous boiling is produced along the path of the particles. The flash is delayed by about a millisecond to enable the bubbles to grow to a suitable size to be photographed. When the trail of bubbles grows to the size of about 200μ in diameter, the chamber is illuminated and photographed.

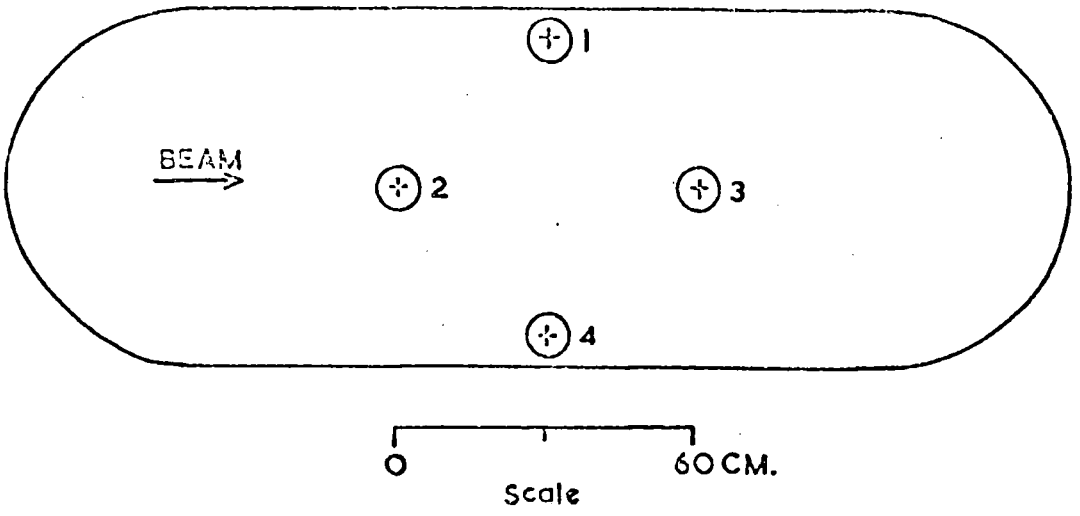

FIG. 1.3 CAMERA POSITIONS OF THE CERN 2-METRE CHAMBER.

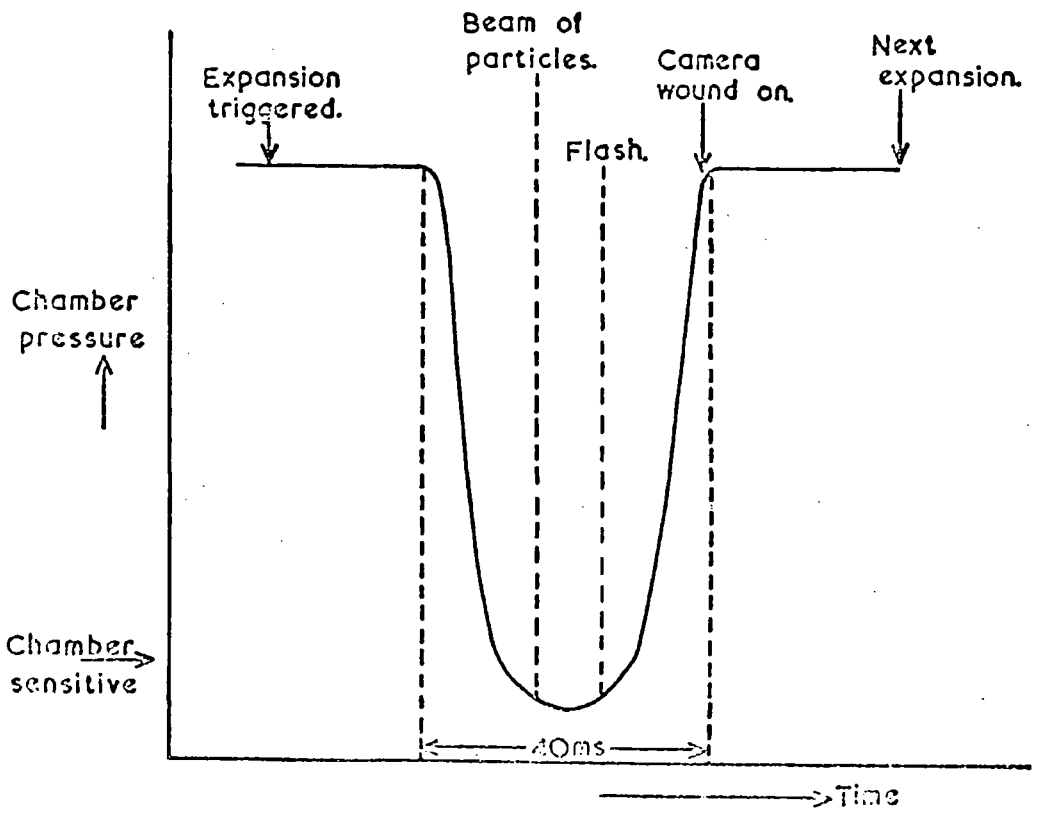

FIG. 1.4 OPERATION CYCLE FOR THE BUBBLE CHAMBER.

The cameras are wound on and the pressure is increased again for the bubbles to condense for the next cycle to be repeated after every machine pulse (e.g., two seconds in this experiment).

The bubble chamber operated for a week can produce 100,000 to 200,000 pictures for subsequent analysis.

1.3 The Film Analysis System

Fig.(1.5) shows the flow diagram for the film analysis system as used in Durham for the experiment. Equivalent systems were used by the collaborating laboratories.

An experiment of this type involves hundreds of thousands of pictures (e.g., 180,000 in this experiment), hence a somewhat automated system is necessary. The different steps involved are briefly described in this Section.

1.3.1 Scanning

Of the three views of one exposure of the chamber one was scanned, the other two being used as a check and a record was kept of the location and prong number of the events and any special features. The prong number of an event is determined by the number of secondaries leaving the interaction.

The film was scanned twice and the two lists of events thus obtained were compared for determining efficiency. For the four-prong events used in this thesis the efficiencies were high, being 99%.

1.3.2 Measuring

The measuring machines were manually operated. The film was moved, the movement being digitised, so that the enlarged image

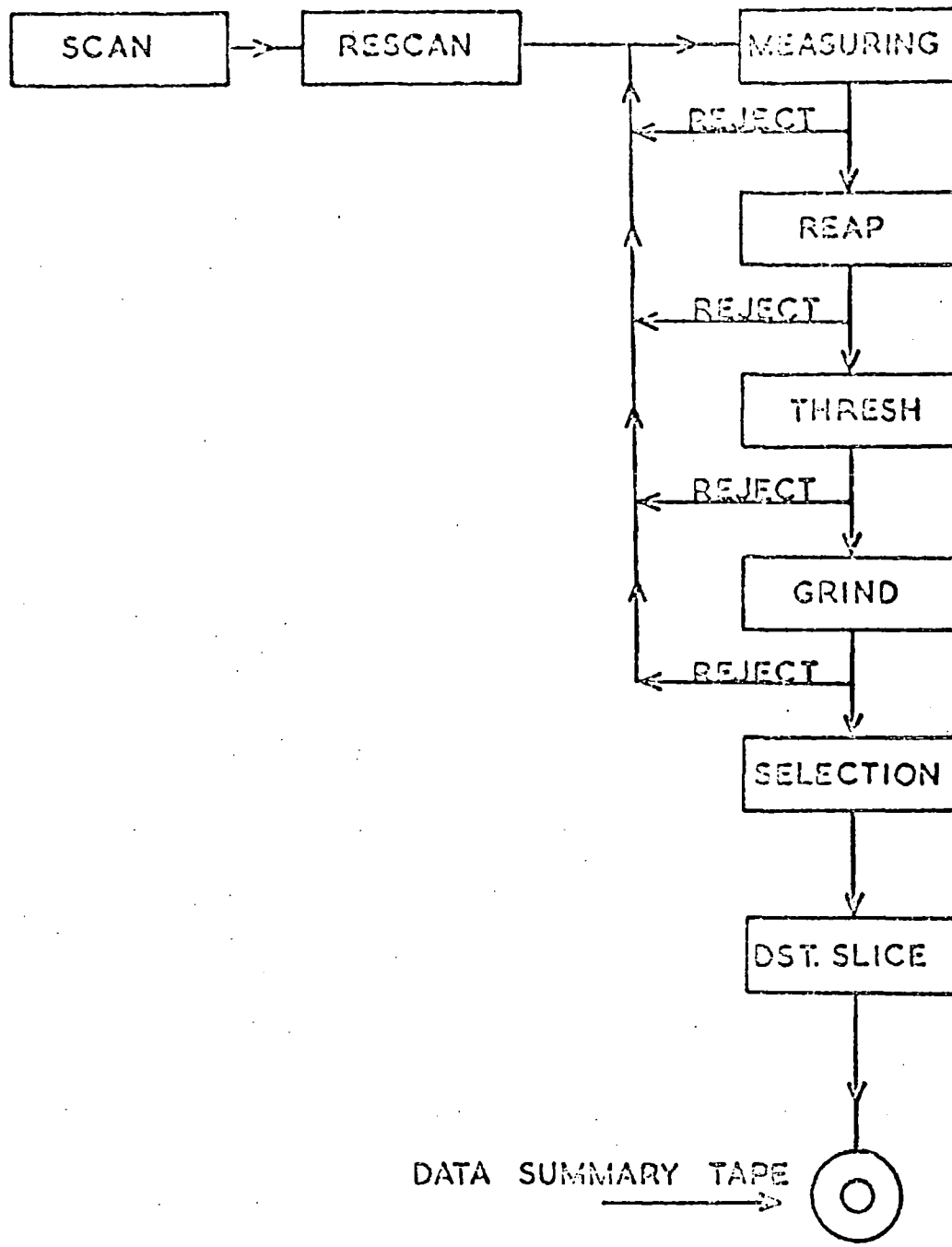

FIG. 1.5 FLOW DIAGRAM FOR THE FILM ANALYSIS.

projected on to a screen swept past a fixed mark on the screen. Such a machine is called a film plane digitiser. The x,y co-ordinates and other relevant information were stored on a magnetic disc. †

The measurement of two views of a track are sufficient for a three-dimensional reconstruction in chamber space provided the track does not lie along the optic axis of either of the cameras. To avoid such a situation three views were measured thus ensuring at least two good views for each track.

The coordinate system of measurements was determined by measuring four fiducial marks — two each on the front and the back windows of the chamber.

Usually nine points were measured for each track in each view. For very short tracks only the end point was measured. Thus for a simple two-prong event about 100 coordinate pairs are recorded and a four-prong event requires 150 measurements. These measurements are listed in Table (1.2).

Table (1.2)

Coordinate measurements for two- and four-prong events in each view

Measurement	Two-prong Events	Four-prong Event
Fiducial marks	4	4
Apex	1	1
Beam track	9	9
Secondary tracks	18	36
Total	32	50

†For the first part of the experiment, measurements were actually stored on paper tape, but the subsequent flow of information was of course the same.

The stored coordinate information was then processed by a programme (REAP) to put it in a form suitable for input to the programme THRESH. The data from THRESH were then processed by a programme called GRIND.

1.3.3 THRESH and GRIND

THRESH is a geometry programme of the CERN TC library which reconstructs from the measurements the geometry of the events in space. It checks up the measurement of each view in turn and then examines the fiducial measurements whether or not they lie within the permitted tolerance. A circle was fitted to the measurements of nine or so points for each track in a view (i.e., in projection). The two best fitted circles were then used to reconstruct each track as a helix in the three-dimensional chamber space and the third circle, if measured, was used for checking.

Thus after operation of THRESH one had the space trajectories and hence curvatures of particle tracks, to determine their momenta, but not the nature of the particles. So various hypotheses were tried to fit the experimental measurements using the conservation laws. For example, the four-prong events were kinematically fitted to the following three reactions:

$$\pi^+ p \longrightarrow p\pi^+\pi^+\pi^-,$$

$$\pi^+ p \longrightarrow p\pi^+\pi^+\pi^-\pi^o,$$

$$\pi^+ p \longrightarrow n\pi^+\pi^+\pi^+\pi^-.$$

GRIND is the CERN TC programme which was used to do this kinematic fitting.

Each event must satisfy the four constraint equations of energy and momentum at the interaction .

$$\left.\begin{aligned}
\Sigma P_x &= \sum^{n} (P_i \cos\lambda_i \cos\phi_i) - P\cos\lambda\cos\phi \longrightarrow 0, && \text{(a)}\\
\Sigma P_y &= \sum^{n} (P_i \cos\lambda_i \sin\phi_i) - P\cos\lambda\sin\phi \longrightarrow 0, && \text{(b)}\\
\Sigma P_z &= \sum^{n} (P_i \sin\lambda_i) - P\sin\lambda \longrightarrow 0, && \text{(c)}\\
\Sigma E &= \sum^{n} \sqrt{P_i^2 + m_i^2} - \left(\sqrt{P^2 + m^2} + M\right) \longrightarrow 0, && \text{(d)}
\end{aligned}\right\} \quad (1.1)$$

where P, λ, ϕ and m respectively are the momentum, dip, azimuth and mass of the beam particle. P_i, λ_i, ϕ_i are the corresponding quantities for the outgoing particle i and M is the mass of target. The particle momenta were determined from the track curvatures using the known magnetic field. A stopping particle's momentum was obtained from the range-energy relations.

The method of least squares is used to reduce ΣP_x, ΣP_y, ΣP_z and ΣE to a predetermined limit of, in this case, 0.0005 GeV, i.e., χ^2, given below, is minimized.

$$\chi^2 = \sum_i \frac{(X_i - \bar{X}_i)^2}{\Delta X_i^2}, \quad (1.2)^{\dagger}$$

where $\bar{X}_i$ is the measured quantity, X_i is the fitted quantity and ΔX_i is the error on X_i.

---

† Since there are correlations between the measurements, equation (1.2) is approximate. The more general analysis used by THRESH and GRIND, using matrix notation is briefly as follows[6].

Let G^{-1} be the full error matrix where $(G^{-1})_{ii}$ is the variance of the ith measurement and $(G^{-1})_{ij}$ is the covariance between the ith and jth measurements. The inverse, G, of the full error matrix is called a weighting matrix. Then equation (1.2) becomes:

$$\chi^2 = \sum_{j=1}^{J} \sum_{i=1}^{I} (X_i - \bar{X}_i)\, G_{ij}\, (X_j - \bar{X}_j) .$$

When no neutral particle is involved in the final state, all the variables are constrained and there are four degrees of freedom and the fit is called a '4C-fit.' When a neutral particle of assigned mass is missing, the first three equations (1.1 a-c) are used to solve for P_i, λ_i, ϕ_i and the fourth one is used for a constraint. There being one degree of freedom, the fit is known as a '1C-fit.' When more than one particle is missing there are more unknowns than the constraint equations and thus the fit cannot be done. Events rejected by THRESH or GRIND were remeasured and reprocessed. The final pass rate was 90%.

1.3.4 Ionisation check and data summary tape

All events successful in GRIND were examined on the scanning table to check whether the ionisation (bubble density) seen for a track was compatible with the requirements of the hypothesis.

It has been shown by several workers[7-9] that experimentally the bubble density, D, (i.e., number of bubbles per unit of track) is inversely proportional to the square of the particle velocity, β provided $0.5 < \beta < 0.8$ for heavy liquids and up to $\beta \sim 0.97$ for hydrogen. Thus

$$D = D_o/\beta^2, \qquad (1.3)$$

where D_o is the minimum value of ionisation (i.e., for beam tracks). The momenta of the pion and proton corresponding to $\beta \sim 0.97$ are 0.57 GeV/c and 3.8 GeV/c respectively.

Fig. (1.6) shows the relative bubble density against the momentum for three particles, i.e., pion, kaon and proton. In the present experiment an estimate of bubble density by eye leads to pions and proton indistinguishable above about 1.2 GeV/c. This is

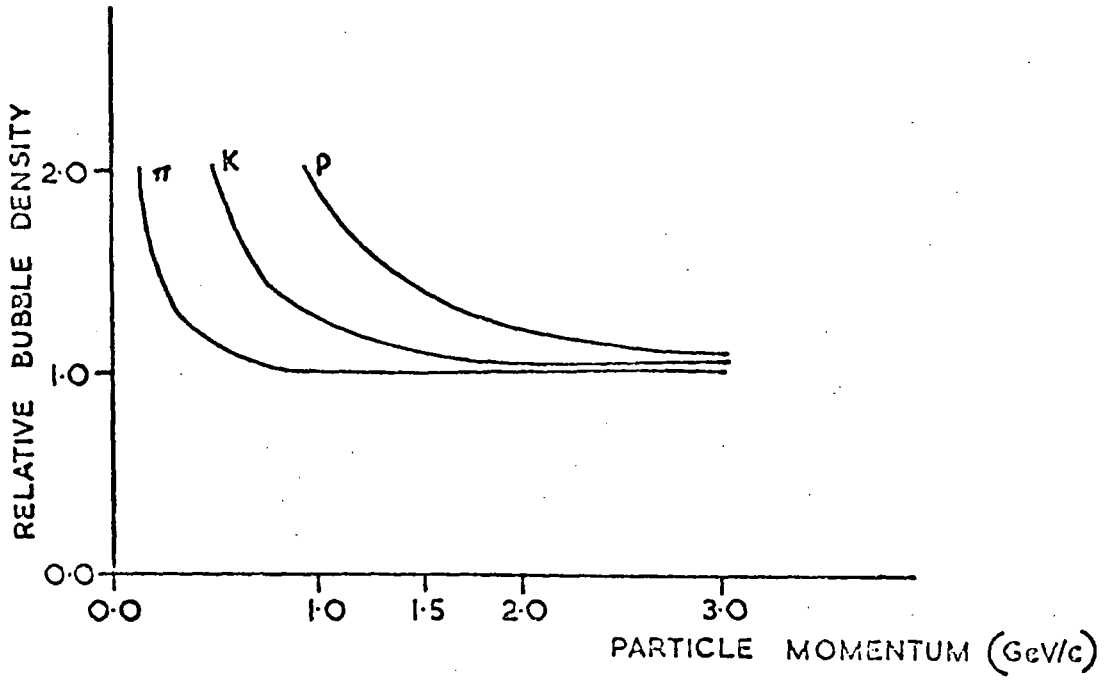

FIG. I.6 THE RELATIVE BUBBLE DENSITY VS. THE PARTICLE MOMENTUM (PION, KAON AND PROTON)

illustrated by the proton momentum distribution of $1C\pi^o$ events ambiguous with 1Cn and of those for which two $1C\pi^o$ hypotheses fitted. There is a sharp cut off at about 1.2 GeV/c. Therefore, it is concluded that protons and pions were in practice distinguished below 1.2 GeV/c for this experiment.

All hypotheses compatible with the ionization code were accepted. There is, of course, a class of events which do not fit any of the hypotheses tried. These are called 'no-fit' events† and could be examples of multi-neutral particle production, for example:

$$\pi^+ p \longrightarrow \pi^+ p\, \pi^+\, \pi^-\, \pi^o\, \pi^o,$$

or

$$\pi^+ p \longrightarrow \pi^+\, \pi^+\, \pi^+\, \pi^-\, \pi^o\, \pi^o.$$

The data summary tapes (DST) were prepared from the GRIND output. The DST contains the selected events, hypotheses and kinematic information such as angles and momenta and statistical information such as the confidence level of the fitted hypothesis (normally called χ^2-probability or $P(\chi^2)$).

1.4 Checks on the DST

The distributions of errors on curvature, dip and azimuthal angles as given by THRESH are normally distributed. The fits to the different hypotheses for an event as obtained by GRIND using the extra information in the form of constraint equations (1.1) should yield kinematic quantities which are closer to the truth than the original measurements. This will be true if no systematic errors of measurement have been made. In order to check this, the pull

---

† No hypotheses fitting the strange particle production were tried. They also contributed towards no-fit events.

distributions, as defined below, were plotted for each fitted hypothesis.

$$\text{Pull} = \frac{Q_u - Q_f}{\sqrt{\sigma_u^2 + \sigma_f^2}} , \qquad (1.4)$$

where Q_u and σ_u respectively are the unfitted quantity and its standard deviation and Q_f and σ_f are the corresponding quantities for the fitted values. The pull distribution should be a Gaussian around zero with a standard deviation of one. The pull distributions for curvature, dip and azimuthal angles were plotted for all the laboratories concerned and small adjustments were made to the information on errors submitted to GRIND, for those quantities where the width of the relevant pull distribution was not unity. No indication for the presence of large systematic errors in measurement was obtained.

Each collaborating laboratory produced its own DST containing the relevant information in the appropriate format. The compatibility of data on the DSTs of different laboratories was checked [10].

The χ^2-proability ($P(\chi^2)$) for a true sample of a particular class of events, such as 4C, $1C\pi^o$, etc. is expected to be flat. But the fit cannot sometime resolve between 4C and $1C\pi^o$ events. Therefore ambiguities arise where the same measurements are simultaneously compatible with two or more hypotheses. How these ambiguities have been treated in the present work is discussed in Sections 3.2 and 3.3.

Figure (1.7) shows $P(\chi^2)$ distribution for 4-prong $1C\pi^o$ events. It is almost flat for $P(\chi^2)>0.1$ but for $P(\chi^2)<0.1$, it is strongly peaked. This is due to the possibility that within measurement errors, the data obtained for some events can be consistent with a single missing π^o-meson even if the events are due to other processes such as two missing π^o mesons. For example, the error on MM^2 (square of the missing mass) is distributed between $5M^2_{\pi o}$ and $15M^2_{\pi o}$ and hence the no-fit background may also contribute towards the lower $P(\chi^2)$ events.

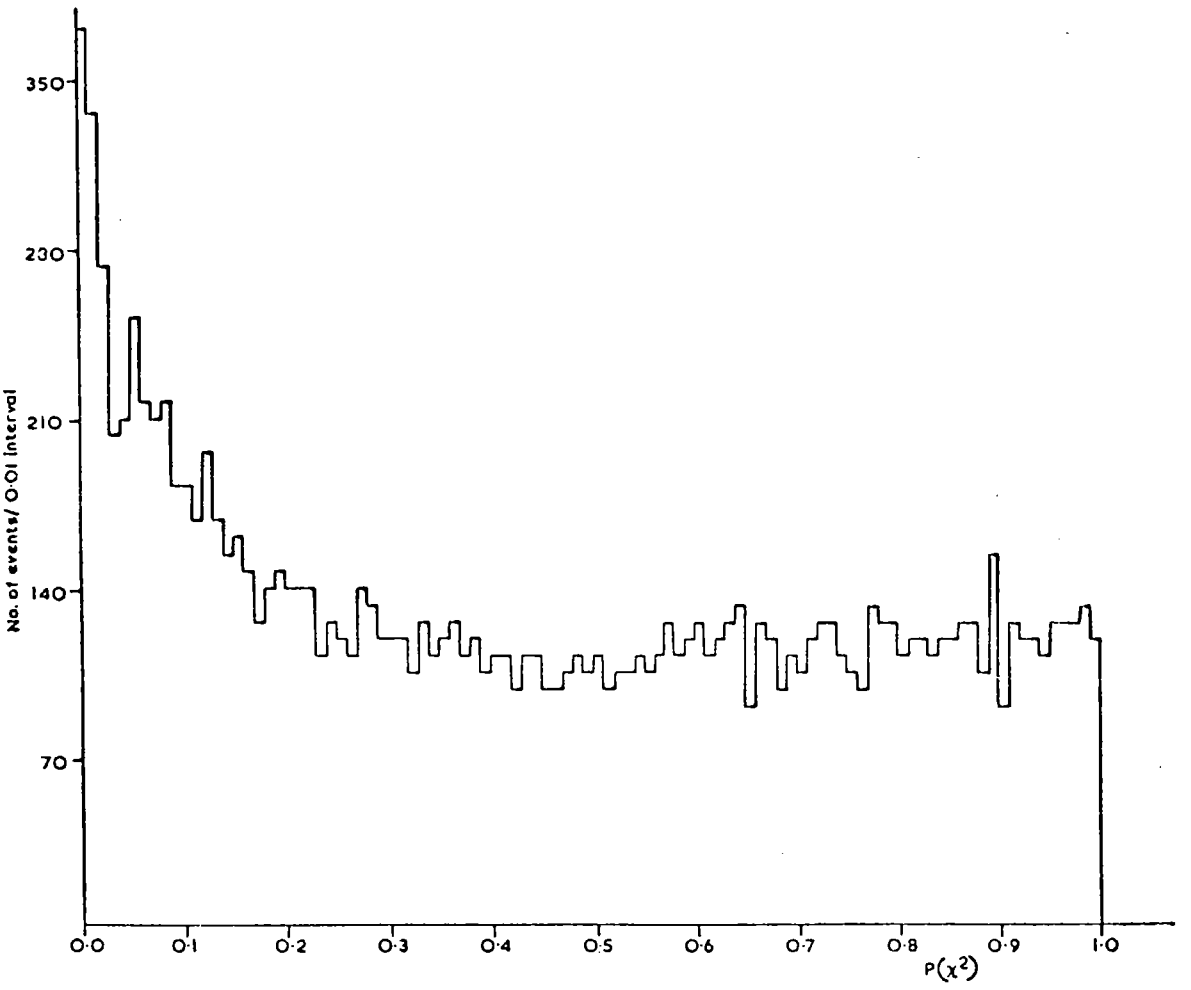

FIG. 1.7 χ^2– PROBABILITY $(P(\chi^2))$ DISTRIBUTION FOR 4-PRONG IC π^0 EVENTS — 13,372 EVENTS.

Fitted as single π^o-production events the confidence levels would no longer be expected to lie uniformly between 0 and 1 in probability, but in general would tend to be small. In the present work, in general, $P(\chi^2)$ has been taken >0.1 (see Section 3.3.1).

CHAPTER 2

THE BASIC MEASUREMENTS OF QUASI-TWO-BODY INTERACTIONS

2.1 Introduction

The term quasi-two-body interaction is applied to a channel that can be interpreted as being

$$a + b \longrightarrow c + d.$$

Here, a and b denote the particles that collide (in the present study a π^+ meson and proton) and c and d are the reaction products which could be two resonances. A specific example discussed in Chapter 4 is

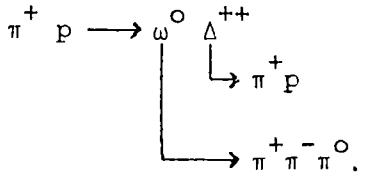

The ω^o and Δ^{++} have such short lifetimes that it is only their decay products that can ever be observed, and such a reaction channel will appear (along with other reactions leading to similar final states) as a final state $p\pi^+\pi^+\pi^-\pi^o$.

A strong motivation for the study of such quasi-two-body processes is their inherent simplicity. Experimentally, it is possible to recognise them reasonably easily and theoretically one can hope to describe them in a simpler manner than could be possible for a many particle final state. The experimental measurements yield the total channel cross-section, the differential cross-section (as a function of angle or four-momentum transfer) and information about the spin states of the particles produced. In later Sections of this Chapter a general discussion of the extraction of these quantities from the data will be given. In the last Section is given a qualitative description of the kind of theoretical treatments that are currently used to discuss channels of this type.

2.2 The Total Cross Section

It is possible to determine an absolute total cross-section with a bubble chamber experiment if a careful account is kept of the incident particle intensity throughout the scanned film and corrections are made for unwanted particle contamination in the beam and the density of the liquid hydrogen is precisely known. However, scanning speeds are reduced by the requirement of sample counting of incident beam tracks, and there are practical difficulties in keeping the same criteria for such measurements in different laboratories spread over Europe. It is much easier to be sure that the interactions are correctly recorded, and it was decided that the present experiment would not be used to determine an absolute cross-section, but that published counter measurements would be used to determine the cross-section equivalent of the scanned events.†

Table (2.1) lists the number of events found per laboratory as a function of prong number (normally called a topology classification).

Table (2.1)

Topology classification

Laboratory	Corrected 2-Prong	Corrected 4-Prong	Corrected 6-Prong	Corrected 8-Prong	Corrected ≥10-Prong	Corrected Total
Durham	12,068	9,478	3,966	705	64	26,281
Genova	13,321	13,462	6,170	1,178		34,131
Hamburg	5,363	5,475	2,458	458	33	13,787
Milano	9,313	9,121	3,745	672	48	22,899
Saclay	25,436	26,214	9,862	182	18	61,712
Total	65,501	63,750	26,201	3,358		158,810

† For a partial Durham sample in which track counting was done a reasonable agreement with the counter results was found [10].

Corrections were applied to all the events for scanning efficiency. In addition, there is a loss of two prong events when proton momenta are low and therefore such events may appear merely as scatters. This is important at high energies for elastic scatters which are dominated by small momentum transfers. The loss of events was most pronounced for $|t| \leq 0.02$ $(GeV/c)^2$ and $\phi = 90^o$ (i.e., parallel to the optic axes of the cameras). This visibility correction amounted to 37% on 2-prong elastic events [10].

Hence equating the total corrected number of events to the counter cross-section at this energy [11] one gets:

$$158{,}810 \text{ events} = 24.5 \pm 0.08 \text{ mb},$$

$$\mu b/\text{event} = 0.1543.$$

Since 90% of the scanned 4-prong events could be measured well enough to appear on the DST, assuming a random loss, equally over all channels, one arrives at the normalisation:

$$\mu b/\text{event for 4-prong DST} = 0.17.$$

2.3 The Breit Wigner Function

The effective mass distribution of the particles the resonance decays into has a Breit-Wigner shape. In order to estimate the channel cross-section a Breit Wigner function superimposed on a smoothly varying background is fitted to such a mass distribution. The fitting thus not only estimates the cross-section but also determines mass and width at half height of the resonance.

The effect of background is one of the major problems in an analysis of a resonance channel. This is caused by random association from all those final states not containing the resonance. In most of the cases the details of all such states are not known,

therefore a guess has to be made regarding the shape of the background, e.g., linear or quadratic depending on the shape of the distribution on either side of the resonance. The better the guess regarding the background, the better would be the level of confidence for the fit.

A simple Breit-Wigner function has the form:

$$BW = \frac{(\Gamma/2)^2}{(m-m_o)^2 + (\Gamma/2)^2}, \qquad (2.1)$$

where m, m_o and Γ respectively are the effective mass of the combination of particles, the central mass and full width at half height. This is obviously a symmetric function.

Experimentally, it is observed that some resonances are asymmetric. Such an asymmetric mass-dependent Breit Wigner function has the form [12]:

$$BW(m) = \frac{c\Gamma(m)}{(m^2-m_o^2)^2 + (m_o\Gamma(m))^2} \frac{m}{q}, \qquad (2.2)$$

where c is the normalisation constant, m is the effective mass of the particle combination under consideration, m_o the central mass and Γ the width of the resonance. For a two particle decay the width can be expressed as a function of the effective mass of the particle combination which takes into account the centrifugal barrier affecting the decay of the resonance.

$$\Gamma(m) \approx \Gamma_o (q/q_o)^{2\ell+1}, \qquad (2.3)$$

where q is the three-momentum of either decay particle in the rest frame of the resonance, q_o is the central value of q (i.e., for $m = m_o$) and ℓ is the orbital angular momentum. For $\ell = 0$, 1 and 2, the relevant Breit-Wigner function is respectively called s-wave, p-wave and d-wave Breit-Wigner function. The q can be

written as:

$$q^2 = \frac{[m^2 - (m_1+m_2)^2]\ [m^2 - (m_1-m_2)^2]}{4\ m^2}\ , \qquad (2.4)$$

where m is the effective mass of the particle combination under consideration and m_1 and m_2 are the rest masses of the decay products.

The ω^o-decay into three-pion obviously is not the same condition as a two particle decay but since the ω^o natural width $\Gamma_o \simeq 10\ MeV/c^2$ and hence the variation of q/q_o is small. The form of the Breit Wigner function given in equation (2.2) has been used for the symmetric situation where the three pions have the same energy in the rest system of the ω^o-decay. In this case the final state is considered as consisting of two particles, a pion and a dipion system where the mass, $m_{2\pi}$ of the latter is:

$$m_{2\pi}^2 = \frac{m^2 + 3m_\pi^2}{3}\ . \qquad (2.5)$$

The value of q for an ω -mass, m, is then given by:

$$q^2 = \frac{[m^2 - (m_\pi + m_{2\pi})^2]\ [m^2 - (m_\pi - m_{2\pi})^2]}{4m^2}\ , \qquad (2.6)$$

where q_o corresponds to the value m_o.

The minimum errors on the mass and width are worked out in later chapters using the following formula given by Davis et al. [13,14].

$$\left.\begin{aligned} \delta_{min}\ (m) &= \Gamma/\sqrt{N}\ , \\ \delta_{min}\ (\Gamma) &= 4\Gamma/\sqrt{N}\ , \end{aligned}\right\} \qquad (2.7)$$

where N is the number of events in the resonance.

2.4 The Important Parameters of the Quasi-two-body Reactions

The following three quantities are of special interest in the study of the quasi-two-body reactions.

(i) The total channel cross-section (σ) of the reaction and its dependence on the beam momentum in the laboratory.

(ii) The differential cross-section of the reaction $(d\sigma/d|t|)$ or $(d\sigma/d|t'|)$. The four-momentum transfer (see equation (2.36)) from the incident meson (baryon) to the meson (baryon) resonance is denoted by $|t|$ and $|t'| = |t-t_{min}|$, where t_{min} is the minimum value of the $|t|$. Because of the width of a resonance, t_{min} varies from event to event, therefore it is preferable to use $|t'|$, rather than $|t|$ for the study of the differential cross-section in the forward direction (small $|t|$ or $|t'|$). However, dips and other structure, if any, in the distribution of $d\sigma/d|t'|$ other than those at $|t'| = 0$, are not greatly affected by the choice of $|t'|$ or $|t|$. Visibility problems may arise at low $|t|$, because there may be loss of events where laboratory momentum of proton is very low.

(iii) The resonance decay angular distribution. If the spin of the resonance is known, the decay angular distribution gives the information regarding the spin density matrix elements (i.e., the relative probabilities of the different magnetic substates on the axis of quantization). The relative population for the different spin projections are related to the dynamics of the reaction. The average value of the spin density matrix elements and their dependence on the variable $|t|$, will be studied in the present work wherever the statistics permit.

2.4.1 The density matrix

Consider a quantum mechanical system of spin j. As a general case this pure state consists of a linear superposition of basis vectors belonging to the same j.

$$\left.\begin{aligned} \psi_j = |j\rangle &= \sum_{m=-j}^{m=j} a_m |j,m\rangle \\ \text{its conjugate state is} \\ \psi_j^* = \langle j| &= \sum_{m=-j}^{m=j} a_m^* \langle j,m| \,. \end{aligned}\right\} \qquad (2.8)$$

The normalised state is

$$\sum_{m=-j}^{m=j} a_m^* a_m = \sum_{m=-j}^{m=j} |a_m|^2 = 1 . \qquad (2.9)$$

The expectation value of an operator Q is given by:

$$\left.\begin{aligned} \langle Q\rangle &= \sum_{m,m'} a_m^* a_{m'} \langle j,m|Q|j,m'\rangle \\ &= \sum_{m,m'} a_m^* a_{m'} Q_{m,m'} , \end{aligned}\right\} \qquad (2.10)$$

where $\langle j,m|Q|j,m'\rangle$ is the matrix element $Q_{m,m'}$ of the operator Q. The density matrix ρ for this pure state is defined by:

$$\rho_{m'm} = a_{m'} a_m^* \,; \quad \mathrm{Tr}\ \rho = 1 \,, \qquad (2.11)$$

where Tr denotes the trace of the matrix.

In general one has to deal with "mixed states" which are a statistical mixture of the pure states and can be described by the incoherent sum of the pure states.

For a statistical mixture of state $\psi^{(i)}$ with probabilities $w^{(i)}$, the average value of a physical quantity Q will be:

$$\langle Q\rangle = \sum_i w^{(i)} \langle Q^{(i)}\rangle \qquad (2.12)$$

with

$$\langle Q^{(i)} \rangle = \langle \psi^{(i)} | Q | \psi^{(i)} \rangle \quad . \tag{2.13}$$

The pure states $|\psi^{(i)}\rangle$ can be defined in terms of the angular momentum: for a given angular momentum j there are (2j+1) eigen-functions corresponding to the different values of the magnetic quantum number m:

$$|\psi^{(i)}\rangle = \sum_m a_m^{(i)} \; |\psi_m\rangle \quad . \tag{2.14}$$

Substituting in equation (2.13), one gets

$$\langle Q^{(i)} \rangle = \sum_{m,m'} a_m^{(i)*} \; a_{m'}^{(i)} \; Q_{m,m'} \tag{2.15}$$

$$\langle Q \rangle = \sum_i w^{(i)} \left\{ \sum_{m,m'} a_m^{(i)*} \; a_{m'}^{(i)} \; Q_{m,m'} \right\} \tag{2.16}$$

$$\left. \begin{aligned} &= \sum_{m,m'} Q_{mm'} \; \rho_{m'm} = \sum_m (Q\rho)_{mm} \\ &= \mathrm{Tr}\,(Q\rho) \qquad = \mathrm{Tr}\,(\rho Q) \end{aligned} \right\} \tag{2.17}$$

where

$$\rho_{m'm} = \sum_i w^{(i)} \; a_m^{(i)*} \; a_{m'}^{(i)} \quad . \tag{2.18}$$

$\rho_{m'm}$ are termed as the density matrix elements.

Some of the important properties of the density matrix are given below:

(i) It is hermitian

$$\rho_{mm'} = \rho^*_{m'm}$$

(ii) The sum of the diagonal elements is 1.

$$\sum_m \rho_{mm} = \mathrm{Tr}\,(\rho) = 1$$

(iii) The diagonal elements are positive

$$\rho_{mm} \geq 0$$

(iv) From parity conservation in the production process with unpolarised incident particles, it follows:

(a) $\rho_{mm'} = (-1)^{m-m'} \rho_{-m,-m'}$ (z-axis in production plane)

(b) $\rho_{mm'} = 0$ for $(m-m')$ odd (z-axis normal to production plane).

The detailed discussion of the density matrix is available in the literature [15].

2.5 Frames of Reference

Consider a quasi-two-body reaction of the type

$$a + b \longrightarrow c + d,$$

where a and b respectively are the incident particle and the target proton and c or/and d are resonances. Let c and d be meson and baryon respectively, where d is the resonance under consideration which decays into α and β.

The choice of a frame of reference, in principle, is arbitrary. But different frames emphasise different characteristics [16]. For the helicity-type axes the z-axis is defined by the direction of either b (the t-channel helicity or Gottfried - Jackson frame) in the rest system of d or c (the s-channel helicity or helicity frame) in the C.M. system. The y-axis is taken in the direction of the normal to the reaction plane and the x-axis is chosen to define a right-handed coordinate system.

Figures (2.1 a-c) show the decay of the d (in its rest frame) with respect to the above production plane. The momenta of a, c and b lie in the production plane (plane of paper). The momenta of α and β are equal in magnitude and opposite and are denoted by the dotted lines. They usually do not lie in the production plane. The right-handed coordinate systems xyz in the two categories of helicity-type axes are:

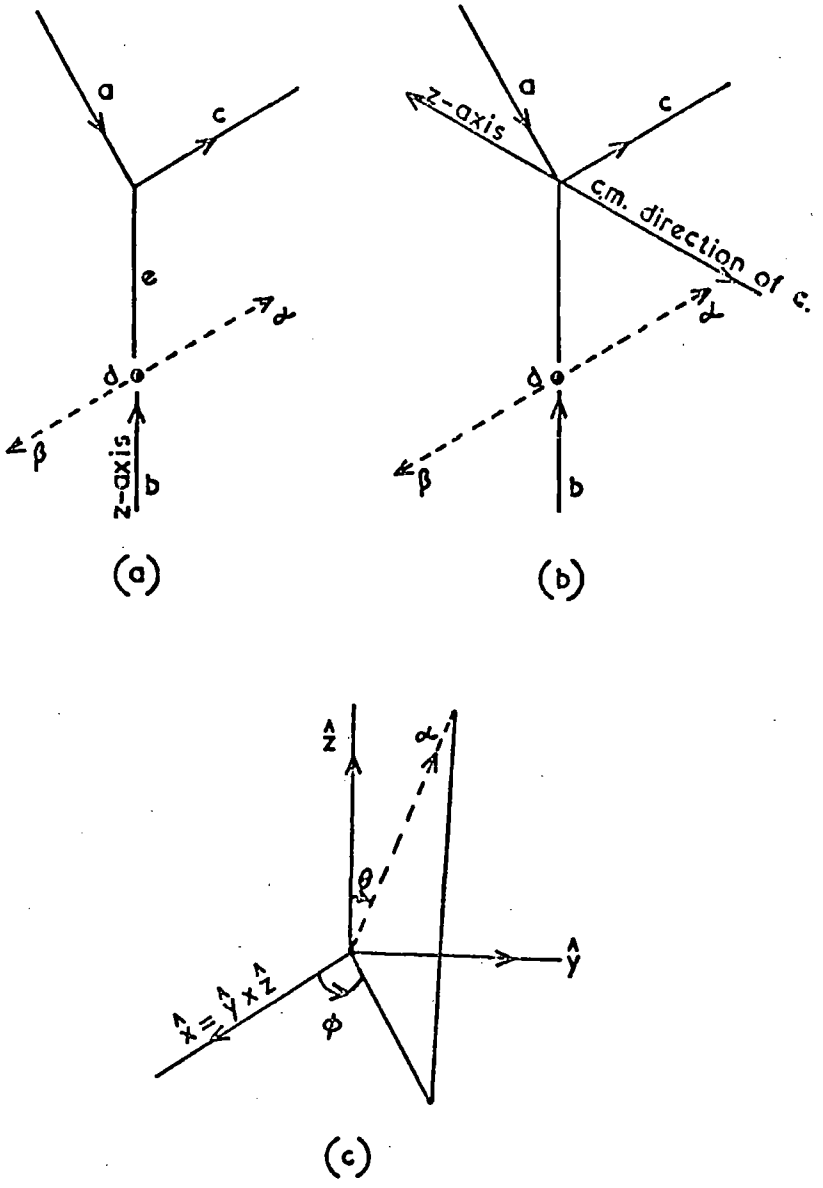

FIG. 2.1 a) THE t-CHANNEL HELICITY FRAME.

b) THE s-CHANNEL HELICITY FRAME.

c) THE POLAR AND THE AZIMUTHAL ANGLES OF THE DECAY PARTICLE α IN THE t- AND s-CHANNEL HELICITY FRAMES.

The t-channel helicity (Gottfried-Jackson) frame

$$\left.\begin{aligned} \hat{y} &= \frac{\vec{a} \times \vec{c}}{|\vec{a} \times \vec{c}|}^{\dagger} && \text{(a)} \\ \hat{z} &= \frac{\vec{b}}{|\vec{b}|}^{\dagger} && \text{(b)} \\ \hat{x} &= \hat{y} \times \hat{z} && \text{(c)} \end{aligned}\right\} \qquad (2.19)$$

The s-channel helicity (helicity frame)

$$\left.\begin{aligned} \hat{y} &= \frac{\vec{a} \times \vec{c}}{|\vec{a} \times \vec{c}|}^{\dagger} && \text{(a)} \\ \hat{z} &= -\frac{\vec{c}}{|\vec{c}|}^{\dagger} && \text{(b)} \\ \hat{x} &= \hat{y} \times \hat{z} && \text{(c)} \end{aligned}\right\} \qquad (2.20)$$

The decay angles θ and ϕ (see Figure 2.1c), being the polar angle and azimuthal angle (also called Trieman-Yang angle [12,19]), respectively, of the decay particle α (or β)†† are given by the following formulas:

$$\left.\begin{aligned} \cos\theta &= \hat{z} \cdot \frac{\vec{\alpha}}{|\vec{\alpha}|} && \text{(a)} \\ \cos\phi &= \hat{y} \cdot \frac{\vec{z} \times \vec{\alpha}}{|\vec{z} \times \vec{\alpha}|} && \text{(b)} \end{aligned}\right\} \qquad (2.21)$$

---

† For the meson resonance: $\hat{y} = \frac{\vec{b} \times \vec{d}}{|\vec{b} \times \vec{d}|}$ in equations (2.19a) and (2.20a) and $\hat{z} = \frac{\vec{a}}{|\vec{a}|}$ in equation (2.19b) and $\hat{z} = -\frac{\vec{d}}{|\vec{d}|}$ in equation (2.20b). The advantage of this choice is given for the discussion of the peripheral model as explained in references [17,18].

†† For the ω^{o} decays into three pions, the normal to the ω^{o} decay plane in the ω rest system is given by $\hat{n} = \frac{\vec{\pi^-} \times \vec{\pi^o}}{|\vec{\pi^-} \times \vec{\pi^o}|}$ and θ and ϕ are thus given by formulas (2.21), if one replaces $\hat{\alpha}$ by $\hat{n}$.

Here ϕ varies between 0^{o} and 360^{o} but its value is zero or 180^{o} in the production plane. The symbols in these formulas mean the momenta of the particles in the rest frame of the d except in equation (2.20b), where c denotes the momentum of the particle c in the C.M.S.

The transversity-type axes, where the z-axis is taken along the normal to the reaction plane, are obtained by relabelling the respective helicity type-axis in the following way:

$$\left.\begin{aligned} z_T &= y_H && \text{(a)} \\ y_T &= -z_H && \text{(b)} \\ x_T &= x_H && \text{(c)} \end{aligned}\right\} \qquad (2.22)$$

Here the minus sign in equation (2.22b) is required to define a right-handed coordinate system as given in references [20,21].

The transformation of angles from the helicity-type axes to the transversity-type axes can be done in the following way as given in reference [22].

$$\left.\begin{aligned} \cos\theta_T &= \sin\theta_H \sin\phi_H \\ \sin\theta_T \cos\phi_T &= \sin\theta_H \sin\phi_H \\ \sin\theta_T \sin\phi_T &= -\cos\theta_H \end{aligned}\right\} \qquad (2.23)$$

Figure (2.1d) shows the possible orientation of the axes giving the decay of the d (in its rest frame) with reference to the production process a+b $\longrightarrow$ c+d. For the t-channel helicity frame

$$(x_H, y_H, z_H) = (1^t, 2, 3^t)$$

and for the s-channel helicity frame

$$(x_H, y_H, z_H) = (1^s, 2, 3^s).$$

Similarly for the t-channel transversity frame

$$(x_T, y_T, z_T) = (1^t, -3^t, 2)$$

and for the s-channel transversity frame

$$(x_T, y_T, z_T) = (1^s, -3^s, 2).$$

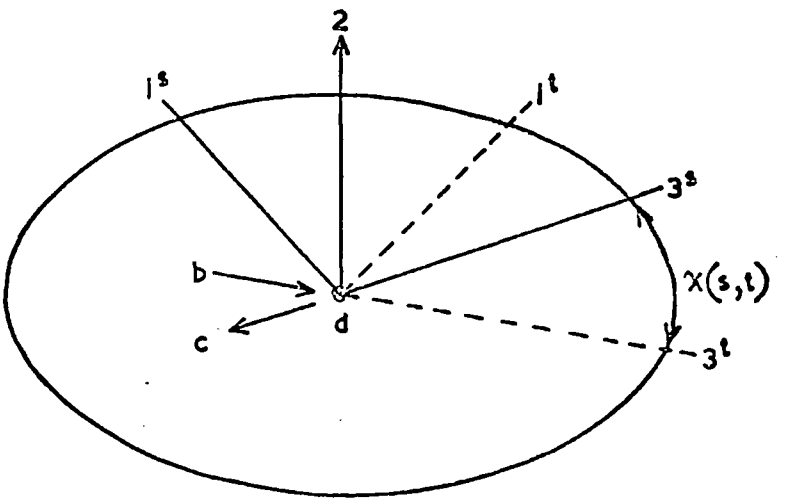

FIG. 2.1 d. THE POSSIBLE ORIENTATION OF THE AXES FOR THE DECAY OF PARTICLE d (IN ITS REST FRAME) WITH REFERENCE TO THE PRODUCTION PROCESS $a+b \longrightarrow c+d$.

The s-channel and the t-channel axes are related by a rotation χ about the normal (i.e., axis 2) to the a + b $\longrightarrow$ c+d production plane. The angle χ is called the s-t crossing angle. It can be shown that the polar angles (θ) of the decay particle in the transversity frames are unchanged by rotations and are thus frame invariant.

2.6 Decay Angular Distributions

For a resonance with $J^P = 1^-$ decaying into three pseudoscalar mesons (e.g., $\omega^o \longrightarrow \pi^+\pi^-\pi^o$), the density matrix in the t- and s-channel helicity frames may be written as:

$$\rho = \begin{pmatrix} \rho_{11} & \rho_{10} & \rho_{1,-1} \\ \rho^*_{10} & \rho_{00} & -\rho^*_{10} \\ \rho_{1-1} & -\rho_{10} & \rho_{11} \end{pmatrix} . \qquad (2.24)$$

Parity conservation restricts the density matrix elements:

$$\rho_{m,m'} = (-1)^{m-m'} \rho_{-m,-m'}$$

and there are three real elements (ρ_{11}, ρ_{00} and $\rho_{1,-1}$) and one complex element ρ_{10}.

The normalised† decay angular distribution is given by [17,18]:

$$W(\cos\chi,\psi) = \frac{3}{4\pi}\left\{ \frac{1-\rho_{00}}{2} + \frac{3\rho_{00}-1}{2}\cos^2\chi - \rho_{1-1}\sin^2\chi\cos 2\psi - \sqrt{2}\,\mathrm{Re}\,\rho_{10}\sin 2\chi\cos\psi \right\} \qquad (2.25)$$

Integrating equation (2.25) first over ψ and then over $\cos\chi$ gives:

---

† The normalization is such that

$$\int_0^{2\pi} d\psi \int_{-1}^{+1} d\cos\chi \;.\; W(\cos\chi,\psi) = 1 .$$

$$\left.\begin{aligned} W(\cos\chi) &= \frac{3}{4}\left\{(1-\rho_{00}) + (3\rho_{00}-1)\cos^2\chi\right\} \qquad \text{(a)} \\ W(\psi) &= \frac{1}{2\pi}\left\{(1+2\rho_{1,-1}) - 4\rho_{1-1}\cos^2\psi\right\} \qquad \text{(b)} \end{aligned}\right\} \tag{2.26}$$

In the t- and the s-channel transversity frames, the reflection invariance gives:

$$\rho_{mm'} = 0 \text{ for } (m-m') \text{ odd.}$$

The density matrix can be written as:

$$\rho = \begin{pmatrix} \rho_{11} & 0 & \rho_{1-1} \\ 0 & \rho_{00} & 0 \\ \rho^{*}_{1,-1} & 0 & \rho_{-1,-1} \end{pmatrix} . \tag{2.27}$$

The normalised decay angular distribution then becomes [23]:

$$W(\cos\chi, \psi) = \frac{3}{4\pi}\left\{\frac{1-\rho_{00}}{2} + \frac{3\rho_{00}-1}{2}\cos^2\chi - \text{Re}\,\rho_{1-1}\sin^2\chi\cos 2\psi + \text{Im}\,\rho_{1-1}\sin^2\chi\sin 2\psi\right\} \tag{2.28}$$

Integrating equation (2.28) first over ψ and then over $\cos\chi$ gives:

$$\left.\begin{aligned} W(\cos\chi) &= \frac{3}{4}\left\{(1-\rho_{00}) + (3\rho_{00}-1)\cos^2\chi\right\} \qquad \text{(a)} \\ W(\psi) &= \frac{1}{2\pi}\left\{1 + 2\text{Re}\,\rho_{1-1} - 4\,\text{Re}\,\rho_{1-1}\cos^2\psi + 4\,\text{Im}\,\rho_{1-1}\sin\psi\cos\psi\right\} \qquad \text{(b)} \end{aligned}\right\} \tag{2.29}$$

For a baryonic resonance with $J^P = 3/2^+$ decaying into a spinless pion and a spin 1/2 baryon, the density matrix in the t- and the s-channel helicity frames has the form:†

---

† The subscripts on the density matrix elements are 2 m and 2m'.

$$\rho = \begin{pmatrix} \rho_{33} & \rho_{31} & \rho_{3-1} & \rho_{3-3} \\ \rho^*_{31} & \rho_{11} & \rho_{1-1} & \rho^*_{3-1} \\ \rho^*_{3-1} & -\rho_{1-1} & \rho_{11} & -\rho^*_{31} \\ -\rho_{3-3} & \rho_{3-1} & -\rho_{31} & \rho_{33} \end{pmatrix} . \qquad (2.30)$$

Parity conservation restricts the density matrix elements:

$$\rho_{mm'} = (-1)^{m-m'} \rho_{-m,-m'}$$

and hermiticity requires that all the diagonal elements are real and that ρ_{3-3} and ρ_{1-1} are purely imaginary.

The normalised decay angular distribution is given by [17]:

$$W(\cos\theta, \phi) = \frac{3}{4\pi} \left\{ \frac{1 + 4\rho_{33}}{6} + \frac{1}{2}(1 - 4\rho_{33})\cos^2\theta - \frac{2}{\sqrt{3}} \mathrm{Re}\,\rho_{3-1} \sin^2\theta \cos 2\phi - \frac{2}{\sqrt{3}} \mathrm{Re}\,\rho_{31} \sin 2\theta \cos\phi \right\} \qquad (2.31)$$

Integrating equation (2.31) first over ϕ and then over $\cos\theta$ gives:

$$\left.\begin{aligned} W(\cos\theta) &= \frac{1}{4}\left\{(1+4\rho_{33}) + (3-12\rho_{33})\cos^2\theta\right\} \quad \text{(a)} \\ W(\phi) &= \frac{1}{2\pi}\left\{(1+\frac{4\sqrt{3}}{3}\mathrm{Re}\,\rho_{3-1}) - \frac{8\sqrt{3}}{3}\mathrm{Re}\,\rho_{3-1}\cos^2\phi\right\} \quad \text{(b)} \end{aligned}\right\} \qquad (2.32)$$

In the t- and the s-channel transversity frames, the reflection invariance gives:

$$\rho_{mm'} = 0 \quad \text{for } (m-m') \text{ odd}.$$

The density matrix can be written as:

$$\rho = \begin{pmatrix} \rho_{33} & 0 & \rho_{3-1} & 0 \\ 0 & \rho_{11} & 0 & \rho^{*}_{3-1} \\ \rho^{*}_{3-1} & 0 & \rho_{-1-1} & 0 \\ 0 & \rho_{3-1} & 0 & \rho_{-3-3} \end{pmatrix} . \qquad (2.33)$$

The noramlised decay angular distribution then becomes [24]:

$$W(\cos\theta, \phi) = \frac{3}{4\pi}\left[\frac{1+2(\rho_{33}+\rho_{-3-3})}{6} + \frac{1}{2}\left\{1 - 2(\rho_{33}+\rho_{-3-3})\right\}\cos^2\theta - \frac{1}{\sqrt{3}}\,\mathrm{Re}\,(\rho_{3-1}+\rho_{-31})\sin^2\theta\cos 2\phi + \frac{1}{\sqrt{3}}\,\mathrm{Im}\,(\rho_{3-1}-\rho_{-31})\sin^2\theta\sin 2\phi \right] \qquad (2.34)$$

Integrating equation (2.34), first over ϕ and then over $\cos\theta$ gives:

$$\left.\begin{aligned} W(\cos\theta) &= \frac{1}{4}\left[1+2(\rho_{33}+\rho_{-3-3})+3\left\{1-2(\rho_{33}+\rho_{-3-3})\right\}\cos^2\theta\right] \quad (a) \\ W(\phi) &= \frac{1}{2\pi}\left[1+\frac{2\,\mathrm{Re}\,(\rho_{3-1}+\rho_{-31})}{\sqrt{3}} - \frac{4\,\mathrm{Re}\,(\rho_{3-1}+\rho_{-31})}{\sqrt{3}}\cos^2\phi + \frac{4\,\mathrm{Im}\,(\rho_{3-1}-\rho_{-31})}{\sqrt{3}}\sin\phi\cos\phi\right] \quad (b) \end{aligned}\right\} (2.35)$$

2.7 Qualitative Discussion of Current Theoretical Models

The basic starting point of theoretical models for a quasi-two-body channel:

$$a + b \longrightarrow c + d$$

is the peripheral one particle exchange model normally represented by a Feynman diagram of the type shown in Figure (2.2). The process

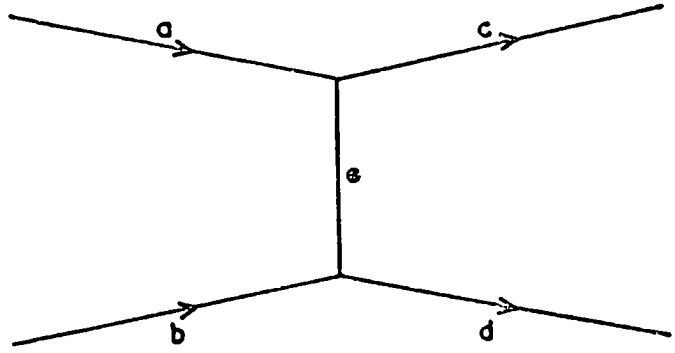

FIG. 2.2 FEYNMAN DIAGRAM FOR A TWO-BODY REACTION WITH PARTICLE EXCHANGE e.

is thought of as being mediated by a virtual exchange particle e, the cross-section depending on the two couplings of e at the two vertices and a propagator term. The kinematic variables normally employed are s, t (and u for backward production in the centre of mass, a process which will not be considered in the present work). These variables are called the Mandelstam variables [25,26] and are defined as:

$$\left.\begin{aligned} s &= (q_a + q_b)^2 = (q_c + q_d)^2 = (\text{total c.m. energy})^2, \\ t &= (q_a - q_c)^2 = (q_b - q_d)^2 = (\text{4-momentum transfer from a to c or from b to d})^2, \\ u &= (q_a - q_d)^2 = (q_b - q_c)^2 = (\text{crossed 4-momentum transfer from a to d or from b to c})^2, \end{aligned}\right\} \quad (2.36)$$

where q_i is 4-momentum transfer of particle i = $(E_i, \vec{p_i})$

These variables are related by

$$s + t + u = m_a^2 + m_b^2 + m_c^2 + m_d^2 = \sum_{i=a}^{d} m_i^2, \quad (2.37)$$

where m_i is mass of particle i.

In the present experiment s is fixed by the incident beam momentum, having a value of 22.5 $(\text{GeV})^2$. This is of course the square of the total c.m. energy E which has the value 4.74 GeV. The only kinematic variable that remains at fixed s is the four-momentum transfer, t, which in the type of production channels under discussion, always has a negative value. Kinematically, t is the square of what would normally be considered the mass of a particle, in this case the exchange particle e. Clearly, whatever the nature of the real particle corresponding to e, in the Feynman diagram of Figure (2.2), it is off the mass shell. However, it is an observed general property of quasi-two-body production that the values of t tend to be close to zero, and hence particularly when

e is considered to be a pion, the exchanged particle is not far off the mass shell.

Starting with the simplest version of a one particle exchange model, a short qualitative resume of different theoretical models, that are currently important for quasi-two-body processes will now be given.†

2.7.1 The one particle exchange (OPE) model

The fact that the interactions take place at low value of $|t|$ suggests that reactions occur by exchange of a particle. Such a particle e is shown in Figure (2.2). From Feynman rules the transition matrix element for the Figure (2.2) has the following form:

$$T(s,t) = V_{aec}\left[\frac{1}{m_e^2 - t}\right] V_{bed} \quad , \tag{2.38}$$

where $1/(m_e^2-t)$ is the propagator of the exchange particle and V_{aec} and V_{bed} are the vertex functions dependent on coupling constants. At the non-physical point $t = m_e^2$ there is a pole and the vertex functions are equal to the matrix elements for the following peripheral processes:

$$\left.\begin{aligned} a + e &\longrightarrow c \, , \\ b + e &\longrightarrow d \, . \end{aligned}\right\} \tag{2.39}$$

This model predicts large cross sections at small values of $|t|$ particularly for small m_e. Therefore, reactions taking place by one pion exchange are expected to be peripheral. The one pion exchange model was first suggested by Goebel [28] and later by Chew and Low [29].

---

† A survey of the current models for high energy processes is given by Jackson [27].

The quantum numbers of the exchanged particle as shown in Figure (2.2) are limited by conservation laws — e.g., baryon number, charge, G-parity, strangeness and isospin conservation — at each vertex.

The attraction of this simple model is that the t dependence of the cross-section is dominated by the propagator term which decreases as $|t|$ increases but tends to increase the cross-section at low values of $|t|$, i.e., close to the pole, just as the experimental data qualitatively indicate. The small value of $|t|$ corresponds to small c.m. scattering angle which is favoured by the propagator. However, as will be seen later, the detailed shape of the experimentally observed t distribution is not reproduced by this simple model and therefore attempts have been made to modify the model in a consistent way.

For the two-body channels discussed in this thesis the restrictions on e are obtained below:

(a) For the reaction $\pi^+ p \longrightarrow \omega^o \Delta^{++}$, the possible candidates for exchange are ρ and B. These two exchanged particles give certain predictions on the density matrix elements which are discussed below.

(i) The ω production via ρ exchange (natural parity)

If the ρ-meson is exchanged, the process occurring at the meson vertex of Figure (2.3a) when seen in the rest frame of the ω looks like Figure (2.3b). Here the exchange particle belongs to the natural parity series (1^-, 2^+, ...).

From angular momentum conservation: $L = J_e - 1, J_e, J_e + 1$. So vectors of $\vec{L}$ can be composed with J_e to give spin 1 of the c meson (the ω^o in this case). The z-component of L, $L_z = 0$,

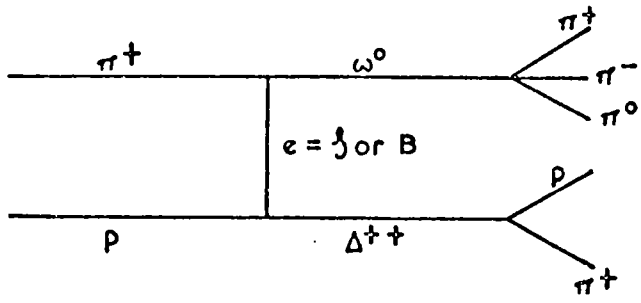

(a)

(b)

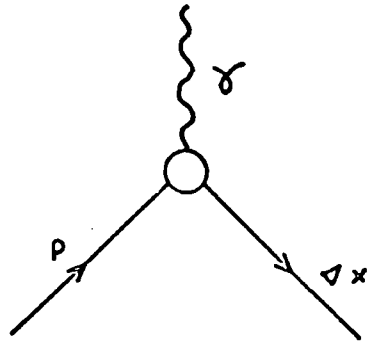

(c)

FIG. 2.3

a) DIAGRAM FOR THE REACTION $\pi^+ p \longrightarrow \omega^0 \Delta^{++}$ WITH ℓ OR B EXCHANGE.

b) SKETCH FOR THE PROCESS $\pi^+ e \longrightarrow \omega$ AT THE VERTEX a e c IN REST FRAME OF c.

c) DIAGRAM FOR THE PHOTOPRODUCTION OF $\gamma p \rightarrow \Delta^+$.

where z is the axis of quantization which is direction of incident π^+.

From parity conservation:

$$P_a\,(-1)^{J_e}\,(-1)^{L} = P_c = (-1)\,.$$

Hence $L + J_e$ is even. Also $L = J_e$. Conservation of z-component of angular momentum requires $J_{ez} = m = 0, \pm 1$. Thus there are only two spin states $|J_e, \pm 1\rangle$ which can be coupled with the orbital angular momentum state $|L = J_e, 0\rangle$ to give the states of $c = |J_c = 1, m = \pm 1\rangle$. On the other hand the two states $|J_e, 0\rangle$ and $|L = J_e, 0\rangle$ cannot be composed to give $|J_c = 1, m = 0\rangle$.

In the expansion of $|L = J_e, 0\rangle\,|J_e, 0\rangle$ into eigenstates $|J, 0\rangle$ of the total angular momentum only terms with even J survive and $\langle L = J_e, J_e; 0,0 \,|\, J_c = 1, m = 0\rangle$ vanishes for odd $L + J_e + J_c$. Thus it follows that $|m = 0\rangle$ vanishes and $|m = \pm 1\rangle$ survives. Hence

$$\rho_{0m} = \rho_{m0} = 0\,, \text{ i.e., } \rho_{00} = 0 \text{ and } \rho_{11} = 1/2\,.$$

Jackson et al.[30,31] further conclude that if only natural parity exchange occurs then $\rho_{1-1} = \rho_{11}$ as $s \longrightarrow \infty$.

The decay angular distributions (2.25) and (2.26) become:

$$W(\cos\chi,\psi) = \frac{3}{4\pi}\,(1/2 - \rho_{1-1}\cos 2\psi)\,\sin^2\chi \qquad (2.40)$$

$$\left.\begin{aligned} W(\cos\chi) &= 3/4\,\sin^2\chi \qquad (a)\\ W(\psi) &= \frac{1}{2\pi}\left[(1 + 2\rho_{1-1}) - 4\rho_{1-1}\cos^2\psi\right] \qquad (b)\end{aligned}\right\} \qquad (2.41)$$

(ii) The ω production via B exchange (unnatural parity).

If the B-meson is exchanged then the process in Figure (2.3b) belongs to the unnatural parity series $(1^+, 2^-, \ldots\ldots)$

From Angular momentum conservation:

$$L = J_e + 1,\ J_e,\ J_e - 1.$$

From parity conservation:

$$P_a\,(-1)^{J_e+1}\,(-1)^{L} = P_c.$$

Hence $L + J_e$ is odd or $L = J_e \pm 1$.

In this case all the three spin states $m = 0, \pm 1$ are permissible. Hence in general all the matrix elements ρ_{00}, ρ_{1-1}, ρ_{10} are non-zero. The matrix element ρ_{10} is non-zero for exchange of a particle with unnatural parity and $J_e \geq 1$ in the t-channel helicity frame [17].

(iii) The Δ production via ρ exchange.

Assuming the exchange of ρ-meson at the baryon vertex of Figure (2.3.a), Stodolsky and Sakurai [32,33] treated the vertex $p\rho\Delta^{++}$ similar to the photo-production vertex in Figure (2.3c) because the ρ-meson has the same quantum numbers as the γ. The latter reaction is $\gamma p \longrightarrow \Delta^{+} \longrightarrow p\pi^{o}$. They found that the Δ^{+} has only the spin orientations $m = \pm 1$ normal to the production plane. The decay distribution in the transversity frame has the form:

$$W(\cos\theta_T, \phi_T) = \frac{1}{8\pi}\,(1 + 3\cos^2\theta_T)\,. \qquad (2.42)$$

Using equation (2.23), the transformed distribution (2.42) in the helicity frame becomes:

$$W(\cos\theta_H, \phi_H) = \frac{1}{8\pi}\,(1 + 3\sin^2\theta_H \sin^2\phi_H)\,. \qquad (2.43)$$

From the above equation Stodolsky and Sakurai predicted the following values of the density matrices for the Δ^{++} for a ρ exchange:

$$\rho_{33} = 3/8, \quad \text{Re}\,\rho_{3-1} = \sqrt{3}/8, \quad \text{Re}\,\rho_{31} = 0. \qquad (2.44)$$

Hence all other decay parameters, including the joint decay distributions should vanish, if the OPE model holds for the reaction $\pi^{+}p \longrightarrow \omega\Delta^{++}$ which provides a severe test of this simple model [34].

(b) For the reaction $\pi^+ p \longrightarrow pB^+$, the possible lowest mass exchange particle is the ω-meson. The slope of the differential cross-section supports such an exchange.

This model does not show a rapid enough fall off of the differential cross-section with t and predictions on the density matrix elements are not satisfied in a number of reactions, hence attempts have been made to modify it by introducing form factors in the vertex functions and the absorptive effects in the collisions of two particles at higher energies where many inelastic channels compete with one another.

The peripheral models ran into difficulty when the exchanged particle had spin more than zero. Various calculations have been made by several workers on different reactions using the Regge pole model [35,36] with or without absorption. According to this model, particles and resonances can be grouped into families, each family being associated with a given Regge trajectory.

Gell-Mann [37] proposed that the hadrons were built up of more fundamental particles — called quarks. From the assignment of different quantum numbers to the quarks and the application of the conservation laws, calculations have been made by different workers to explain several high energy reactions on the basis of the quark model.

The detailed theoretical calculations of above models is beyond the scope of this thesis. However, predictions made on the values of differential cross-section and the spin density matrix elements on the basis of different models relevant to the reactions: $\pi^+ p \longrightarrow \omega\Delta^{++}$ and $\pi^+ p \longrightarrow pB^+$ will be discussed in Chapters 4 and 5.

CHAPTER 3

SELECTION OF EVENTS AND THE INITIAL RESULTS

3.1 Introduction

In this Chapter, the production of the ω^o from the reaction

$$\pi^+ p \longrightarrow p\pi^+\pi^+\pi^-\pi^o, \qquad (3.1)$$

at incident momentum of 11.7 GeV/c will be discussed. The strong production of the ω^o resonance is prominent in this reaction. A rough outline of the Chapter is given below.

After partially resolving the ambiguities in the reation (3.1) on the basis of χ^2-probability ($P(\chi^2)$) and the ionization; the negative side of distribution of $((MM^2-M^2_{\pi^o})/\Delta MM^2)$, where MM^2, $M^2_{\pi^o}$ and ΔMM^2 respectively are the missing mass squared, mass of π^o squared and the error on the missing mass squared, is fitted with a Gaussian plus a background function. Taking the fitted Gaussian representing the true $1C\pi^o$ component, the total number of $1C\pi^o$ events is estimated. This cross-section is compared with those published for different energies and their energy dependence is estimated.

The narrow width of the ω^o makes the effect of the different ambiguities less important in selecting the $p\omega\pi^+$ channel. Only the unambiguous and the two-fold self-ambiguous events show the ω^o signal. Thus the selection of the ω^o after resolving almost all the ambiguities gives the following three-body final state for further analysis.

$$\pi^+ p \longrightarrow p\omega\pi^+. \qquad (3.2)$$

The background in the reaction (3.2) is estimated by fitting the mass distribution of three pions with a Breit-Wigner function

convoluted with a Gaussian error function. Consistent results are also obtained on the basis of the ω^o-decay matrix element. The production cross-section for the reaction (3.2) thus obtained is compared with those published for different energies.

The three-body Dalitz plot for the reaction (3.2) is given towards the end of the Chapter. The possible quasi-two-body reactions are discussed in the light of the pattern on the Dalitz plot.

Finally, a brief qualitative description of the patterns obtained in longitudinal and transverse momenta corresponding to those seen on the three-body Dalitz plot is given.

3.2 Estimation of the $1C\pi^o$ Cross Section

It is difficult to make a quantitative resolution of the different ambiguities in the kinematic fits to the reaction $\pi^+ p \longrightarrow p\pi^+\pi^+\pi^-\pi^o$. These ambiguities are less important for the study of the $p\omega\pi^+$ final state because of the narrow width of the ω^o. However, for the sake of completeness an estimate of the $1C\pi^o$ cross-section is presented.

The ambiguities fall into the following four categories:

(i) ambiguities with a four-constraint (4C) fit,

(ii) one-constraint neutron (1Cn) ambiguities,

(iii) self-ambiguities,

(iv) no-fit ambiguities (i.e., possible multi π^o events).

These ambiguities were partially resolved on the basis of the χ^2-probability ($P(\chi^2)$) and the ionization. The proton and the pion can be distinguished by eye on the measuring table if laboratory momentum is less than about 1.2 GeV/c (see Section 1.3.4). On the other hand, no particle having laboratory momentum > 1.2 GeV/c can be unambiguously identified as a proton or a pion. The second two

categories of ambiguities occur because the proton could not be identified. But the fourth category is due to experimental error in determining the missing mass.

3.2.1 Ambiguities with a four-constraint (4C) fit

If a $1C\pi^o$ event had a consistent fit to a 4C reaction with $P(\chi^2) \geq 0.1$, the event was assumed to belong to the latter reaction because of the higher constraint for such a reaction. FAKE runs show this to be reasonable [38].

3.2.2 One-constraint neutron (1Cn) ambiguities

If a $1C\pi^o$ event had a consistent fit to a 1Cn reaction with $P(\chi^2) \geq 0.1$, the event was considered to be ambiguous with 1Cn. These events could be one, two and three fold ambiguous $1C\pi^o$ with a 1Cn depending on whether one, two and three $1C\pi^o$ fits to the same reaction were ambiguous with a 1Cn. For all these cases the proton momentum was >1.2 GeV/c and the $1C\pi^o$ hypothesis was accepted if its confidence level ($P(\chi^2)$) was higher than that for the 1Cn. There were 513 such events.

3.2.3 Self-ambiguities

Since in this experiment protons and pions with momenta >1.2 GeV/c cannot be identified by checking the bubble density, ambiguities occur because of the possible permutations of the proton track assignment. For the two-fold and three-fold self-ambiguous events, the one with a greater $P(\chi^2)$ was accepted.

3.2.4 No-fit ambiguities

The $1C\pi^o$ events with $P(\chi^2) \geq 0.1$ ambiguous with no-fit events were accepted as candidates for the former category. This sample

(72% of the total) obviously contains the largest contamination of background events (see Section 3.2.5).

Table (3.1) gives the numbers in the different categories of events.

Table (3.1)

The different categories of events

No. of $1C\pi^o$ events ambiguous with 1Cn events	No. of $1C\pi^o$ unambiguous events	No. of $1C\pi^o$ self-ambiguous events	No. of $1C\pi^o$ events ambiguous with no-fit events	Total
513	2,646	140	8,406	11,705

3.2.5 Estimation of the number of $1C\pi^o$ events

Figure (3.1) shows the distribution of $(MM^2-M_{\pi^o}^2)/\Delta MM^2)$ for all events given in Table (3.1), where MM^2, $M_{\pi o}^2$ and ΔMM^2 respectively are the missing mass squared, mass of π^o squared and the error on the missing mass squared. This distribution should be a Gaussian with a standard deviation ±1 and central value of zero, but in practice is asymmetric, there being more events on the positive (right-hand) side.

As has been mentioned the major contamination would be expected to arise from multi-π^o production (the no-fit events) and qualitatively it is understandable that they should make a major contribution to the positive side of the distribution. The missing mass squared distribution of the no-fit events starts at $MM^2 \sim 4M_{\pi o}^2$. For a particular value MM_c of missing mass for a no-fit event, the measured MM^2 distribution will be the Gaussian:

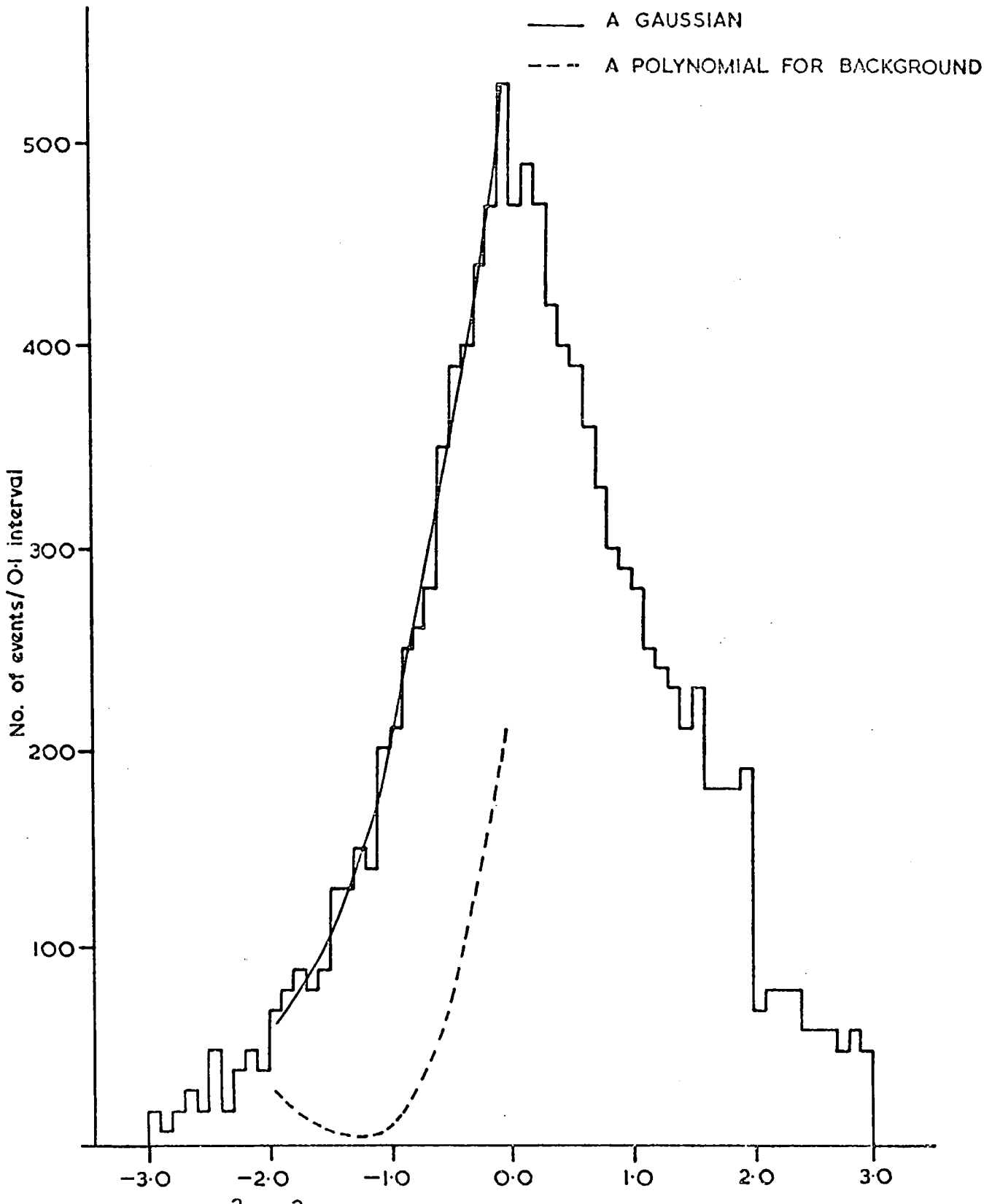

FIG. 3.1 DISTRIBUTION WHERE MM^2, $M^2_{\pi^0}$ AND ΔMM^2 ARE AS EXPLAINED IN THE TEXT —— 11075 EVENTS.

$$N \propto \exp\left(-\left(x - \frac{MM_c^2 - M_{\pi^o}^2}{\Delta MM^2}\right)^2/2\right),$$

where $x = \frac{MM^2 - M_{\pi^o}^2}{\Delta MM^2}$. The value of ΔMM^2 is distributed between $\sim 5M_{\pi^o}^2$ and $15M_{\pi^o}^2$ and hence the no-fit background will contribute an envelope of Gaussians falling rapidly for negative values of x, but having a complex shape for positive values of x. To represent the possible behaviour of the intensity of the background at negative values of x, a third-order polynomial of the form $(C_o + C_1 x + C_2 x^2 + C_3 x^3)$ for the background added to the standard Gaussian expected for true $1C\pi^o$ events for the distribution of Figure (3.1) was fitted between -2 and zero. A confidence level of about 60% with the following parameters for the Gaussian and the polynomial was obtained:

Central value of Gaussian	=	0.005,
σ (standard deviation)	=	±0.98,
C_o	=	229.8 ,
C_1	=	431.8 ,
C_2	=	264.2 ,
C_3	=	48.9 .

Taking the fitted Gaussian as representing true $1C\pi^o$ component, the total number of good $1C\pi^o$ events is estimated as 7690 ± 123. This yields a cross-section of 1.31 ± 0.13 mb, where the quoted error on the cross-section includes the statistical error on the fitted sample plus 10% for the normalization (see Section 2.2).

3.2.6 Energy dependence of the cross-section

Figure (3.2) shows the comparison of the cross-section obtained above with those at different incident momenta for the

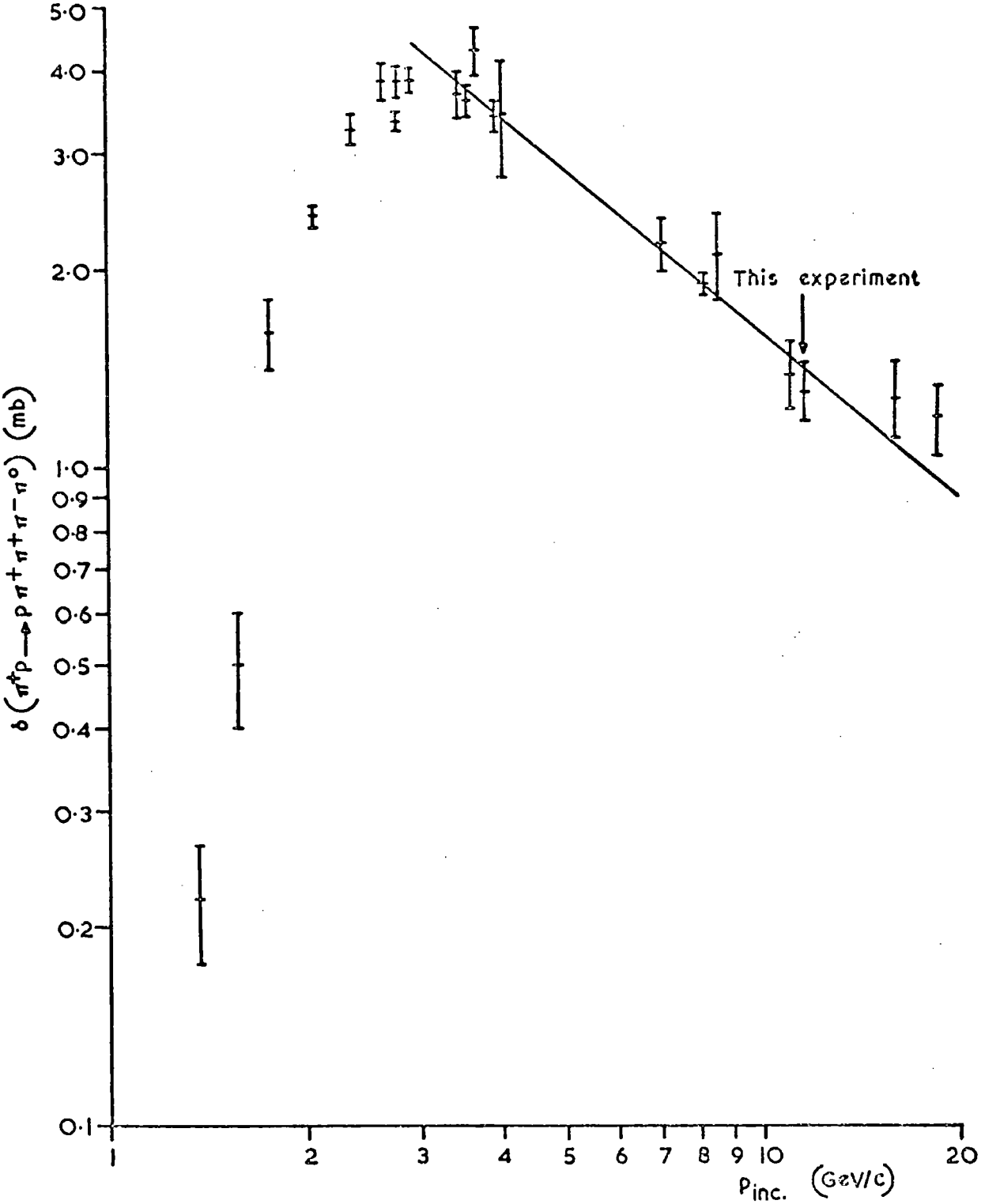

FIG. 3.2 TOTAL CROSS SECTION FOR $\pi^+ p \longrightarrow p\pi^+\pi^+\pi^-\pi^0$ AS A FUNCTION OF LABORATORY MOMENTUM ($p_{inc.}$) OF INCIDENT PION.

reaction $\pi^+ p \longrightarrow p\pi^+\pi^+\pi^-\pi^o$ [39-56]. The following equation was fitted to the experimental points:

$$\sigma = Kp_{inc}^{-n}, \qquad (3.3)$$

where σ is the cross-section in mb, p_{inc} is the laboratory momentum of the incident pion in GeV/c and K and n are constants. The fit was restricted to the data having $p_{inc} > 3.0$ GeV/c because equation (3.3) is clearly not applicable to the experimental points below that momentum. The high momentum points at 16 and 18.5 GeV/c do not appear to be consistent with such a power law behaviour either. In view of the present analysis it is possible that these high momentum points are overestimated. Ballam et al. at 16 GeV/c [54-55], for instance, removed the 4C ambiguities and accepted the fits with a confidence level of greater than 1% having a missing mass squared in the interval of ± 0.11 $(GeV/c^2)^2$ about the π^o mass and $\Delta MM^2 < 0.18$ $(GeV/c^2)^2$. Hones et al. [56] estimated the cross-section by fitting a Gaussian to the negative side of the missing mass squared distribution with a central value of 0.01 $(GeV/c^2)^2$. In both these cases the background contribution due to multi-π^o production has not been taken into account explicitly. Therefore, these points have not been included in the fit. The values of K and n, as obtained from the fit are 10.7 and 0.82 respectively and are compatible with those obtained by the other workers [57].

3.3 Selection of $p\omega\pi^+$ Channel

The narrow width of the ω^o makes the effect of the different ambiguities discussed in Section 3.2 less important in selecting the $p\omega\pi^+$ channel. In this Section it is seen that the χ^2-probability ($P(\chi^2)$) cut off at <0.1 is still reasonable because it is only the events above this cut off that show a clear ω^o signal. The $1C\pi^o$

events ambiguous with 4C, 1Cn and those that are three-fold self-ambiguous do not show the ω^o signal at all. Only the unambiguous and the two-fold self-ambiguous events show the ω^o signal. The three-pion mass distributions for these different categories of events are shown in Figures (3.3) to (3.6).

In subsequent Sections the three-pion mass distribution is discussed and fitted with a convoluted Breit-Wigner. The mass interval between the limits 745 MeV/c^2 < M_ω < 825 MeV/c^2 is selected as containing most of the ω^o. The double ω^o events are resolved on the basis of the ω-decay matrix element and $P(\chi^2)$.

Finally the ω^o Dalitz plot is discussed and the background is estimated from the ω-decay matrix element. Then the cross-section of $p\omega\pi^+$ channel is compared with those published at different energies and their energy dependence is estimated.

3.3.1 The type of events that show a signal for the ω^o-meson

In order to estimate a reasonable cut off for $P(\chi^2)$, while still retaining the major part of the ω^o signal, the region for $P(\chi^2) < 0.1$ was divided into several intervals that gave a resonable number of events and the mass distributions of $M(\pi^+\pi^-\pi^o)$ were examined. There was no obvious ω^o signal for the region of $P(\chi^2) < 0.1$. Figure (3.3) shows the mass distributions of $M(\pi^+\pi^-\pi^o)$. The cross-hatched histogram shows the $\pi^+\pi^-\pi^o$ events for $P(\chi^2) < 0.1$ and that with clear outline is for events with $P(\chi^2) \geq 0.1$ with 2,462 events and 10,910 events respectively.

As discussed in Section (3.2.1), it makes sense to exclude $1C\pi^o$ events ambiguous with 4C. Figure (3.4) shows the mass distribution of $M(\pi^+\pi^-\pi^o)$ for the events rejected because of a 4C ambiguity (647 events). There is no ω^o signal.

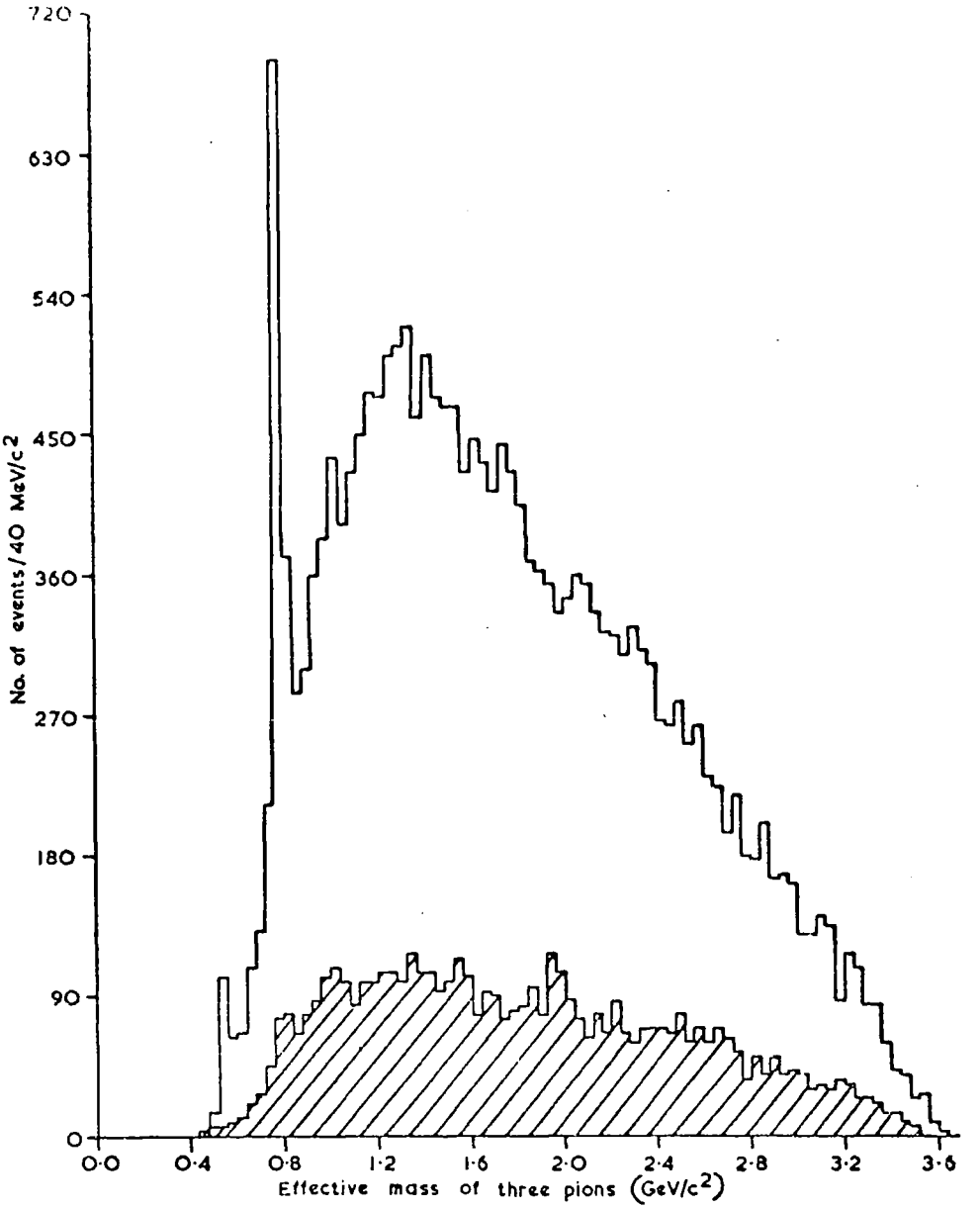

FIG. 3.3 $M(\pi^+\pi^-\pi^0)$ FOR $P(\chi^2) \geq 0{\cdot}1$ (CLEAR OUTLINE — 10,910 EVENTS) AND $P(\chi^2) < 0{\cdot}1$ (CROSS HATCHED — 2,462 EVENTS). THERE ARE TWO ENTRIES PER EVENT.

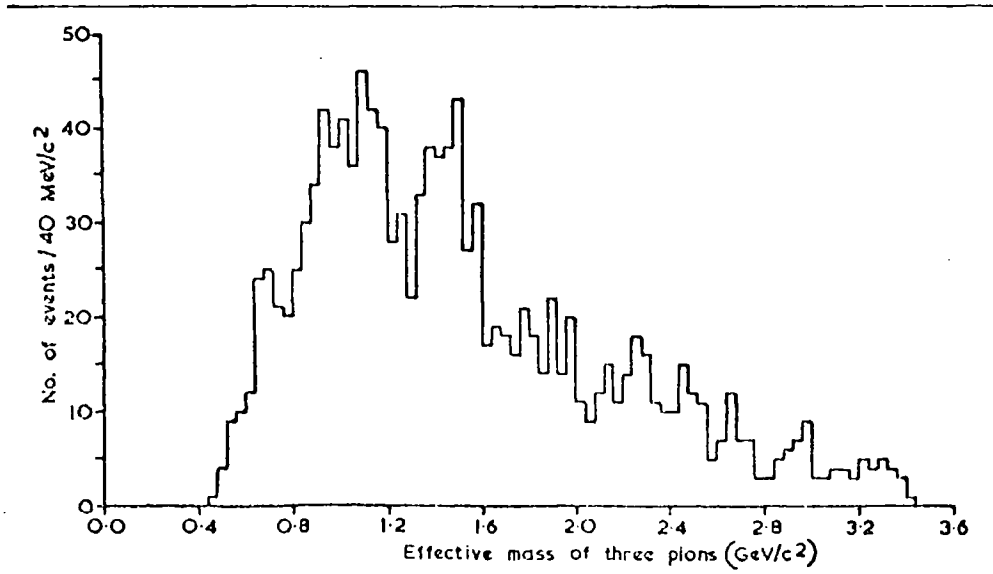

FIG. 3.4 $M(\pi^+\pi^-\pi^0)$ FOR EVENTS REJECTED BECAUSE OF A 4C AMBIGUITY. THERE ARE 647 EVENTS WITH TWO ENTRIES PER EVENT.

Unidentifiable protons (momentum > 1.2 GeV/c) give rise to self-ambiguities and 1Cn ambiguities. Figure (3.5) shows the mass distributions of $M(\pi^+\pi^-\pi^o)$ for events with a neutron ambiguity (clear outline) and those that are three-fold self-ambiguous (cross-hatched) with 976 events and 117 events respectively. There is no clear ω^o-signal in either of these samples and they are therefore rejected.

Figure (3.6) shows the mass distributions of $M(\pi^+\pi^-\pi^o)$ events without self-ambiguity (clear outline) and those that are two-fold self-ambiguous (cross-hatched) with 8,531 events and 639 events respectively. There is a clear signal of the ω^o in both these cases.

There are two possible π^+ mesons that could be combined in the $\pi^+\pi^-\pi^o$, hence in Figures (3.3) to (3.6) both the mass combinations are plotted. It is clear that only the unambiguous and the two-fold self-ambiguous categories of events show the signal for the ω^o-meson.

The two possible combinations of a π^+ meson to give a three-pion mass in the ω^o peak is not a serious problem in this experiment, since such a coincidence only occurs 20 times for the 907 events in the peak. Of the two combinations, the one was chosen which had the greater value of ω^o- decay matrix element (see Section 3.3.3).

3.3.2 Analysis of the mass spectrum in the ω^o region

Figure (3.7) shows the three-pion mass plot in 10 MeV/c^2 intervals from threshold through the region of the ω^o peak and up to 1.3 GeV/c^2. Clearly all the events between 0.70 - 0.87 GeV/c^2 are not due to the presence of the ω^o meson since the form of the spectrum on either side of the peak makes it obvious that the ω^o signal stands on a continuous background spectrum. It would be

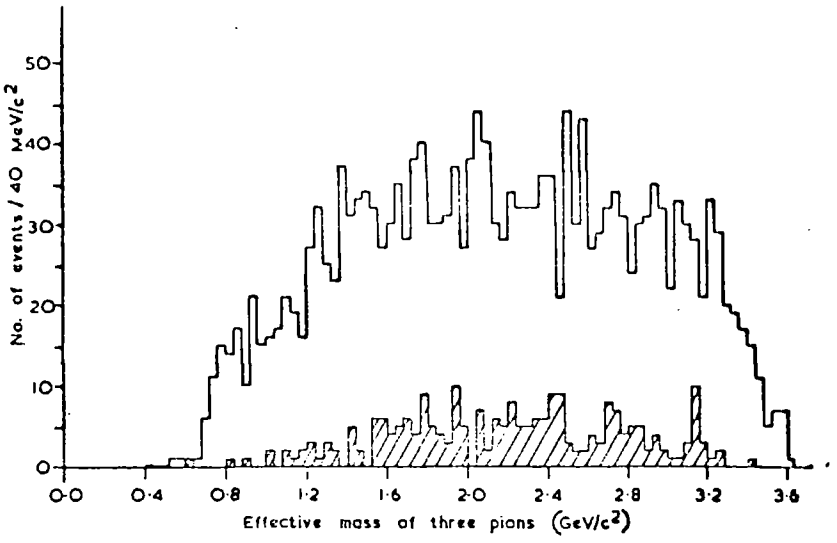

FIG. 3.5 $M(\pi^+\pi^-\pi^0)$ FOR EVENTS WITH A NEUTRON AMBIGUITY (CLEAR OUTLINE — 976 EVENTS) AND THOSE THAT ARE 3-FOLD SELF-AMBIGUOUS (CROSS HATCHED — 117 EVENTS). THERE ARE 2 ENTRIES PER EVENT.

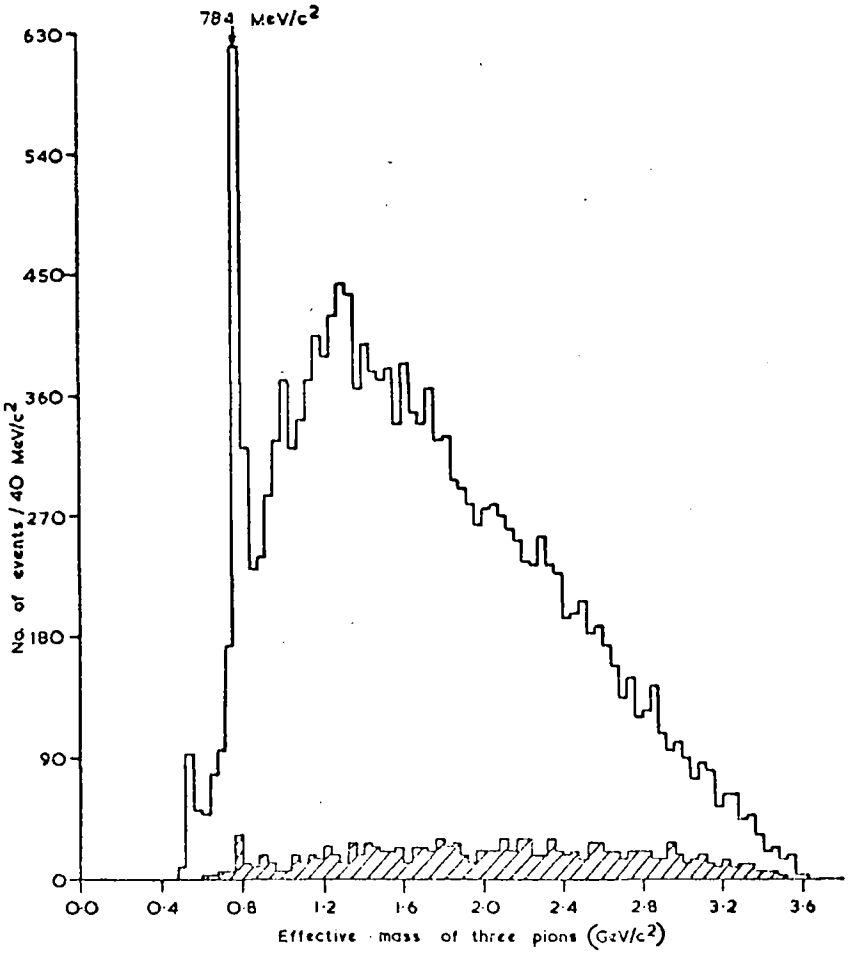

FIG. 3.6 $M(\pi^+\pi^-\pi^0)$ FOR UNAMBIGUOUS EVENTS (CLEAR OUTLINE — 8,531 EVENTS) AND THOSE THAT ARE 2-FOLD SELF-AMBIGUOUS (CROSS HATCHED — 639 EVENTS). THERE ARE TWO ENTRIES PER EVENT.

possible to make an exact analysis of the mass spectrum of Figure (3.7) if the shapes of the ω^o peak and the background spectrum were known.

The shape of the background spectrum depends on the three-pion masses that arise by random association from all those final states not containing an ω^o meson. Since the details of all such states are not known, it is not possible to calculate the background spectrum and for the present analysis, a linear background through the small mass interval across the ω^o peak will be assumed.

In the absence of the experimental error, the shape of the ω^o-mass spectrum is given by a Breit Wigner function (see Section 2.3). From a consideration of the measurement errors in the present experiment, one would expect an error of about ± 15 MeV/c^2 on a three-pion mass in the ω^o region†. This is large as compared with the value of Γ_o, the full width at half height, but not large enough to convert the original Breit-Wigner into a Gaussian distribution. Attempts to fit the distribution of Figure (3.7) with a simple Gaussian and a linear background consistently lead to confidence levels of less than 1%.

A confidence level of about 30% is obtained by convoluting a Gaussian of standard deviation of 12.5 MeV/c^2 with the ω^o Breit-Wigner (see equations (2.5 - 2.6)) having m_o = 785 MeV/c^2 and

---

† $MM^2 = ME^2 - MP^2$,

$\Delta MM^2 = 2MM\Delta MM$,

$\Delta MM = \Delta MM^2/2MM$, or

$\Delta MM \propto \Delta MM^2$ for a small variation of MM,

where MM^2, ME^2, MP^2, ΔMM and ΔMM^2 respectively are missing mass squared, missing energy squares, missing momentum squared, error on missing mass and error on missing mass squared.

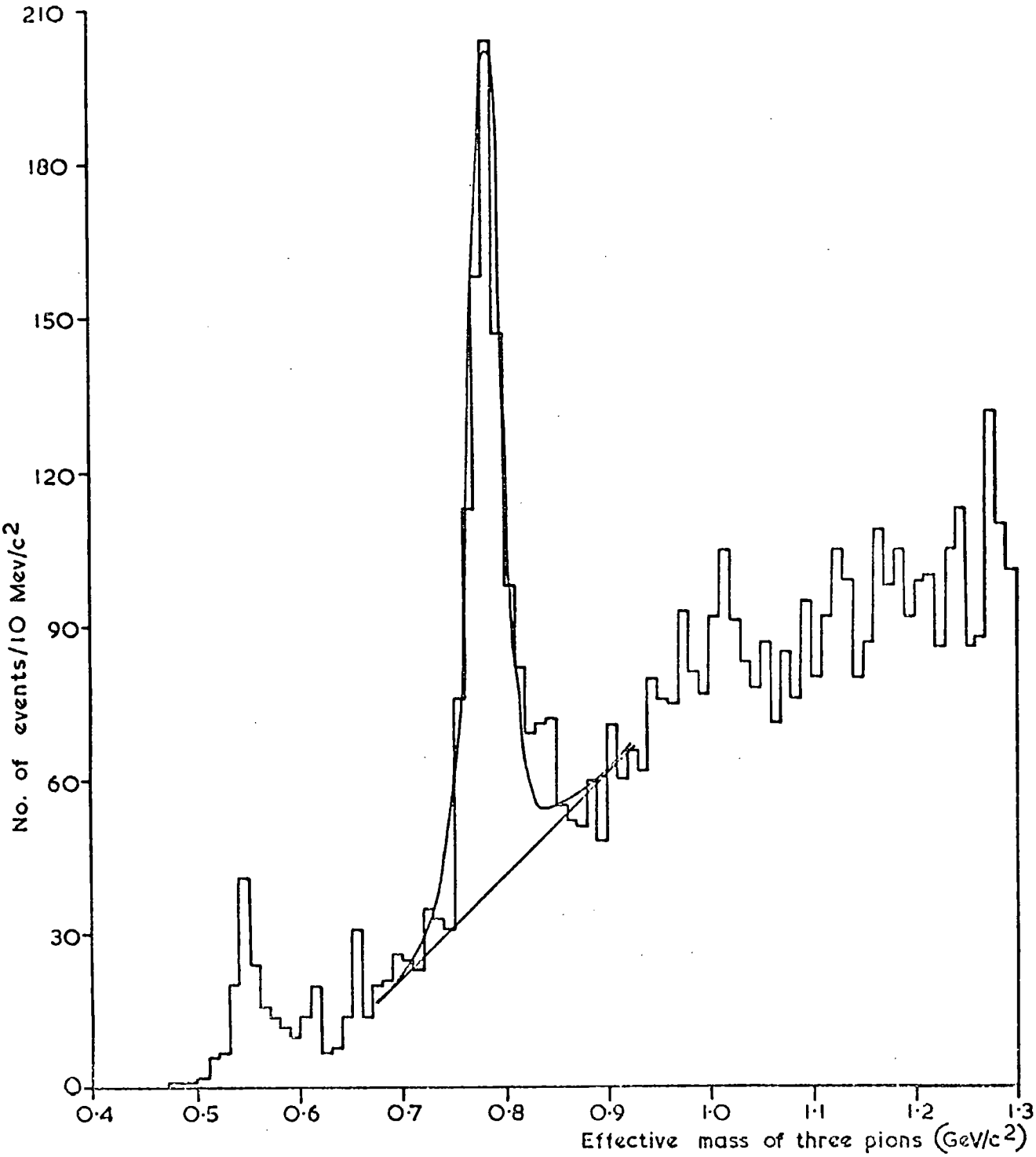

FIG. 3.7 $M(\pi^+\pi^-\pi^0)$ FOR UNAMBIGUOUS AND 2-FOLD SELF-AMBIGUOUS EVENTS. (2702 EVENTS UP TO 1·3 GEV/c^2 WITH TWO ENTRIES PER EVENT). THE CURVE IS A FIT TO THE DATA AS EXPLAINED IN THE TEXT.

Γ_o = 10 MeV/c^2 and combining the result with the linear background shown in Figure (3.7). The resulting fitted curve is shown in the figure. The total number of the ω^o meson entries above the background required for the fit is 665 ± 25. For later analysis the mass interval 745 MeV/c^2 < M_ω < 825 MeV/c^2 was selected as defining the ω^o events. There are 927 entries in this region and the above fit to data requires these to consist of 621 ± 25 true ω^o mesons with 306 ± 17 entries (33%) in the non-resonant background. The defined mass region thus includes 93% of the total number of the ω^o mesons as deduced by the above fit.

3.3.3 The ω^o Dalitz plot

Figure (3.8) shows the triangular Dalitz plot for the ω^o mass band (745-825 MeV/c^2). The Dalitz variables in the ω^o rest frame are:

$$\left.\begin{aligned} X &= \frac{T_+ - T_-}{Q\sqrt{3}}, \qquad \text{(a)} \\ \text{and} \quad Y &= T_o/Q, \qquad \text{(b)} \end{aligned}\right\} \quad (3.4)$$

where

T_n = kinetic energy of the pion with charge n, and

Q = available energy = $M_\omega - (M_{\pi^+} + M_{\pi^-} + M_{\pi^o})$

= $T_+ + T_- + T_o$ = Height of the triangle.

The Q value varies from event to event due to the finite width of the resonance. Therefore, the normalized variables T_+/Q, T_-/Q and T_o/Q are more appropriate to work with. Most of the events are concentrated at the centre and the density of the points decreases radially as expected.

There is no way to distinguish the true ω events from the

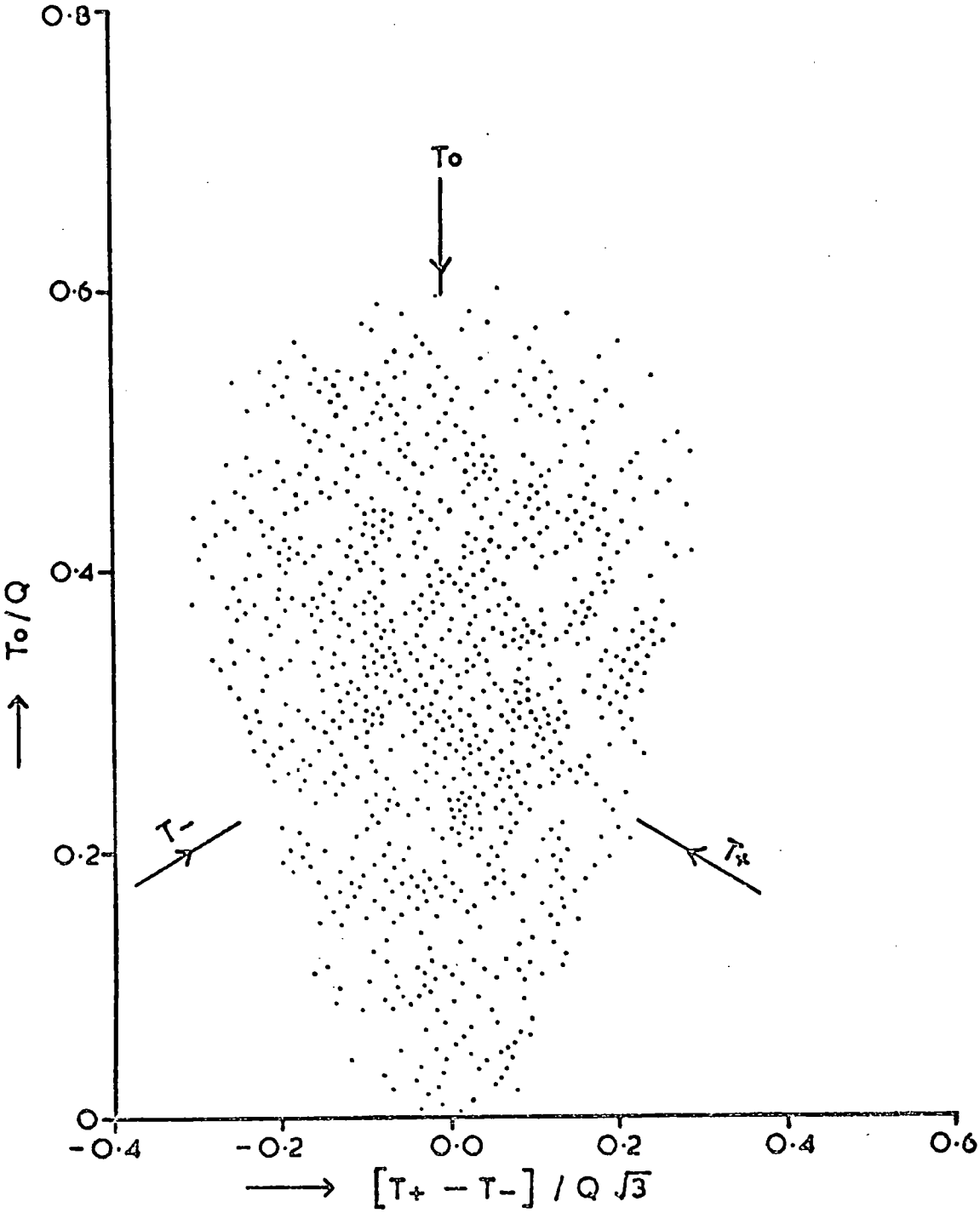

FIG. 3.8 DALITZ PLOT FOR THE ω^0 (907 EVENTS).

non-resonant background experimentally on an individual basis. However, the properties of the ω-decay matrix element as given below can be utilized to estimate the background.

The normalized ω-decay matrix element squared is [58]:

$$\lambda_\omega = \frac{|\vec{p}_+ \times \vec{p}_-|^2}{\frac{3}{4}\left[\frac{M_{3\pi}^2}{9} - m_\pi^2\right]^2}, \tag{3.5}$$

where $\vec{p}_\pm$ is the $\pi^\pm$-momentum in the (3π) C.M. system. The λ_ω so defined is normalized to the limits:

$$0 \leq \lambda_\omega \leq 1 .$$

The distribution of the three-pion decay states as a function of λ_ω is given by:

$$dN/d\lambda_\omega \propto \lambda_\omega , \tag{3.6}$$

being maximum for $\lambda_\omega = 1$ and zero for $\lambda_\omega = 0$; dN is the number of events.

The values of $\lambda_\omega = 1$ and 0 correspond to the centre and periphery respectively of the Dalitz plot of the three pions. The non-resonant background, if assumed uniform in phase space, is uniformly distributed in λ_ω as well. Hence, the higher the value of λ_ω the more likely it is that the event represents a true ω^o rather than background.

Equation (3.6) is modified to account for the background as follows:

$$dN/d\lambda_\omega = A + B\lambda_\omega , \tag{3.7}$$

where A and B are constants.

Figure (3.9) shows the λ_ω distribution for the selected $p\omega\pi^+$ channel. Equation (3.7) was fitted to this distribution and the fitted parameters are:

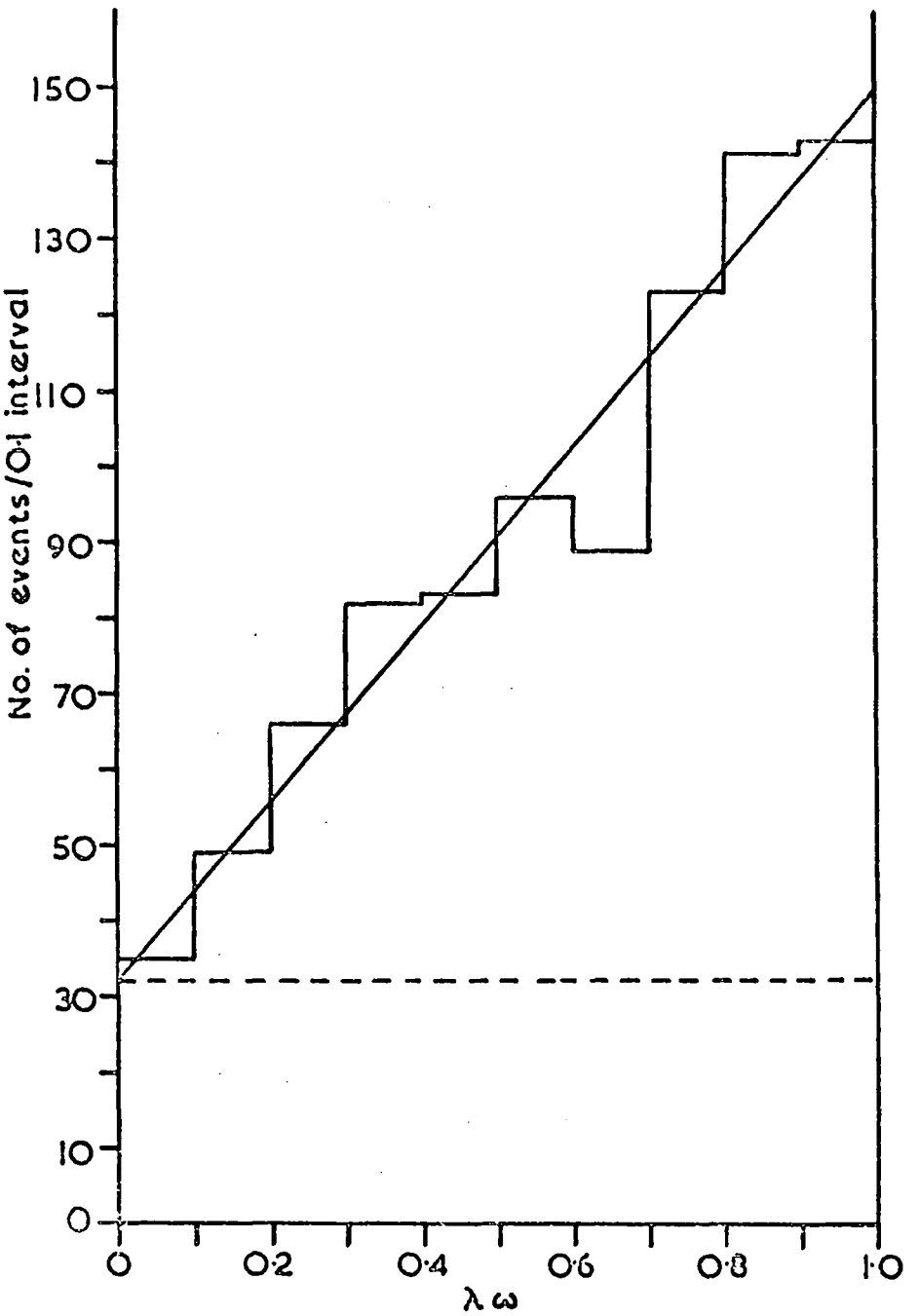

FIG. 3.9 DECAY MATRIX ELEMENT OF THE $\omega^0(\lambda\omega)$ DISTRIBUTION— 907 EVENTS. THE STRAIGHT LINE IS A FIT TO THE DATA AS EXPLAINED IN THE TEXT.

$$A = 31.9 \pm 2.9,$$

$$B = 118.1 \pm 6.0.$$

The solid line shows the fitted equation (3.7) and the dashed line gives the estimate of about 35% background. This is consistent with what was deduced in Section 3.3.2.

3.4 Cross-section for $p\omega^o\pi^+$ Channel

From Section 3.3.2 it is seen that the three-pion mass spectrum is consistent with the presence of 621 ± 25 ω^o mesons in the mass band (745 - 825 MeV/c^2) and Section 3.3.3 shows that the kinematic distribution of three pions in the central region of the ω^o mass is consistent with that expected from the ω^o-decay matrix element and a uniformly distributed non-resonant background. The corresponding cross-section is 0.103 ± 0.01 mb. The error includes the uncertainty on the estimate of the number of the ω^o mesons obtained above and on the overall normalization of the experiment (see Section 2.2). Adding 10% each for cut off on $P(\chi^2)$ at 0.1 and for unseen decay modes of the ω^o-meson and 7% for the ω^o mesons outside the selected mass interval (see Section 3.3.2), the cross-section becomes:

$$\sigma\ (\pi^+ p \rightarrow p\omega\pi^+) = 0.134 \pm 0.013 \text{ mb}.$$

Figure (3.10) shows the comparison of this cross-section with those obtained at different incident momenta [40,42-44,46,49-50, 59-61]. The experimental points are fitted by the function: $\sigma = K p_{inc}^{-n}$ (see equation (3.3)). The values of K and n, as obtained from the fit†, are 5.57 and 1.41 respectively and these are in good agreement with those obtained by other workers [57].

---

† The fit was restricted to the data having $p_{inc} > 3.0$ GeV/c.

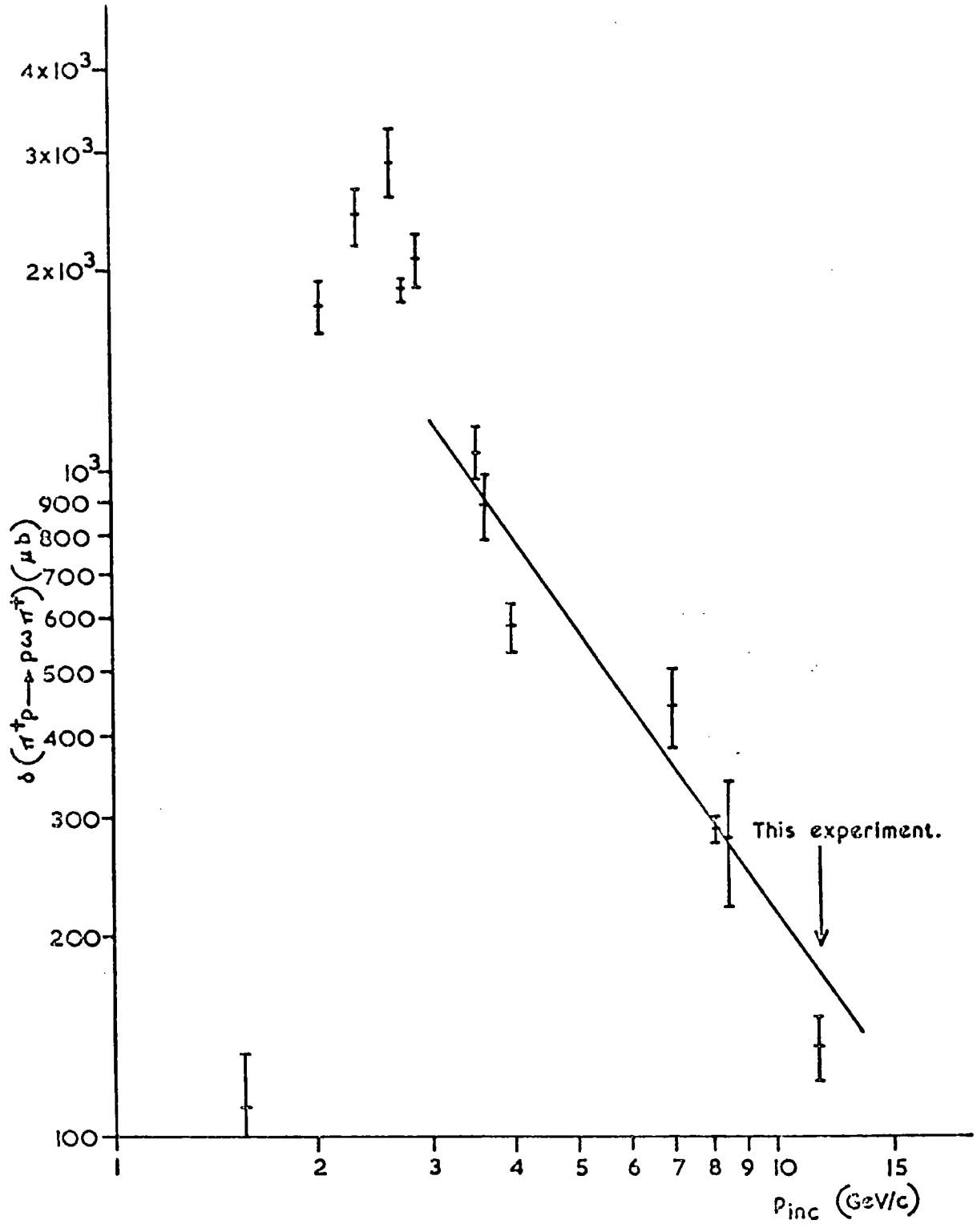

FIG. 3.10 TOTAL CROSS SECTION FOR $\pi^+ p \rightarrow p\omega\pi^+$ AS A FUNCTION OF LABORATORY MOMENTUM (p_{inc}) OF INCIDENT PION.

3.5 The Dalitz Plot for $p\omega\pi^+$ Channel

Figure (3.11) shows the triangular Dalitz plot for $M^2(p\omega)$ versus $M^2(\omega\pi^+)$, where $M^2(p\omega)$ and $M^2(\omega\pi^+)$ respectively are the effective mass squared of $(p\omega)$ and $(\omega\pi^+)$†. The Cartesian coordinates for the Figure (3.11) are given below:

$$\left.\begin{aligned} X &= \frac{2M^2(p\omega) + M^2(\omega\pi^+)}{\sqrt{3}}, \qquad \text{(a)} \\ Y &= M^2(\omega\pi^+). \qquad \text{(b)} \end{aligned}\right\} \quad (3.8)$$

The height of the triangle in Figure (3.11) is equal to: $s + M_p^2 + M_\omega^2 + M_{\pi+}^2 = M^2(p\omega) + M^2(\omega\pi^+) + M^2(p\pi^+)$, where $s^{\frac{1}{2}}$ is the C.M. energy.

The possible projections of this plot are shown as the effective mass distributions in Figures (3.12 a-c). These distributions clearly show the presence of at least the following quasi-two-body reactions:

$$\pi^+ p \longrightarrow \omega^o \Delta^{++},$$

$$\pi^+ p \longrightarrow p B^+.$$

The Δ^{++} (1236) is very strong in the mass distribution of $(p\pi^+)$ and the B^+ (1235) in the effective mass of $\omega\pi^+$ is clearly seen. Whether or not the mass enhancement of $M(\omega p)$ below 2 GeV/c^2 is a resonance will be discussed later. However, its signal is the weakest. In the Dalitz plot of Figure (3.11), the B^+ can be seen as a horizontal band, the Δ^{++} and $M(\omega p)$ are seen as the bands

---

† Instead of using the effective mass squared of a pair of particles, the kinetic energy of the third particle in the C.M. system can be used to obtain a Dalitz plot, since these two variables are linearly dependent.

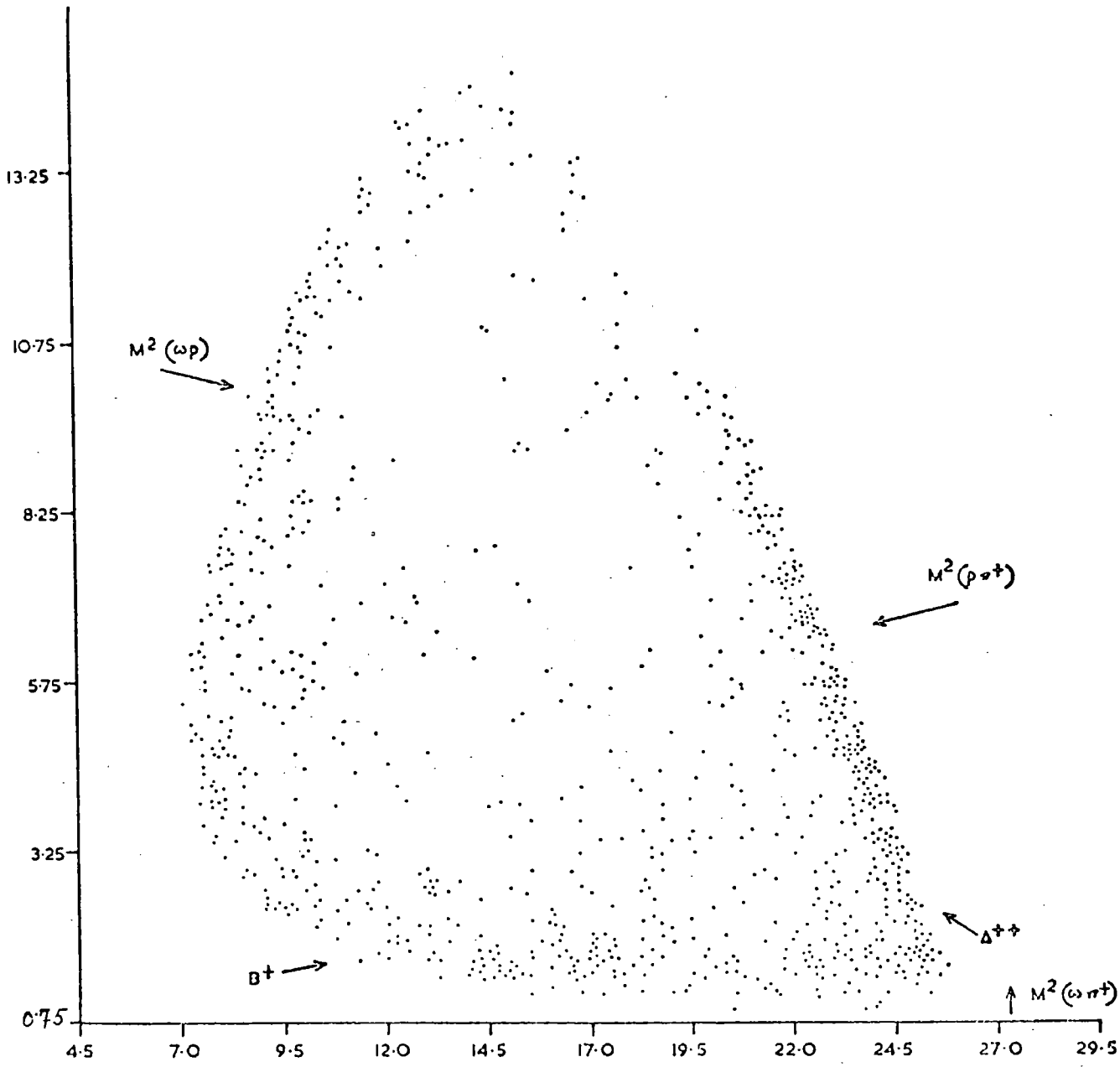

FIG. 3.11 DALITZ PLOT FOR $p\omega\pi^+$ CHANNEL (907 EVENTS).

parallel to the right and the left sides of the boundry of the plot as marked by the symbols B^+, Δ^{++} and (ωp) respectively.

If the matrix element for the final state is constant, phase space predicts a uniform population of points on a Dalitz plot. Inspection of Figure (3.11) shows that apart from the following quasi-two-body reactions:

$$\pi^+ p \longrightarrow \omega\Delta^{++},$$
$$\pi^+ p \longrightarrow pB^+,$$

there is a concentration of points at the low effective mass of $(p\omega)$. The number of events that does not contribute towards the quasi-two-body final state reactions is far more than the estimated number of non-resonant background in the three-pion state accepted as the ω^o mesons in the $p\omega\pi^+$ final state (see Section 3.3).

At the high energy of the present experiment the large orbital angular momentum also affects the uniform population of points on the Dalitz plot. The areas corresponding to the states of low relative momentum between pairs of particles will be depopulated on the Dalitz plot. This effect has depopulated the top-right-hand corner and the centre of the Dalitz plot. On the other hand the bottom-right-hand corner shows a clustering of events because of overlap of the B^+ and the Δ^{++}.

3.6 The C.M. Longitudinal Versus C.M. Transverse Momenta Plots for $p\omega\pi^+$ Final State

Before considering the quasi-two-body final states in detail, a brief qualitative description will be given of the patterns obtained in longitudinal and transverse momenta corresponding to those seen on the Dalitz plot of Figure (3.11).

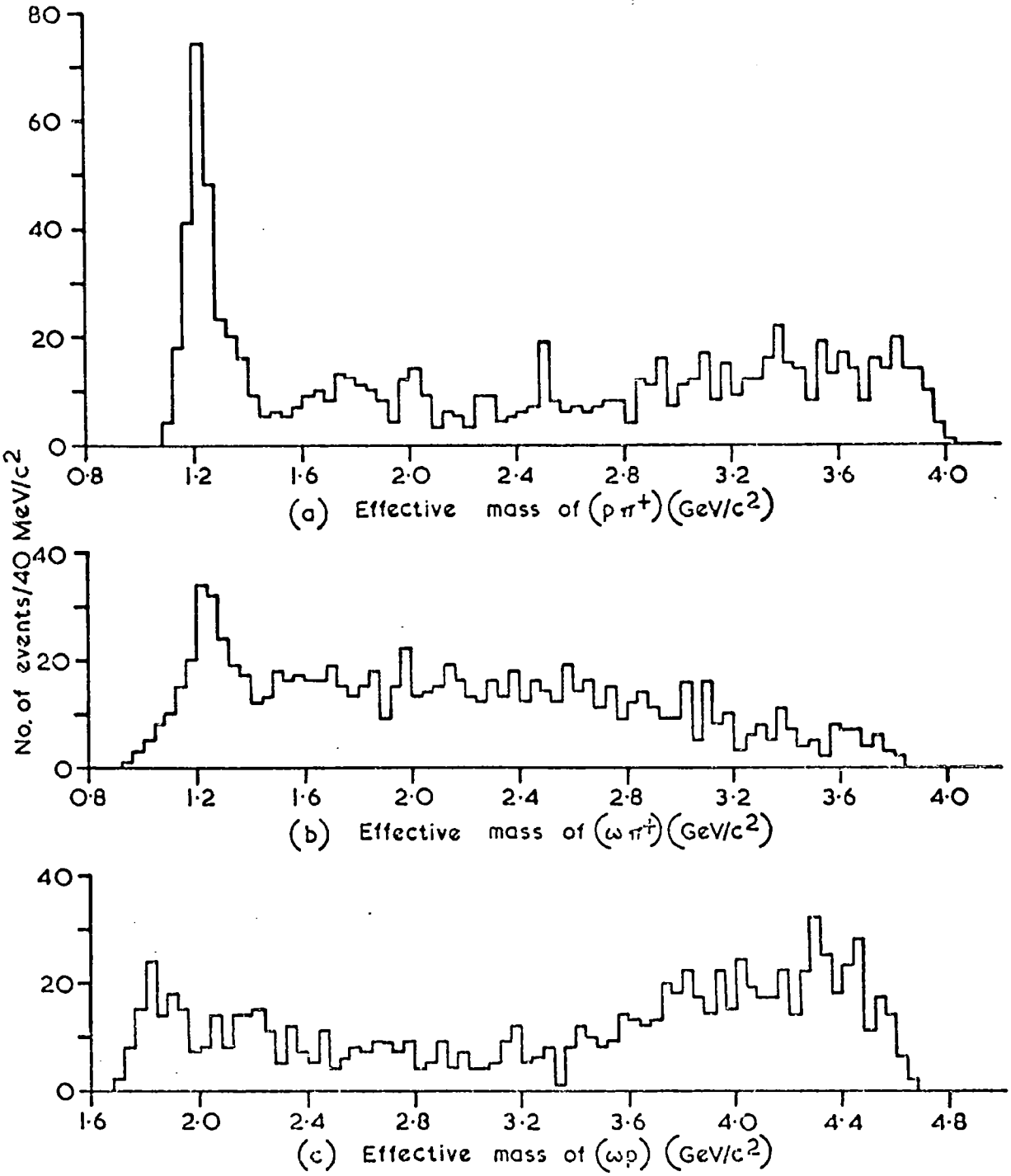

FIG. 3.12 (a) $M(p\pi^+)$, (b) $M(\omega\pi^+)$, (c) $M(\omega p)$ FOR 907 EVENTS ON THE DALITZ PLOT OF FIG. 3.11.

The C.M. longitudinal momentum (along the beam direction) versus the C.M. transverse momentum for the proton, the ω^{o} and the π^{+} meson (sometimes called the Peyrou plots) are given respectively in Figures (3.13) to (3.15). One finds some intensity for the small longitudinal momentum for the π^{+} and the ω^{o}, but the intensity for the proton falls off almost linearly with longitudinal momentum. There is a concentration of events for backwards and forwards production of the proton and the ω^{o} respectively. This shows the double resonance production of the $\omega\Delta^{++}$ at low four-momentum transfer. The forward ω^{o} and π^{+} events with not very high longitudinal momenta arise from the $B^{\pm}$ production. The areas where these events fall are marked on Figures (3.14) and (3.15).

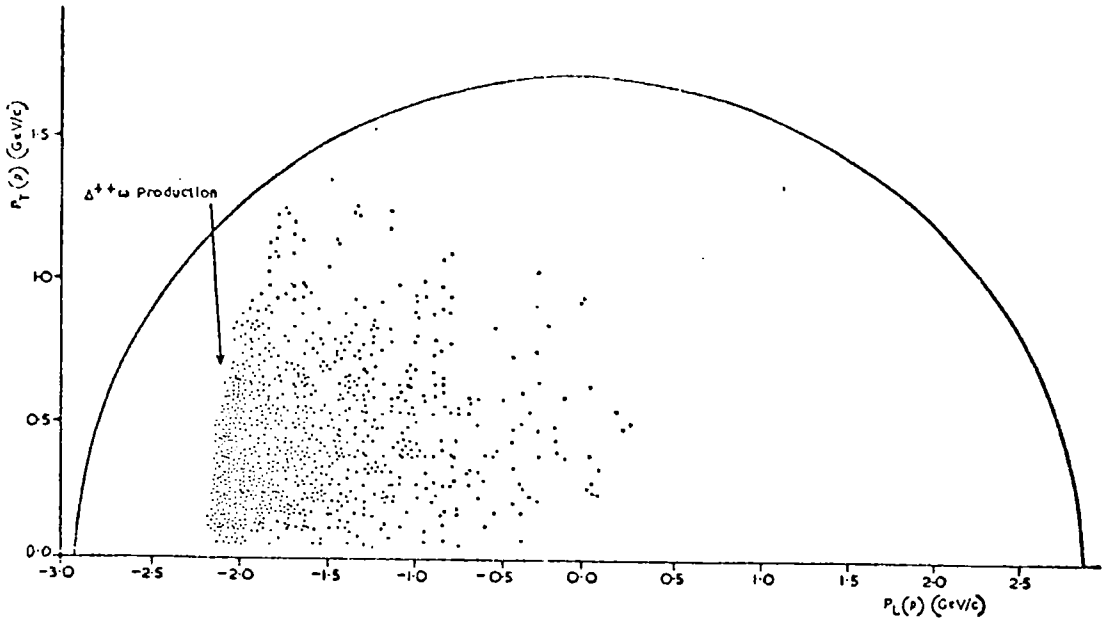

FIG. 3.13 THE C.M. LONGITUDINAL VS C.M. TRANSVERSE MOMENTA FOR THE PROTON — 907 EVENTS

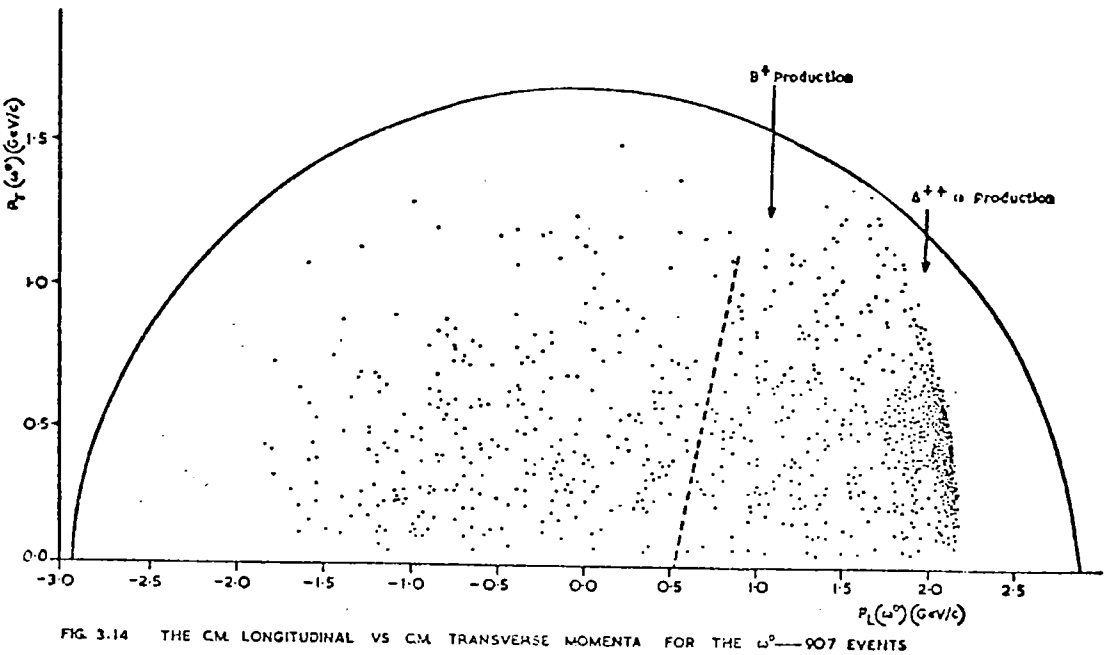

FIG. 3.14 THE C.M. LONGITUDINAL VS C.M. TRANSVERSE MOMENTA FOR THE ω^0 — 907 EVENTS

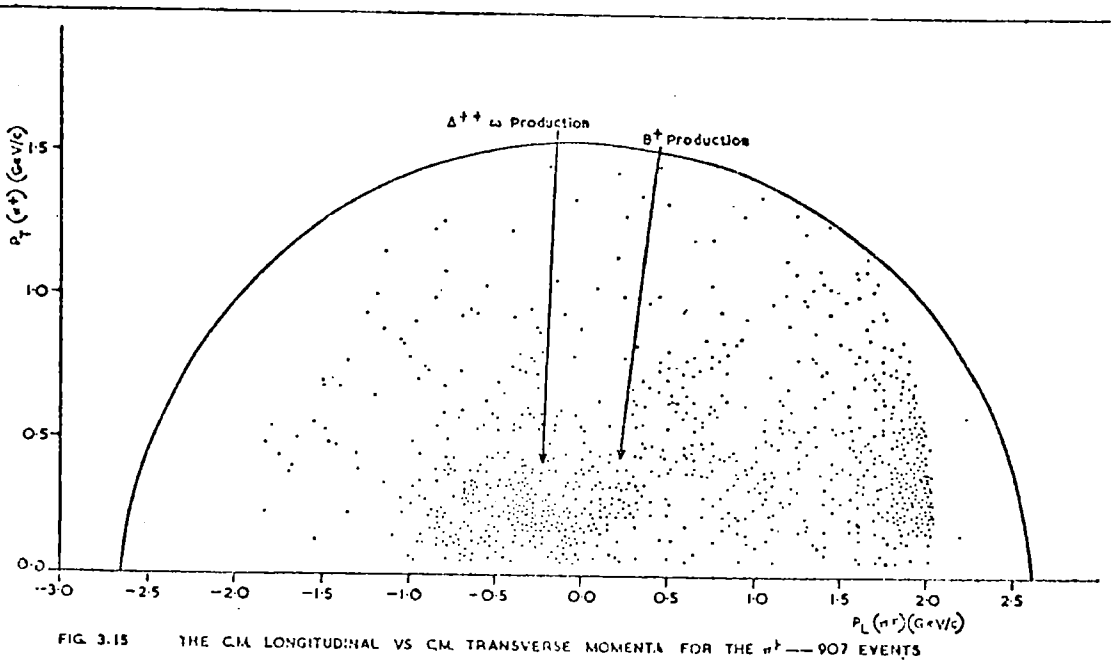

FIG. 3.15 THE C.M. LONGITUDINAL VS C.M. TRANSVERSE MOMENTA FOR THE π^+ — 907 EVENTS

CHAPTER 4

THE $\omega^{o}\Delta^{++}$ FINAL STATE

4.1 Introduction

The reaction

$$\pi^{+}p \longrightarrow \omega^{o}\Delta^{++}(1236), \qquad (4.1)$$

has been studied by several workers at different energies [3, 42-43, 45-46, 50-51, 62-72]. But the situation regarding the production mechanism is still not clear. The possible exchanged particles are the ρ and the B mesons (see Section 2.7.1).

The first two Sections present the total and the differential cross sections for the $\omega^{o}\Delta^{++}$ production.

The next Section gives the spin density matrix elements for the ω^{o} and the Δ^{++} spectra in different frames of reference. Then the positivity conditions for the spin density matrix elements are discussed.

Using the spin density matrix elements, the decay angular distributions for the ω^{o} and the Δ^{++} spectra in different frames of reference are fitted with simple functions.

The next Section deals with the natural and the unnatural parity exchange components.

This is followed by the joint decay correlations. Then the Donohue inequalities and the moduli of the transversity tensors will be presented. Finally the results are discussed.

4.2 Total Cross Section

Figure (4.1) shows the mass distribution of $M(p\pi^{+})$ for events in the $p\omega\pi^{+}$ channel (clear outline) and those that have $|t| \leq 1.0$ $(GeV/c)^{2}$ (cross-hatched) with 907 and 487 events respectively.

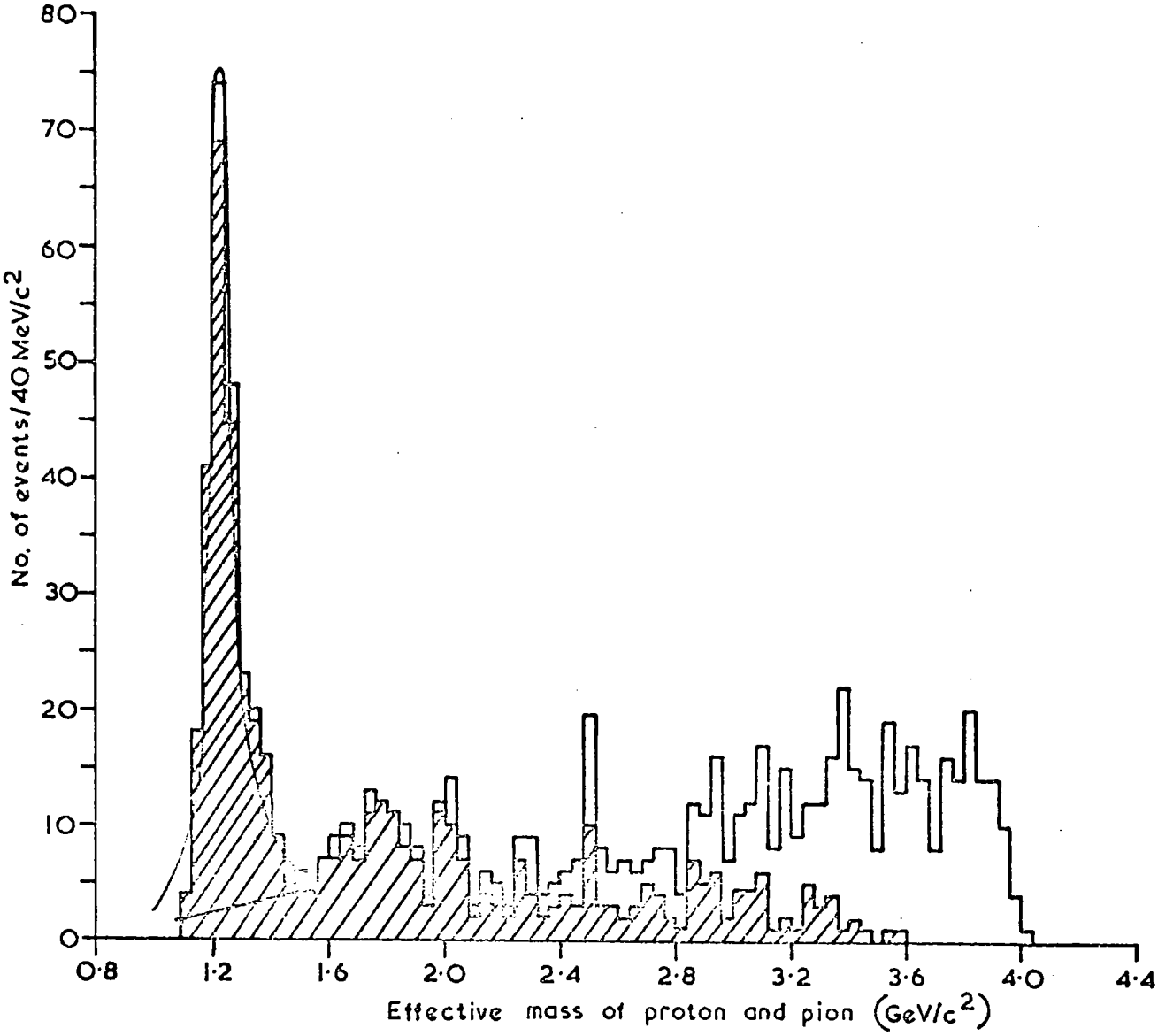

FIG. 4.1 $M(p\pi^+)$ FOR EVENTS IN THE $p\omega\pi^+$ CHANNEL (CLEAR OUTLINE—907 EVENTS.) AND THOSE WITH $|t|(p/\Delta^{++}) \leq 1{\cdot}0\,(\mathrm{GeV/c})^2$ (CROSS HATCHED—487 EVENTS.) THE CURVE IS A FIT TO THE DATA AS EXPLAINED IN THE TEXT.

Here $|t|$ is the four-momentum transfer from the incident proton to the Δ^{++}.

Table (4.1) gives the mass and width of the Δ^{++} as obtained by fitting the mass distribution of $M(p\pi^+)$ (Figure(4.1), cross-hatched), with a p-wave relativistic Breit Wigner (see equations (2.2) to (2.4)), folded with a resolution function (standard deviation, $\sigma_{res} = \pm 10$ MeV) as described by Coyne et al. [73]. The shape of the background is estimated by eye.

Table (4.1)

Mass and width of the Δ^{++}

Reaction	Particle	Mass(MeV/c^2)	Γ(MeV/c^2)	σ(μb)	Background
$\pi^+ p \longrightarrow \omega\Delta^{++}$	Δ^{++}	1234 ± 8	122 ± 32	53 ± 10	∿5%

The errors on the mass and width are worked out by using equation (2.7). The fit was restricted to the $M(p\pi^+) < 1.48$ GeV/c^2. For the subsequent analysis, the mass interval of 1.13 to 1.34 GeV/c^2 as the Δ^{++} was used.

The background, assumed to be linear, is about 5% in the fitted region and there are 240 events above the background. Thus the $\omega\Delta^{++}$ cross-section based on the number of events in Figure (4.1), is (see Section 2.2):

$$\sigma\ (\omega\Delta^{++}) = 41 \pm 8\ \mu b.$$

The error includes the statistical error on the $\omega\Delta^{++}$ events plus 10% for the normalisation. Correcting 10% each for the $P(\chi^2)$ cut off and the unseen ω^o decay modes and 7% for the tails of the ω^o (see Section 3.3.2), the cross-section becomes:

$$\sigma\ (\omega\Delta^{++}) \ = \ 53 \pm 10\ \mu b.$$

Figure (4.2) shows the comparison of this cross-section with those obtained at different incident momenta [42-43, 45-46, 51, 63-68, 70-72]. The experimental points are fitted by the function: $\sigma = K\ p_{inc}^{-n}$ (see Equation 3.3). The values of K and n, as obtained from the fit are 5.8 and 1.85 respectively and are in good agreement with those obtained by other workers for non-strange meson exchange reactions [74,75,76].

4.3 Differential Cross Section

Figures (4.3) and (4.4) show the differential cross sections for the reaction (4.1) as functions of four-momentum transfer $|t|$ and $|t'| = |t-t_{min}|$ respectively, where $|t|$ is the four-momentum transfer from the incident proton to the Δ^{++} and t_{min} is the minimum value of the $|t|$. The events on which the graphs are based are selected in the Δ^{++} mass band:

$$1.13\ GeV/c^2 < M(\Delta^{++}) < 1.34\ GeV/c^2.$$

The transformation to a cross-section is obtained by normalizing the total area to 53 μb which includes all necessary corrections (see Section 4.2). The vertical error bars shown are only those due to statistics since an error in the normalization will not change the shape of the differential cross-section as a function of $|t|$ or $|t'|$. The horizontal error bars represent the intervals chosen.

There are dips in $d\sigma/d|t|$ or $d\sigma/d|t'|$ distributions as $|t|$ (or $|t'|$) $\longrightarrow$ 0. However, there is no reason to suspect the loss of events at $|t|$ (or $|t'|$) $\longrightarrow$ 0, because in the $|t'|$ region of $\lesssim 0.04\ (GeV/c)^2$, the minimum proton momentum is 0.22 GeV/c, which corresponds to a range of about 4 cm in liquid hydrogen. Dips in

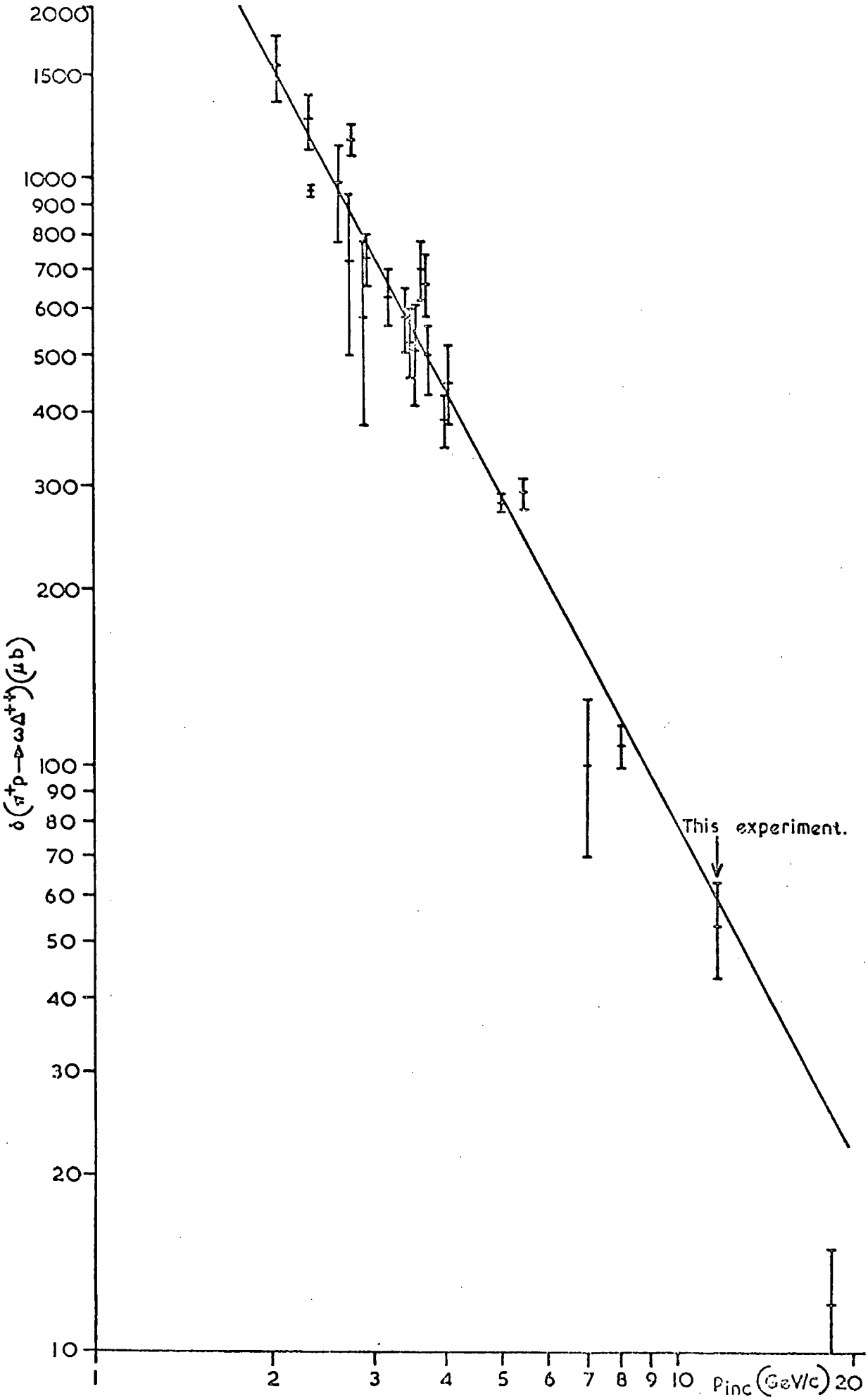

FIG. 4.2 TOTAL CROSS SECTION FOR $\pi^+p\to\omega\Delta^{++}$ AS A FUNCTION OF LABORATORY MOMENTUM (p_{inc}) OF INCIDENT PION.

$d\sigma/d|t'|$ distribution as $|t'| \longrightarrow 0$ have also been reported in other experiments [66,70,51,72] at 3.7, 5.45, 8.0 and 18.5 GeV/c.

Above the region $|t'|$ (or $|t|$) ~ 0.2 $(GeV/c)^2$, $d\sigma/d|t'|$ and $d\sigma/d|t|$ distributions fall sharply with increasing $|t'|$ (or $|t|$) and are consistent with an exponential behaviour $e^{-b|t'|}$ (or $e^{-b|t|}$) with a value of $b = 4.2$ GeV^{-2}. This exponent is compatible with those obtained in other experiments at different energies as listed in Table (4.2).

Table (4.2)

Exponential fit to the differential cross sections

Experiment (GeV/c)	Exponent b (GeV^{-2})	Reference
2.9 - 4.08	3.3	[64]
3.7	4.02	[66]
5.0	4.3	[68]
5.0	3.7	[69]
5.45	3.96	[70]
11.7	4.2	This experiment

The values of the slope b remain fairly constant over a large range of energy. This implies that there is no energy dependence on the value of b.

The exponential shape of $d\sigma/d|t'|$ is too sharp to assume it depends only on the ρ propagator. This can be seen in Figure (4.4) where the dotted curve shows the function $\left(\frac{1}{m_\rho^2 + |t'|}\right)^2$ normalized to the general behaviour of the experimental points at $|t'| \simeq 0.4$.

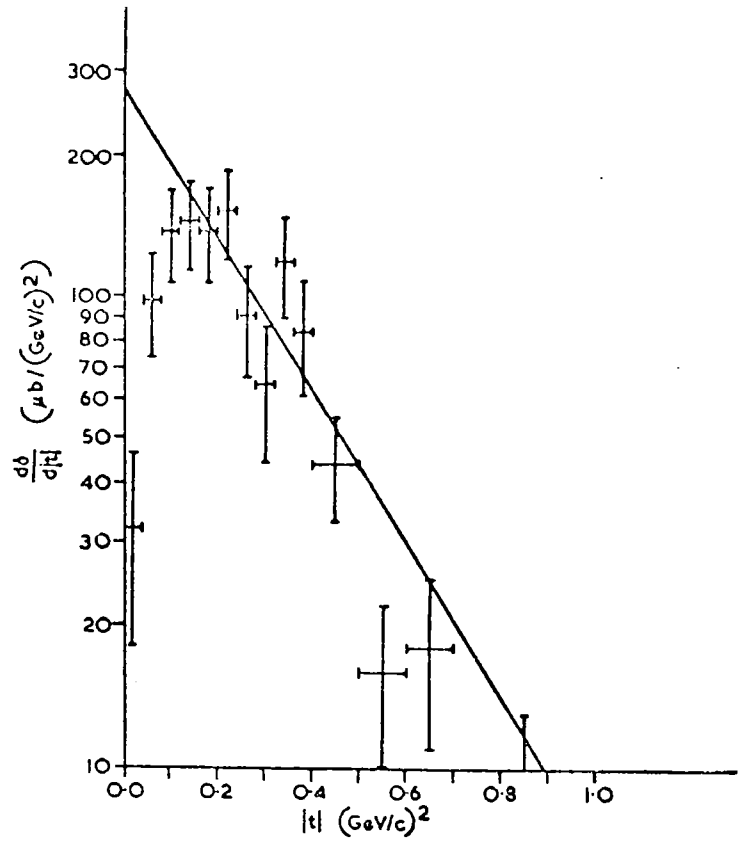

FIG. 4.3 DIFFERENTIAL CROSS SECTION $\frac{d\delta}{d|t|}$ AS A FUNCTION OF $|t|$ FOR $\pi^+ p \rightarrow \omega \Delta^{++}$.

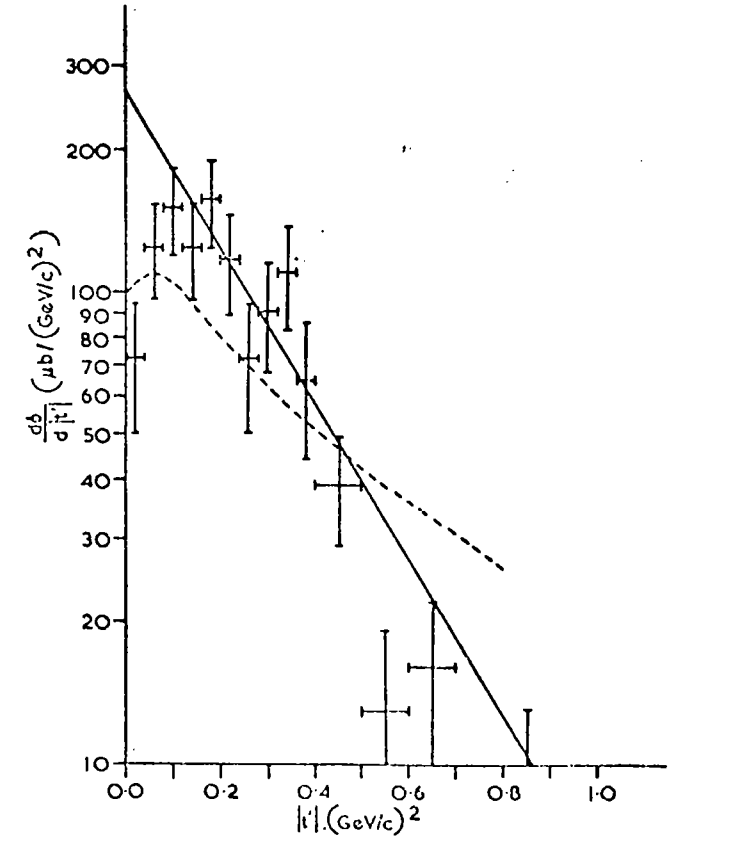

FIG. 4.4 DIFFERENTIAL CROSS-SECTION $\frac{d\delta}{d|t'|}$ AS A FUNCTION OF $|t'|$ FOR $\pi^+ p \rightarrow \omega \Delta^{++}$.

Dips have been reported in other experiments near $|t|$ (or $|t'|$) values of 0.8, 0.15 and 0.6 $(GeV/c)^2$ at incident momenta between 2.95 and 4.08, 3.7 and 5.0 GeV/c respectively [64,66,68]. But the low point in this experiment near $|t|$ (or $|t'|$) $\approx$ 0.25 $(GeV/c)^2$ may be a statistical fluctuation since this is less than two standard deviations away from the exponential fit. However, another dip near $|t|$ (or $|t'|$) $\sim$ 0.6 $(GeV/c)^2$ is more than two standard deviations away from the exponential fit.

4.4 Determination of the Spin Density Matrix Elements for the ω^o and Δ^{++} Spectra

Before describing the density matrix elements, it is worthwhile to describe the method of moments which was used to calculate these elements from the observed distributions of the polar and azimuthal angles of the decays.

If $f(\cos\theta, \phi)$ is some function of the decay angles, the average value $\overline{f}$ is given by:

$$\overline{f} = \int_0^{2\pi} d\phi \int_{-1}^{+1} d\cos\theta \, f(\cos\theta, \phi) \, W(\cos\theta, \phi), \qquad (4.2)$$

and error on the average value of $\Delta\overline{f}$ is:

$$\Delta\overline{f} = \left[\frac{1}{n} \left(\overline{f^2} - \overline{f}^2 \right) \right]^{\frac{1}{2}}, \qquad (4.3)$$

where n is the number of events used. The relation (4.2) follows because $W(\cos\theta, \phi)$, if normalised, is equivalent to a probability distribution.

By a suitable choice of $f(\cos\theta, \phi)$ and replacing $W(\cos\theta, \phi)$ by equations (2.25), (2.28), (2.31) and (2.34), in turn, in equation (4.2) one may obtain the following relations:

(a) For the ω^o decay in the t- and the s-channel helicity frames:

$$\left.\begin{aligned} \rho_{00} &= \frac{5\langle\cos^2\chi\rangle - 1}{2}, && \text{(a)} \\ \rho_{1-1} &= -\frac{5\langle\sin^2\chi\ \cos 2\psi\rangle}{4}, && \text{(b)} \\ \mathrm{Re}\rho_{10} &= -\frac{5\sqrt{2}\langle\sin 2\chi\ \cos\psi\rangle}{8}. && \text{(c)} \end{aligned}\right\} \quad (4.4)$$

(b) For the ω^o decay in the t- and the s-channel transversity frames:

$$\left.\begin{aligned} \rho_{00} &= \frac{5\langle\cos^2\chi\rangle - 1}{2}, && \text{(a)} \\ \mathrm{Re}\rho_{1-1} &= -\frac{5\langle\sin^2\chi\cos 2\psi\rangle}{4}, && \text{(b)} \\ \mathrm{Im}\rho_{1-1} &= \frac{5\langle\sin^2\chi\sin 2\psi\rangle}{4}. && \text{(c)} \end{aligned}\right\} \quad (4.5)$$

(c) For Δ^{++} decay in the t- and the s-channel helicity frames:

$$\left.\begin{aligned} \rho_{33} &= -\frac{15\langle\cos^2\theta\rangle - 7}{8}, && \text{(a)} \\ \mathrm{Re}\rho_{3-1} &= -\frac{5\sqrt{3}\langle\sin^2\theta\cos 2\phi\rangle}{8}, && \text{(b)} \\ \mathrm{Re}\rho_{31} &= -\frac{5\sqrt{3}\langle\sin 2\theta\ \cos\phi\rangle}{8}. && \text{(c)} \end{aligned}\right\} \quad (4.6)$$

(d) For the Δ^{++} decay in the t- and the s-channel transversity frames:

$$\left.\begin{aligned} (\rho_{33} + \rho_{-3-3}) &= -\frac{15\langle\cos^2\theta\rangle - 7}{4}, && \text{(a)} \\ \mathrm{Re}(\rho_{3-1} + \rho_{-31}) &= -\frac{5\sqrt{3}\langle\sin^2\theta\cos 2\phi\rangle}{4}, && \text{(b)} \\ \mathrm{Im}(\rho_{3-1} - \rho_{-31}) &= \frac{5\sqrt{3}\langle\sin^2\theta\sin 2\phi\rangle}{4}. && \text{(c)} \end{aligned}\right\} \quad (4.7)$$

Using the above formulae the values of the spin density matrix elements for the ω^o and the Δ^{++} separately were determined as functions of $|t|$. Figures (4.5a-h) present the values obtained as functions of $|t|$ in the t- and s-channel helicity frames and t- and s-channel transversity frames respectively. The different frames of reference are the same as already discussed in Section 2.5.

4.5 The Positivity Conditions for the Density Matrix Elements

The properties of the density matrix, in particular its positivity for the diagonal elements, its hermiticity and its unit trace, put certain constraints on its elements. These set of conditions, as derived by Minnaert [77,78] for a completely determined matrix, are reduced to a set of inequalities, if the matrix elements are known through the decay distribution.

If the matrix elements are calculated in any frame with the quantization axis in the production plane (e.g., the t- and the s-channel helicity frames as defined in Section 2.5), the positivity conditions for the ω^o, with spin 1 are:

$$\left.\begin{aligned} 0 \leq \rho_{00} \leq 1 \qquad & \text{(a)} \\ |\mathrm{Re}\rho_{10}| \leq \frac{1}{2}\left[\rho_{00}(1 - \rho_{00} - 2\rho_{1-1})\right]^{\frac{1}{2}} \qquad & \text{(b)} \end{aligned}\right\} \quad (4.8)$$

and for the Δ^{++}, with spin 3/2, these conditions are:

$$\left.\begin{aligned} 0 \leq \rho_{33} \leq 1/2 \qquad & \text{(a)} \\ (\mathrm{Re}\rho_{3,-1})^2 + (\mathrm{Re}\rho_{3,1})^2 + (\rho_{33} - 1/4)^2 \leq 3/16 \qquad & \text{(b)} \end{aligned}\right\} \quad (4.9)$$

Tables (4.3) and (4.4) give the values of these inequalities in the t- and the s-channel helicity frames for the $\omega^o\Delta^{++}$ events for

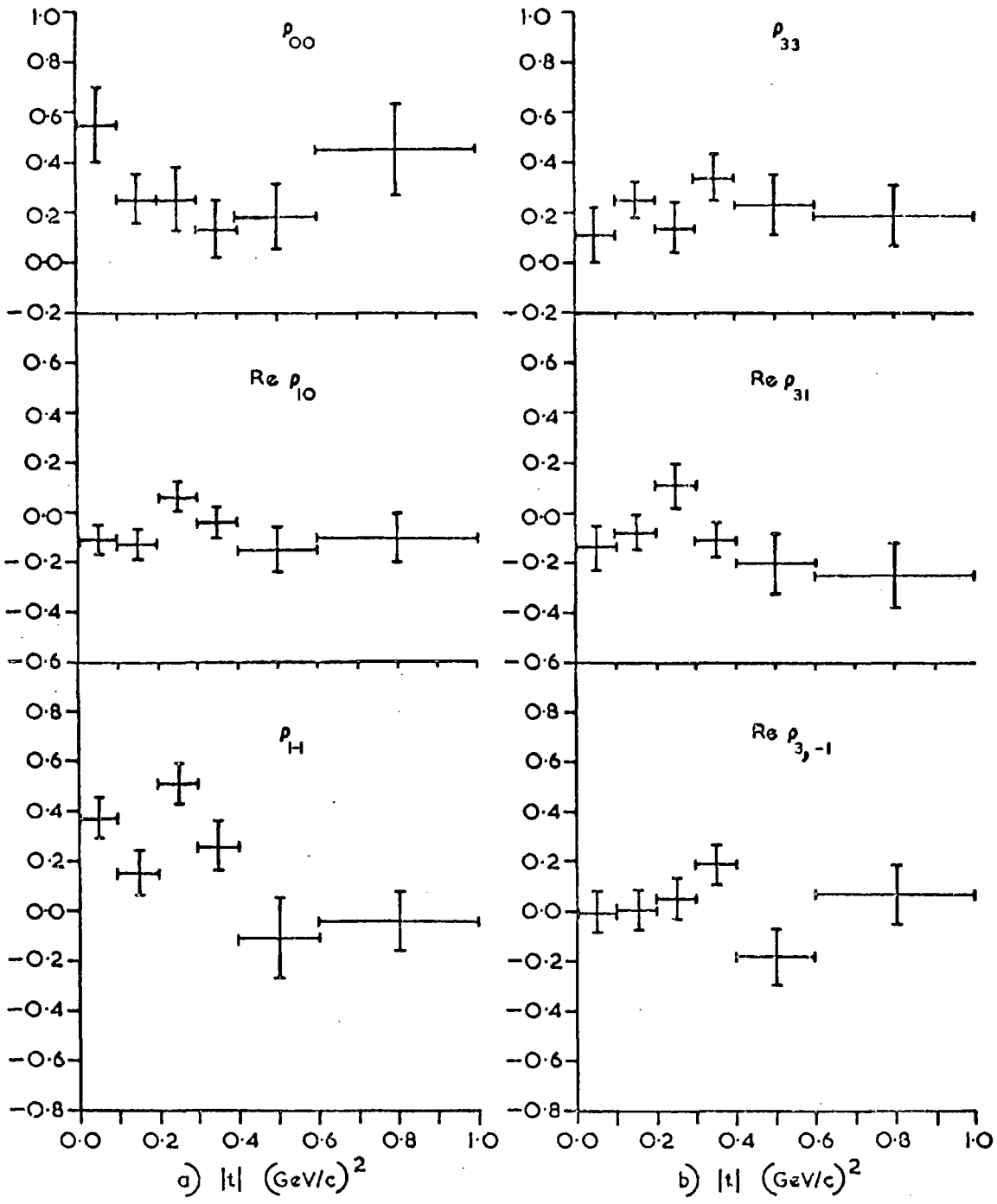

FIG. 4.5 a) SPIN DENSITY MATRIX ELEMENTS FOR THE ω^0 IN THE t-CHANNEL HELICITY FRAME AS FUNCTIONS OF |t|.

b) SPIN DENSITY MATRIX ELEMENTS FOR THE Δ^{++} IN THE t-CHANNEL HELICITY FRAME AS FUNCTIONS OF |t|.

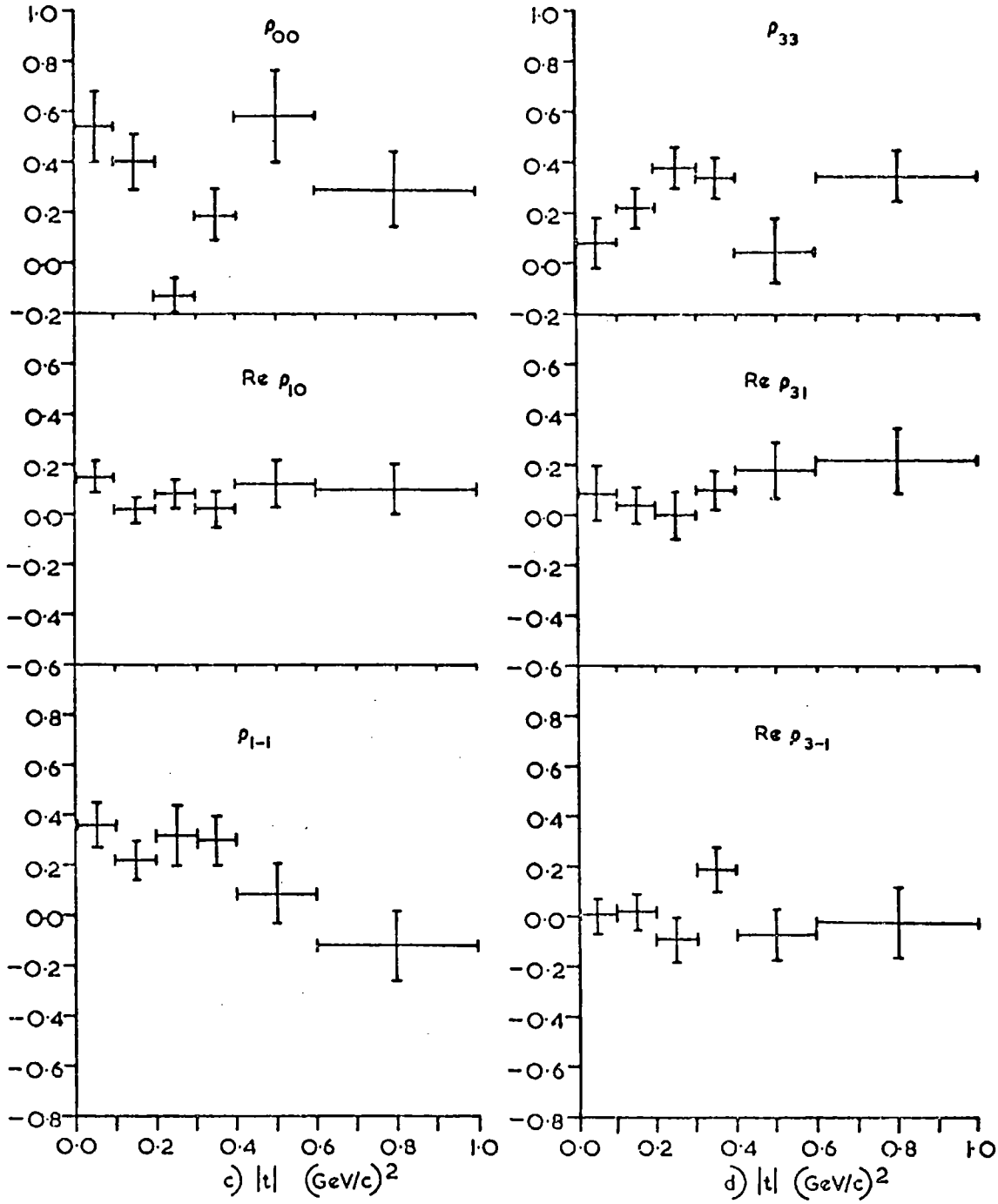

FIG. 4.5 c) SPIN DENSITY MATRIX ELEMENTS FOR THE ω^0 IN THE s-CHANNEL HELICITY FRAME AS FUNCTIONS OF |t|.

d) SPIN DENSITY MATRIX ELEMENTS FOR THE Δ^{++} IN THE s-CHANNEL HELICITY FRAME AS FUNCTIONS OF |t|.

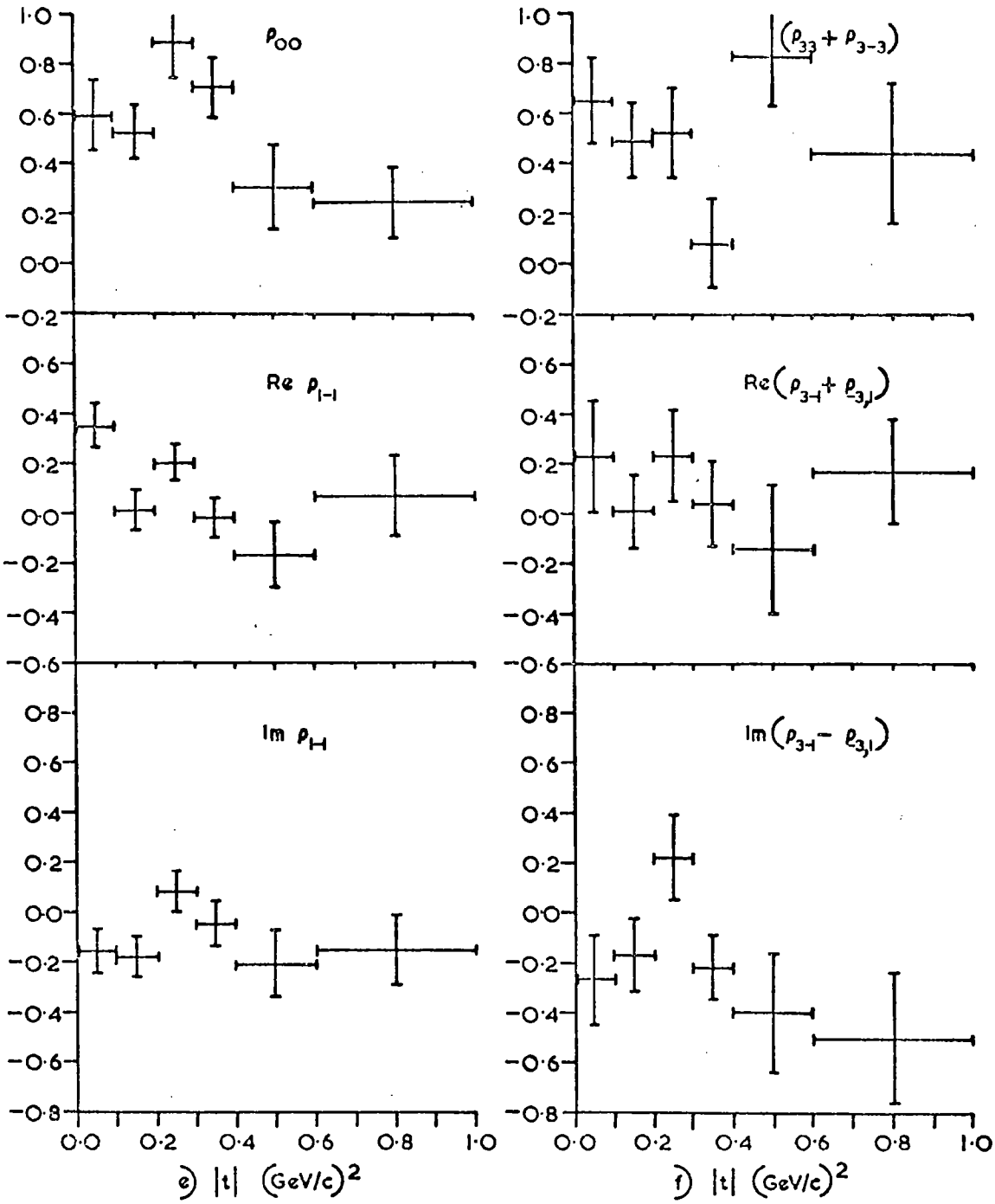

FIG. 4.5 e) SPIN DENSITY MATRIX ELEMENTS FOR THE ω^0 IN THE t-CHANNEL TRANSVERSITY FRAME AS FUNCTIONS OF $|t|$.

f) SPIN DENSITY MATRIX ELEMENTS FOR THE Δ^{++} IN THE t-CHANNEL TRANSVERSITY FRAME AS FUNCTIONS OF $|t|$.

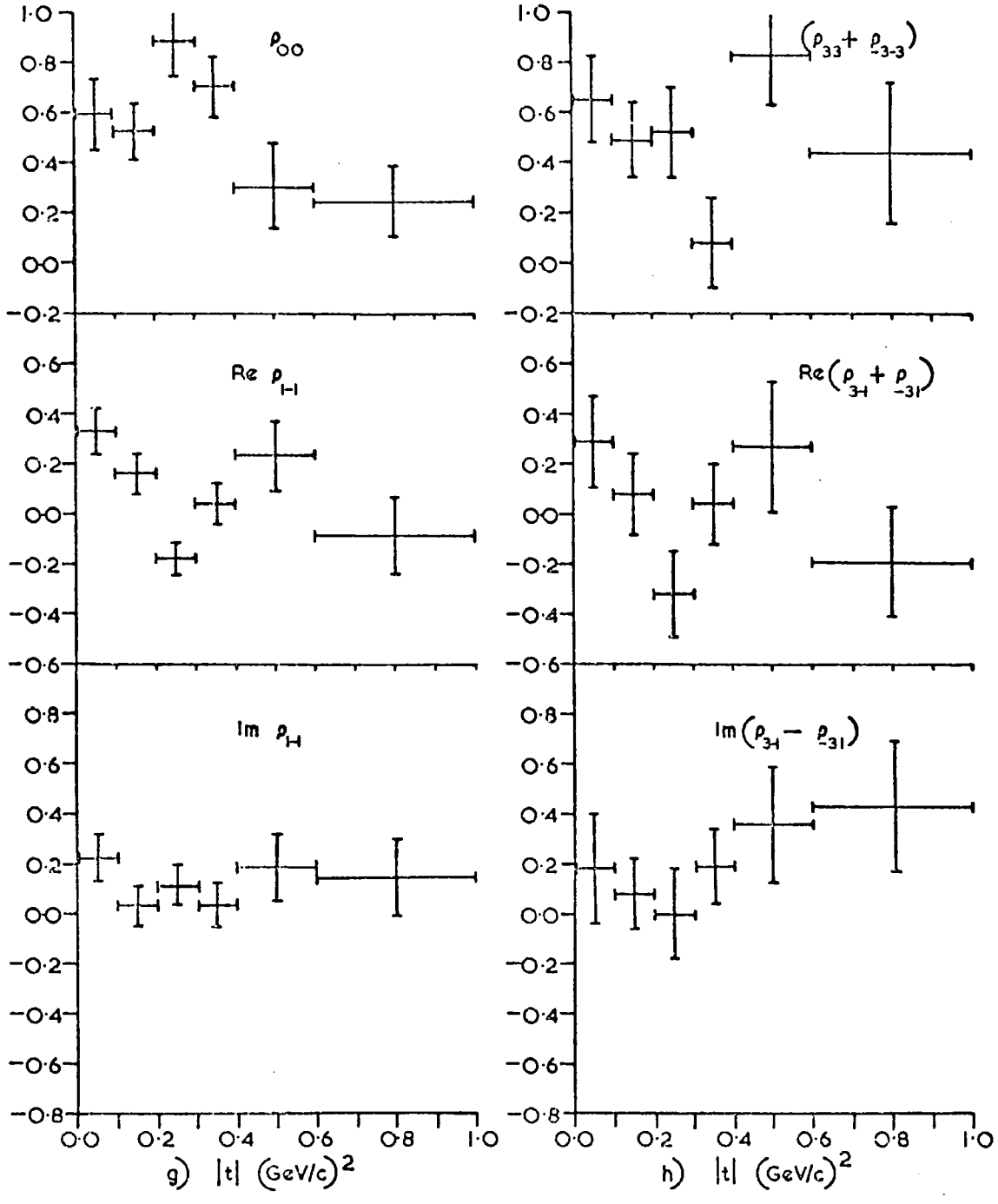

FIG. 4:5 g) SPIN DENSITY MATRIX ELEMENTS FOR THE ω^0 IN THE s-CHANNEL TRANSVERSITY FRAME AS FUNCTIONS OF |t|.

h) SPIN DENSITY MATRIX ELEMENTS FOR THE Δ^{++} IN THE s-CHANNEL TRANSVERSITY FRAME AS FUNCTIONS OF |t|.

different intervals of $|t|$. These are found to be experimentally well satisfied except condition (4.8a) for the $|t|$ interval $0.2 - 0.3\,(GeV/c)^2$ in Table (4.4).

Table (4.3)

Positivity conditions for the density matrix elements in the t-channel helicity (Gottfried-Jackson) frame

Inequality \ $\|t\|$ $(GeV/c)^2$	0.0-0.1	0.1-0.2	0.2-0.3	0.3-0.4	0.4-0.6	0.6-1.0
$0 \leq \rho_{00} \leq 1$	.55±.15	.25±.10	.25±.13	.13±.11	.18±.13	.45±.18
$\|Re\rho_{1,0}\| \leq \frac{1}{2}[\rho_{00}(1-\rho_{00}-2\rho_{1-1})]^{\frac{1}{2}}$	.11±.06 ≤ .20±.06	.13±.06 ≤ .17±.05	.06±.06 ≤ .13±.07	.04±.06 ≤ .11±.10	.15±.09 ≤ .22±.06	.10±.10 ≤ .27±.05
$0 \leq \rho_{33} \leq 1/2$	.11±.11	.25±.07	.14±.10	.34±.09	.23±.12	.19±.12
$(Re\rho_{3-1})^2+(Re\rho_{3\,1})^2 +(\rho_{33}-1/4)^2 \leq 3/16$	.04±.04	.006±.01	.027±.03	.06±.04	.07±.06	.07±.07
No. of events	31	53	40	38	23	19

Table (4.4)

Positivity conditions for the density matrix elements in the s-channel helicity frame.

Inequality \ $\|t\|$ (GeV/c)^2	0.0-0.1	0.1-0.2	0.2-0.3	0.3-0.4	0.4-0.6	0.6-1.0
$0 \leq \rho_{00} \leq 1$	.54±.14	.40±.11	-.13±.07	.19±.10	.58±.18	.29±.15
$\|Re\rho_{1,0}\| \leq \frac{1}{2}[\rho_{00}(1-\rho_{00}-2\rho_{1-1})]^{\frac{1}{2}}$	.15±.06 ≤ .19±.07	.02±.05 ≤ .13±.07	.08±.06 ≤ .13±.09	.02±.07 ≤ .10±.09	.12±.09 ≤ .19±.10	.10±.10 ≤ .26±.05
$0 \leq \rho_{33} \leq 1/2$	.08±.10	.22±.08	.38±.08	.34±.08	.05±.13	.35±.10
$(Re\rho_{3-1})^2+(Re\rho_{3\,1})^2 +(\rho_{33}-1/4)^2 \leq 3/16$	.04±.04	.003±.008	.03±.03	.05±.04	.08±.07	.06±.06
No of events	31	53	40	38	23	19

The value of ρ_{00} in the s-channel helicity frame is negative by two standard deviations for the $|t|$ interval 0.2 - 0.3 (GeV/c)^2. The mass distributions of 3-pion in the various $|t|$ intervals were plotted with a view to finding the reason for the unphysical value of ρ_{00}. The background level in the mass distribution for the $|t|$ interval 0.2 - 0.3 (GeV/c)^2 did not look at all different from others in the different $|t|$ intervals. Similarly, the decay matrix element of the ω^o, λ_ω distribution in this $|t|$ interval did not show any marked difference from those in the other $|t|$ intervals with the statistics of the experiment. It is concluded that the negative value of ρ_{00} is most likely a statistical fluctuation.

4.6 Decay Angular Distributions for the ω^o and Δ^{++} Spectra

Figures (4.6) show the distributions of the ω^o and the Δ^{++} for the decay angles: cosine of polar angle and azimuthal angle for the reaction $\pi^+ p \longrightarrow \omega\Delta^{++}$ in the t- and the s-channel helicity frames and the t- and the s-channel transversity frames. The curves are the fits of the form as obtained from equations (2.26), (2.29), (2.32) and (2.35). The experimental values of the coefficients together with the functions used are tabulated in Table (4.5) on page 61.

4.7 The Natural and the Unnatural Parity Exchange Components

As discussed in Section 2.7.1, the $\omega^o\Delta^{++}$ can be made by exchanging a $\rho(1^-)$ or $B(1^+)$, the former having the natural parity and the latter unnatural. The density matrix element ρ_{oo} in the t-channel helicity frame measures the unnatural parity exchange contribution to the production of the ω^o in the helicity zero state (For the production angle, $\theta^* \longrightarrow 0$ only, i.e., $|t'| \longrightarrow 0$).

The linear combinations

$$\left.\begin{aligned} \sigma_1^+ &= \rho_{11} + \rho_{1-1}\,, && \text{(a)} \\ \sigma_1^- &= \rho_{11} - \rho_{1-1}\,, && \text{(b)} \end{aligned}\right\} \quad (4.10)$$

in the high energy limit (i.e., as $s \longrightarrow \infty$) measure the contributions to the production of the ω^o in the helicity one state for the natural and the unnatural parity exchanges respectively [79]. For the reaction $\pi^+ p \longrightarrow \omega^o\Delta^{++}$, using σ^+ to denote the total natural and σ^- the total unnatural parity exchanges, one gets:

$$\sigma^+ = \sigma_1^+ \quad \text{and} \quad \sigma^- = \sigma_1^- + \rho_{oo}.$$

The distribution of σ_1^+ has the same value for both the t- and the s-channel helicity frames.

Text continued on page 62

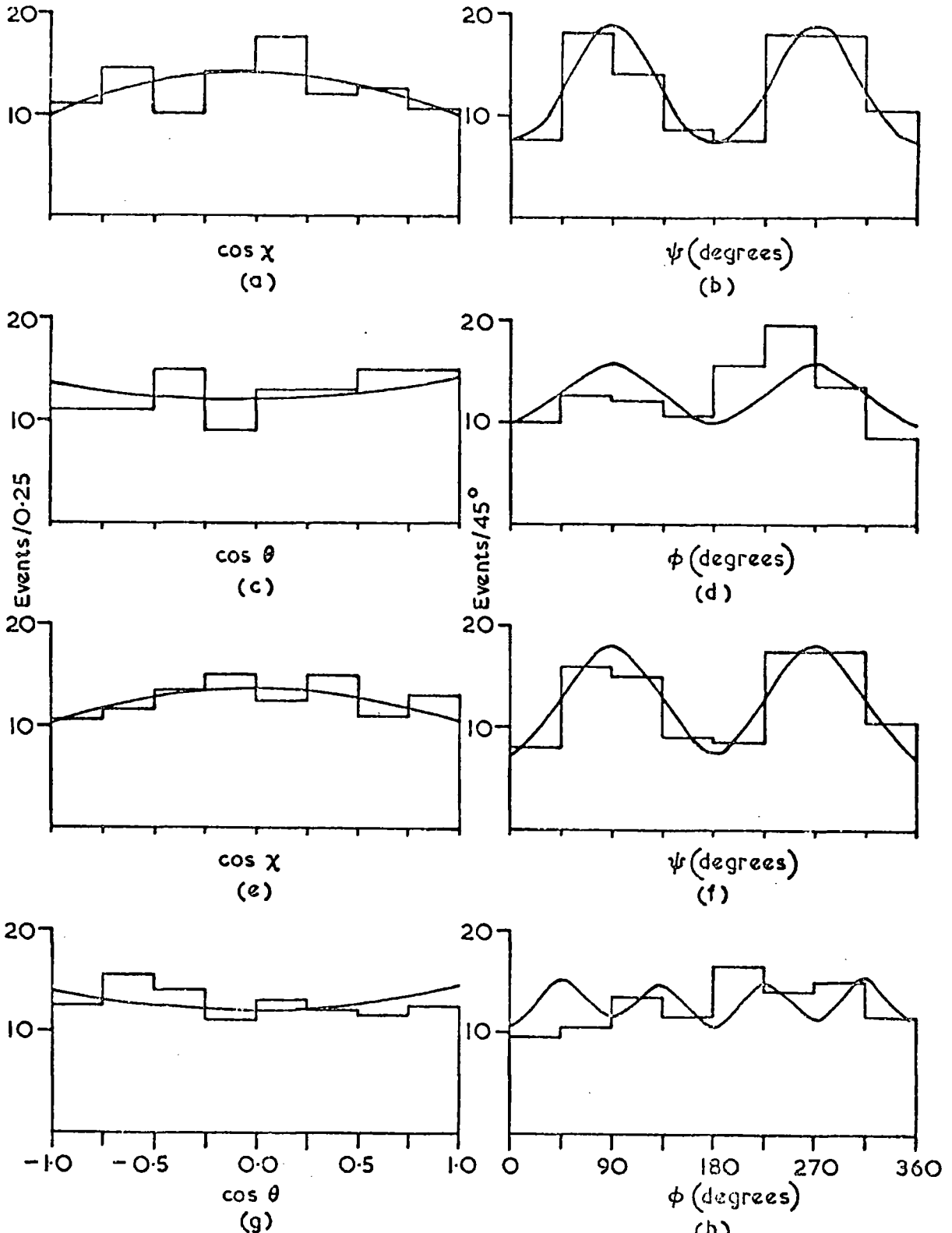

FIG.4.6 (a) DISTRIBUTION OF COSχ FOR THE ω^{o} IN THE t-CHANNEL HELICITY FRAME
(b) DISTRIBUTION OF ψ FOR THE ω^{o} IN THE t-CHANNEL HELICITY FRAME
(c) DISTRIBUTION OF COSθ FOR THE Δ^{++} IN THE t-CHANNEL HELICITY FRAME
(d) DISTRIBUTION OF φ FOR THE Δ^{++} IN THE t-CHANNEL HELICITY FRAME
(e) DISTRIBUTION OF COSχ FOR THE ω^{o} IN THE s-CHANNEL HELICITY FRAME
(f) DISTRIBUTION OF ψ FOR THE ω^{o} IN THE s-CHANNEL HELICITY FRAME
(g) DISTRIBUTION OF COSθ FOR THE Δ^{++} IN THE s-CHANNEL HELICITY FRAME
(h) DISTRIBUTION OF φ FOR THE Δ^{++} IN THE s-CHANNEL HELICITY FRAME

THE CURVES ARE FITS TO THE DATA AS EXPLAINED IN THE TEXT -- 204 events.

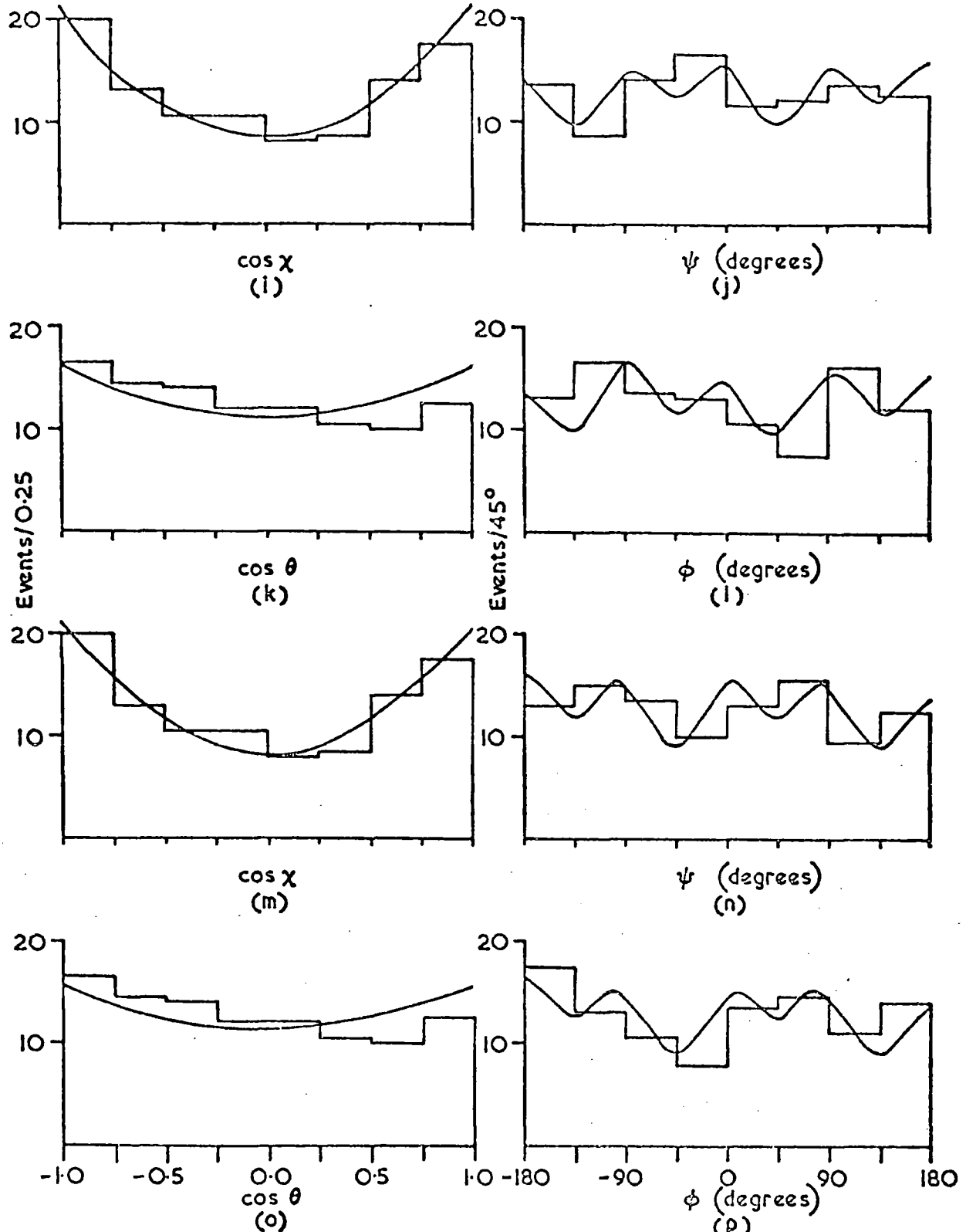

FIG 4.6 (i) DISTRIBUTION OF COSχ FOR THE ω^o IN THE t-CHANNEL TRANSVERSITY FRAME
(j) DISTRIBUTION OF ψ FOR THE ω^o IN THE t-CHANNEL TRANSVERSITY FRAME
(k) DISTRIBUTION OF COSθ FOR THE Δ^{++} IN THE t-CHANNEL TRANSVERSITY FRAME
(l) DISTRIBUTION OF φ FOR THE Δ^{++} IN THE t-CHANNEL TRANSVERSITY FRAME
(m) DISTRIBUTION OF COSχ FOR THE ω^o IN THE s-CHANNEL TRANSVERSITY FRAME
(n) DISTRIBUTION OF ψ FOR THE ω^o IN THE s-CHANNEL TRANSVERSITY FRAME
(o) DISTRIBUTION OF COSθ FOR THE Δ^{++} IN THE s-CHANNEL TRANSVERSITY FRAME
(p) DISTRIBUTION OF φ FOR THE Δ^{++} IN THE s-CHANNEL TRANSVERSITY FRAME

THE CURVES ARE FITS TO THE DATA AS EXPLAINED IN THE TEXT —— 204 events.

Table (4.5)

Parameters of fits to the decay distributions of the ω^o and the Δ^{++} spectra

Frame of Reference	Particle	Fitted Function	Fitted Parameters A	B	C	χ^2/NDF
The t-channel helicity frame (Gottfried-Jackson frame)	ω^o	$A+B\cos^2\chi$	0.55±2.9	-0.16±0.16		4.6/6
		$A+B\cos^2\psi$	0.23±0.07	-0.15±0.04		2.8/6
	Δ^{++}	$A+B\cos^2\theta$	0.72±0.0	0.06±0.49		5.4/6
		$A+B\cos^2\phi$	0.77±0.0	-0.23±0.09		10/6
The s-channel helicity frame (helicity frame)	ω^o	$A+B\cos^2\chi$	0.54±0.8	-0.12		2.0/6
		$A+B\cos^2\psi$	0.22±0.04	-0.13±0.04		1.3/6
	Δ^{++}	$A+B\cos^2\theta$	0.89±0.51	0.11±0.34		2.4/6
		$A+B\cos^2\phi$	0.16±0.11	-0.12±0.03		6/6
The t-channel transversity frame	ω^o	$A+B\cos^2\chi$ †	0.29±0.23	0.46		2.0/6
		$A+B\cos^2\psi + C\sin\psi\cos\psi$	0.68	0.0	-0.21	3.5/5
	Δ^{++}	$A+B\cos^2\theta$ ††	0.35±0.13	0.11±0.15		3.9/6
		$A+B\cos^2\phi + C\sin\phi\cos\phi$	0.24±0.18	-0.04±0.002	-0.04 ±0.02	7.8/5
The s-channel transversity frame	ω^o	$A+B\cos^2\chi$ †	0.29±0.23	0.46		2.0/6
		$A+B\cos^2\psi + C\sin\psi\cos\psi$	0.96±0.15	-0.03±0.06	0.28 ±0.25	2.5/5
	Δ^{++}	$A+B\cos^2\theta$ ††	0.35±0.13	0.11±0.15		3.9/6
		$A+B\cos^2\phi + C\sin\phi\cos\phi$	0.76±0.16	-0.002±0.01	0.30 ±0.26	5.1/5

† These are the same distributions.

†† These are the same distributions.

Table (4.6) gives the values of σ_1^+ and σ_1^- for different intervals of $|t|$ both for the t- and the s-channel helicity frames. Figure (4.7) shows the same values as functions of $|t|$ for six $|t|$ intervals below 1.0 $(GeV/c)^2$.

Table (4.6)

$\sigma_1^+ = \rho_{11}+\rho_{1-1}$ and $\sigma_1^- = \rho_{11}-\rho_{1-1}$ in the t- and the s-channel helicity frames

Quantity	$\|t\|$ $(GeV/c)^2$ / Frame	0.0-0.1	0.1-0.2	0.2-0.3	0.3-0.4	0.4-0.6	0.6-1.0
σ_1^+	The t-channel helicity frame	.59±.11	.52±.10	.88±.10	.70±.11	.30±.16	.24±.15
σ_1^-		-.14±.11	.22±.10	-.14±.10	.18±.11	.52±.16	.32±.15
σ_1^+	The s-channel helicity frame	.59±.11	.52±.10	.88±.10	.70±.11	.30±.16	.24±.15
σ_1^-		-.13±.11	.08±.10	.24±.10	.10±.11	.12±.16	.48±.15
No. of events		31	53	40	38	23	19

Table (4.7) gives the unnatural parity exchange contributions in the helicity zero part of $d\sigma/d|t|$, i.e., $\sigma_o^- = \rho_{00}\, d\sigma/d|t|$, where ρ_{00} is spin density matrix element of the ω^o in the t-channel helicity frame. Figure (4.8) shows the quantity σ_o^- as a function of $|t|$.

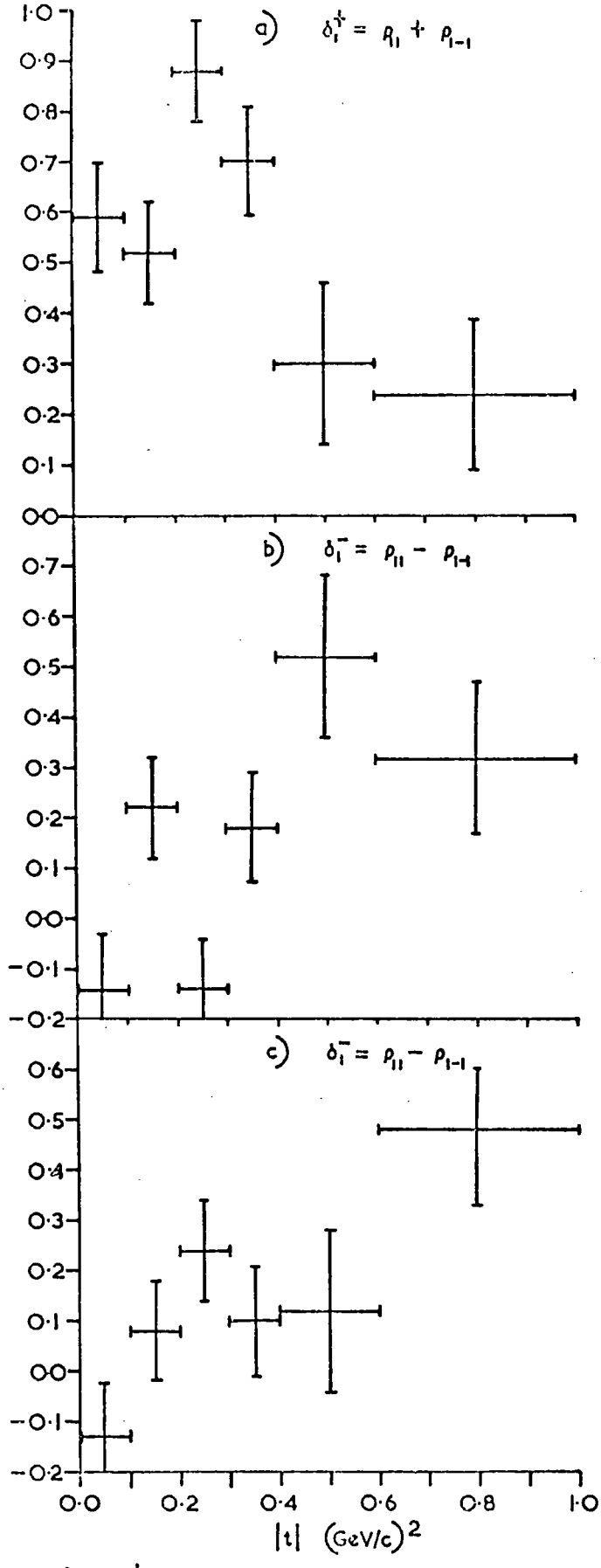

FIG. 4.7

a) δ_1^+ IN THE t-OR s-CHANNEL HELICITY FRAME AS A FUNCTION OF $|t|$.

b) δ_1^- IN THE t-CHANNEL HELICITY FRAME AS A FUNCTION OF $|t|$.

c) δ_1^- IN THE s-CHANNEL HELICITY FRAME AS A FUNCTION OF $|t|$.

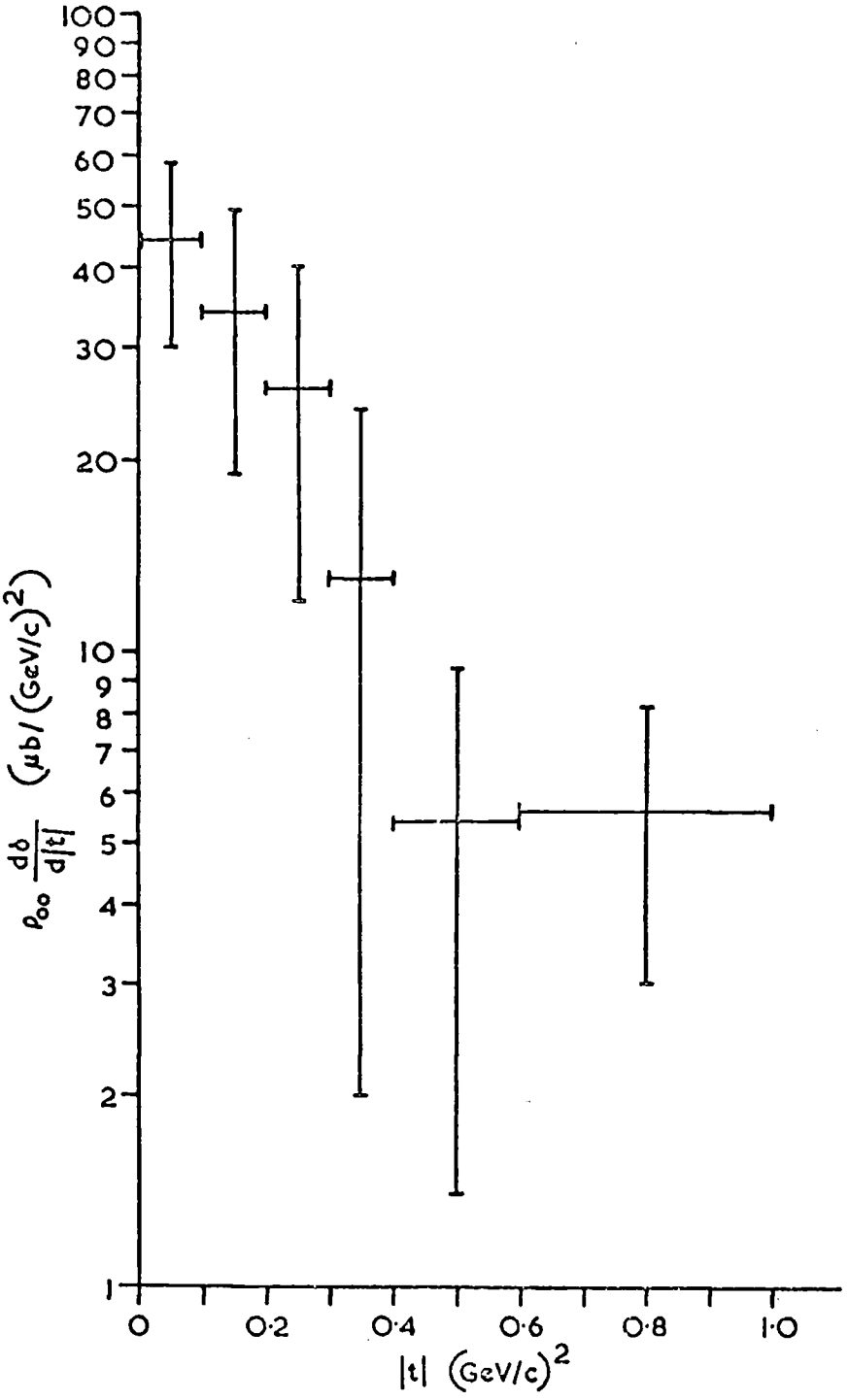

FIG. 4.8 THE UNNATURAL PART OF DIFFERENTIAL CROSS-SECTION, $\rho_{00}\frac{d\delta}{d|t|}$, FOR HELICITY ZERO IN THE t-CHANNEL HELICITY FRAME AS A FUNCTION OF $|t|$.

Table (4.7)

Unnatural part of the differential cross-section, $\rho_{00}\, d\sigma/d|t|$ for helicity zero in the t-channel helicity frame.

$\|t\|$ Interval $[(GeV/c)^2]$	$d\sigma/d\|t\|$ $(\omega\Delta^{++})$ $[\mu b/(GeV/c)^2]$	$\rho_{00}\, d\sigma/d\|t\|$ $(\omega\Delta^{++})$ $[\mu b/(GeV/c)^2]$
0.0 - 0.1	81 ± 14	44 ± 14
0.1 - 0.2	138 ± 19	34 ± 15
0.2 - 0.3	104 ± 16	26 ± 14
0.3 - 0.4	99 ± 16	13 ± 11
0.4 - 0.6	30 ± 6.2	5.4 ± 4
0.6 - 1.0	12 ± 2.8	5.6 ± 2.6

4.8 The Joint Decay Correlations

It was shown in Section 4.4 how the decay angular distributions of the ω^o and the Δ^{++} are used to determine their spin density matrix elements separately. When the double resonance production occurs, as in the reaction (4.1), it is possible to define a joint spin density matrix which determines the combined decay distribution, $W(\cos\chi, \psi\,;\ \cos\theta, \phi)$, where the decay angles are defined in the respective frames of the ω^o and the Δ^{++}.

Using helicity formalism [80], the production amplitudes for the reaction (4.1) may be written as:

$$\langle \lambda_{\omega^o} \lambda_{\Delta^{++}} \mid T(x) \mid \lambda_{\pi^+} \lambda_p \rangle \ , \qquad (4.11)$$

where x is the cosine of the C.M. production angle, and λ_i is the

helicity of particle i.

Defining m and n as the projections of spin of the ω^o and the Δ^{++} along their respective quantisation axes, the joint spin density matrix is a matrix of 144 complex elements as defined by the following relation:

$$\rho^{mm'}_{nn'} = \sum_{\lambda_\pi + \lambda_p} < mn | T(x) | \lambda_{\pi^+}\lambda_p > < m'n' | T(x) | \lambda_{\pi^+}\lambda_p >^* . \qquad (4.12)$$

The combined decay angular distributions of the ω^o and the Δ^{++} thus determine 19 independent parameters, six of which are determined by the individual decays. To calculate the remaining 13 parameters, it is necessary to consider the correlations between the decays. Pilkuhn and Svensson [34] gave an expression for the joint decay in both the t- and the s-channel helicity frames. The extra 13 correlations should all be zero, if there are no correlations.

An alternative method is to use the joint decay distributions for the decay of two resonances (spins s_1 and s_2) in terms of the joint decay statistical tensors, $T^{J_1J_2}_{M_1M_2}$, produced in a collision of unpolarized particles, as given by Kotanski et al. [81,82].

$$W(\cos\chi, \psi; \cos\theta, \phi) = \sum_{J_1M_1} \sum_{J_2M_2} F_1(J_1)\, F_2(J_2) \cdot T^{J_1J_2}_{M_1M_2}\, Y^{M_1}_{J_1}(\chi,\psi)^*\, Y^{M_2}_{J_2}(\theta,\phi)^* , \qquad (4.13)$$

where index 1(2) stands for $\omega(\Delta^{++})$ vertex; F_i are known constants and $J_i \leq 2s_i$. The angles χ, ψ, θ and ϕ specify the direction of the decay products of the ω^o and the Δ^{++} in their respective rest frames. Equation (4.13) then reduces to 19 real parameters in the t- and the s-channel helicity frames as given below (see Appendix B for derivation).

$$W(\cos\chi,\psi;\cos\theta,\phi) = \frac{1}{16\pi^2}\Big[1 - \sqrt{3}\,T_{00}^{02}(3\cos^2\theta-1) + 3\sqrt{2}\,T_{01}^{02}\sin2\theta\cos\phi$$

$$- 3\sqrt{2}\,T_{02}^{02}\sin^2\theta\cos2\phi - \sqrt{6}\,T_{00}^{20}\,(3\cos^2\chi-1)$$

$$+ \quad 6\,T_{10}^{20}\sin2\chi\cos\psi - 6T_{20}^{20}\sin^2\chi\cos2\psi$$

$$+ (\sqrt{6}/2)T_{00}^{22}(3\cos^2\chi-1)(3\cos^2\theta-1)$$

$$- \quad 3\,T_{01}^{22}(3\cos^2\chi-1)\ \sin2\theta\cos\phi$$

$$+ \quad 3\,T_{02}^{22}(3\cos^2\chi-1)\ \sin^2\theta\cos2\phi$$

$$+(3\sqrt{6}/2)T_{1-2}^{22}\ \sin2\chi\sin^2\theta\cos(\psi-2\phi)$$

$$-(3\sqrt{6}/2)T_{1-1}^{22}\sin2\chi\ \sin2\theta\cos(\psi-\phi)$$

$$- \quad 3\,T_{10}^{22}\ \sin2\chi\cos\psi\ (3\cos^2\theta-1)$$

$$+(3\sqrt{6}/2)T_{11}^{22}\ \sin2\chi\sin2\theta\cos(\psi+\phi)$$

$$-(3\sqrt{6}/2)T_{12}^{22}\ \sin2\chi\sin^2\theta\cos(\psi+2\phi) \qquad (4.14)$$

$$-(3\sqrt{6}/2)T_{2-2}^{22}\sin^2\chi\sin^2\theta\cos(2\psi-2\phi)$$

$$+(3\sqrt{6}/2)T_{2-1}^{22}\sin^2\chi\sin2\theta\cos(2\psi-\phi)$$

$$+ \quad 3\,T_{20}^{22}\ \sin^2\chi\cos2\psi\ (3\cos^2\theta-1)$$

$$-(3\sqrt{6}/2)T_{21}^{22}\ \sin^2\chi\ \sin2\theta\ \cos(2\psi+\phi)$$

$$+(3\sqrt{6}/2)T_{22}^{22}\ \sin^2\chi\ \sin^2\theta\ \cos2(\psi+\phi)\Big].$$

In the t- and the s-channel transversity frames, there are three real parameters and eight complex parameters as given below (see Appendix B for derivation).

$$
\begin{aligned}
W(\cos\chi,\psi;\cos\theta,\phi) = \frac{1}{16\pi^2}\Big[1 &- \sqrt{3}\; T_{00}^{02}(3\cos^2\theta-1) - \sqrt{6}\; T_{00}^{20}(3\cos^2\chi-1) \\
&+ (\sqrt{6}/2)\; T_{00}^{22}(3\cos^2\chi-1)(3\cos^2\theta-1) \\
&- 3\sqrt{2}\; \mathrm{Re}\, T_{02}^{02}\sin^2\theta\cos 2\phi \\
&- 3\sqrt{2}\; \mathrm{Im}\, T_{02}^{02}\sin^2\theta\sin 2\phi \\
&+ 3\; \mathrm{Re}\, T_{02}^{22}(3\cos^2\chi-1)\sin^2\theta\cos 2\phi \\
&+ 3\; \mathrm{Im}\, T_{02}^{22}(3\cos^2\chi-1)\sin^2\theta\sin 2\phi \\
&- (3\sqrt{6}/2)\; \mathrm{Re}\, T_{1-1}^{22}\sin 2\chi\sin 2\theta\cos(\psi-\phi) \\
&- (3\sqrt{6}/2)\; \mathrm{Im}\, T_{1-1}^{22}\sin 2\chi\sin 2\theta\sin(\psi-\phi) \\
&+ (3\sqrt{6}/2)\; \mathrm{Re}\, T_{11}^{22}\sin 2\chi\sin 2\theta\cos(\psi+\phi) \\
&+ (3\sqrt{6}/2)\; \mathrm{Im}\, T_{11}^{22}\sin 2\chi\sin 2\theta\sin(\psi+\phi) \\
&- 6\; \mathrm{Re}\, T_{20}^{20}\sin^2\chi\cos 2\psi \\
&- 6\; \mathrm{Im}\, T_{20}^{20}\sin^2\chi\sin 2\psi \\
&- (3\sqrt{6}/2)\; \mathrm{Re}\, T_{2-2}^{22}\sin^2\chi\sin^2\theta\cos 2(\psi-\phi) \\
&- (3\sqrt{6}/2)\; \mathrm{Im}\, T_{2-2}^{22}\sin^2\chi\sin^2\theta\sin 2(\psi-\phi) \\
&+ 3\; \mathrm{Re}\, T_{20}^{22}\sin^2\chi\cos 2\psi(3\cos^2\theta-1) \\
&+ 3\; \mathrm{Im}\, T_{20}^{22}\sin^2\chi\sin 2\psi(3\cos^2\theta-1) \\
&+ (3\sqrt{6}/2)\; \mathrm{Re}\, T_{22}^{22}\sin^2\chi\sin^2\theta\cos 2(\psi+\phi) \\
&+ (3\sqrt{6}/2)\; \mathrm{Im}\, T_{22}^{22}\sin^2\chi\sin^2\theta\sin 2(\psi+\phi)\Big].
\end{aligned}
\tag{4.15}
$$

By a suitable choice of $f(\cos\chi,\psi;\cos\theta,\phi)$ and replacing $W(\cos\chi,\psi;\cos\theta,\phi)$ by equations (4.14) and (4.15), in turn, in equation (4.2), one may obtain the relations as listed in Tables (4.8) and (4.9) respectively for the t- or the s-channel helicity frame and the t- or the s-channel transversity frame on pages 68-69.

The values of the joint statistical tensors as determined by using the formulae listed in Tables (4.8) and (4.9) in the t- and the s-channel helicity frames and in the t- and the s-channel transversity frames for four different intervals of $|t|$ below 1.0 $(GeV/c)^2$ show that most of these values are small with large errors and thus are compatible with zero. However, the following significant correlation terms (significant here means two or more than 2 standard deviations different from zero) are listed in Table (4.10) on page 70.

4.9 The Donohue Inequalities

Donohue [83] analysed the joint decay correlations in the t- and the s-channel helicity frames in the forward production direction using the kinematic constraints and showed that only terms depending on χ,θ (the polar angles of the ω^o and the Δ^{++} respectively) and $(\psi+\phi)$ (sum of azimuthal angles of the ω and the Δ^{++}) need not vanish. These correspond to the first (T_{00}^{02}), fourth (T_{00}^{20}), seventh (T_{00}^{22}), thirteenth (T_{11}^{22}) and nineteenth (T_{22}^{22}) terms in Table (4.8). All these values are compatible with zero in the t-channel helicity frame. But T_{00}^{02}, T_{00}^{20} and T_{00}^{22} have significant values in the s-channel helicity frame for the $|t|$ intervals 0.2-0.4, 0.2-0.4 and 0.0-0.2 $(GeV/c)^2$ respectively as listed in Table (4.10).

Donohue [83] derives two inequalities which should be satisfied in the forward direction for the joint decay correlations in the t- and the s-channel helicity frames. These are:

Text continued on page 71

Table (4.8)

Joint decay statistical tensors in the t- or s-channel helicity frame for $\pi^+ p \longrightarrow \omega\Delta^{++}$ †

Tensor	Value in terms of spherical harmonics	Value in terms of decay angles
T^{02}_{00}	$-\pi\sqrt{20/3}\ \langle Y^0_0(1)Y^0_2(2)\rangle$	$-\frac{5\sqrt{3}}{12}\langle 3\cos^2\theta-1\rangle$
T^{02}_{01}	$-\pi\sqrt{20/3}\ \langle Y^0_0(1)Y^1_2(2)\rangle$	$\frac{5\sqrt{2}}{8}\langle \sin 2\theta\cos\phi\rangle$
T^{02}_{02}	$-\pi\sqrt{20/3}\ \langle Y^0_0(1)Y^2_2(2)\rangle$	$-\frac{5\sqrt{2}}{8}\langle \sin^2\theta\cos 2\phi\rangle$
T^{20}_{00}	$-\pi\sqrt{10/3}\ \langle Y^0_2(1)Y^0_0(2)\rangle$	$-\frac{5\sqrt{6}}{24}\langle 3\cos^2\chi-1\rangle$
T^{20}_{10}	$-\pi\sqrt{10/3}\ \langle Y^1_2(1)Y^0_0(2)\rangle$	$\frac{5}{8}\langle \sin 2\chi\cos\psi\rangle$
T^{20}_{20}	$-\pi\sqrt{10/3}\ \langle Y^2_2(1)Y^0_0(2)\rangle$	$-\frac{5}{8}\langle \sin^2\chi\cos 2\psi\rangle$
T^{22}_{00}	$\pi\sqrt{50/3}\ \langle Y^0_2(1)Y^0_2(2)\rangle$	$\frac{25\sqrt{6}}{48}\langle (3\cos^2\chi-1)(3\cos^2\theta-1)\rangle$
T^{22}_{01}	$\pi\sqrt{50/3}\ \langle Y^0_2(1)Y^1_2(2)\rangle$	$-\frac{25}{16}\langle (3\cos^2\chi-1)(\sin 2\theta\cos\phi)\rangle$
T^{22}_{02}	$\pi\sqrt{50/3}\ \langle Y^0_2(1)Y^2_2(2)\rangle$	$\frac{25}{16}\langle (3\cos^2\chi-1)(\sin^2\theta\cos 2\phi)\rangle$
T^{22}_{1-2}	$\pi\sqrt{50/3}\ \langle Y^1_2(1)Y^{-2}_2(2)\rangle$	$\frac{25\sqrt{6}}{32}\langle \sin 2\chi\sin^2\theta\cos(\psi-2\phi)\rangle$
T^{22}_{1-1}	$\pi\sqrt{50/3}\ \langle Y^1_2(1)Y^{-1}_2(2)\rangle$	$-\frac{25\sqrt{6}}{32}\langle \sin 2\chi\sin 2\theta\cos(\psi-\phi)\rangle$
T^{22}_{10}	$\pi\sqrt{50/3}\ \langle Y^1_2(1)Y^0_2(2)\rangle$	$-\frac{25}{16}\langle \sin 2\chi\cos\psi(3\cos^2\theta-1)\rangle$
T^{22}_{11}	$\pi\sqrt{50/3}\ \langle Y^1_2(1)Y^1_2(2)\rangle$	$\frac{25\sqrt{6}}{32}\langle \sin 2\chi\sin 2\theta\cos(\psi+\phi)\rangle$
T^{22}_{12}	$\pi\sqrt{50/3}\ \langle Y^1_2(1)Y^2_2(2)\rangle$	$-\frac{25\sqrt{6}}{32}\langle \sin 2\chi\sin^2\theta\cos(\psi+2\phi)\rangle$
T^{22}_{2-2}	$\pi\sqrt{50/3}\ \langle Y^2_2(1)Y^{-2}_2(2)\rangle$	$-\frac{25\sqrt{6}}{32}\langle \sin^2\chi\sin^2\theta\cos(2\psi-2\phi)\rangle$
T^{22}_{2-1}	$\pi\sqrt{50/3}\ \langle Y^2_2(1)Y^{-1}_2(2)\rangle$	$\frac{25\sqrt{6}}{32}\langle \sin^2\chi\sin 2\theta\cos(2\psi-\phi)\rangle$
T^{22}_{20}	$\pi\sqrt{50/3}\ \langle Y^2_2(1)Y^0_2(2)\rangle$	$\frac{25}{16}\langle \sin^2\chi\cos 2\psi(3\cos^2\theta-1)\rangle$
T^{22}_{21}	$\pi\sqrt{50/3}\ \langle Y^2_2(1)Y^1_2(2)\rangle$	$-\frac{25\sqrt{6}}{32}\langle \sin^2\chi\sin 2\theta\cos(2\psi+\phi)\rangle$
T^{22}_{22}	$\pi\sqrt{50/3}\ \langle Y^2_2(1)Y^2_2(2)\rangle$	$\frac{25\sqrt{6}}{32}\langle \sin^2\chi\sin^2\theta\cos(2\psi+2\phi)\rangle$

† $Y^M_J(1)$ and $Y^M_J(2)$ stand for $Y^M_J(\omega^o)$ and $Y^M_J(\Delta^{++})$ respectively.

χ and ψ are the polar and azimuthal angles for the ω^o.

θ and ϕ are the polar and azimuthal angles for the Δ^{++}.

Table (4.9)

Joint decay statistical tensors in the t- or s-channel transversity frame for $\pi^+ p \longrightarrow \omega\Delta^{++}$ †

Tensor	Value in terms of spherical harmonics	Value in terms of decay angles
T^{02}_{00}	$-\pi\sqrt{20/3} < Y^0_0(1)Y^0_2(2)>$	$-\frac{5\sqrt{3}}{12}<3\cos^2\theta -1>$
T^{20}_{00}	$-\pi\sqrt{10/3} < Y^0_2(1)Y^0_0(2)>$	$-\frac{5\sqrt{6}}{24}<3\cos^2\chi -1>$
T^{22}_{00}	$\pi\sqrt{50/3} < Y^0_2(1)Y^0_2(2)>$	$\frac{25\sqrt{6}}{48}<(3\cos^2\chi-1)(3\cos^2\theta -1)>$
Re T^{02}_{02}	$\mathrm{Re}(-\pi\sqrt{20/3} < Y^0_0(1)Y^2_2(2)>)$	$-\frac{5\sqrt{2}}{8}<\sin^2\theta\ \cos2\phi>$
Im T^{02}_{02}	$\mathrm{Im}(-\pi\sqrt{20/3} < Y^0_0(1)Y^2_2(2)>)$	$-\frac{5\sqrt{2}}{8}<\sin^2\theta\sin 2\phi>$
Re T^{22}_{02}	$\mathrm{Re}(\pi\sqrt{50/3} < Y^0_2(1)Y^2_2(2)>)$	$\frac{25}{16}<(3\cos^2\chi-1)\ \sin^2\theta\cos2\phi>$
Im T^{22}_{02}	$\mathrm{Im}(\pi\sqrt{50/3} < Y^0_2(1)Y^2_2(2)>)$	$\frac{25}{16}<(3\cos^2\chi-1)\sin^2\theta\sin2\phi>$
Re T^{22}_{1-1}	$\mathrm{Re}(\pi\sqrt{50/3} < Y^1_2(1)Y^{-1}_2(2)>)$	$-\frac{25\sqrt{6}}{32}<\sin2\chi\ \sin2\theta\ \cos(\psi-\phi)>$
Im T^{22}_{1-1}	$\mathrm{Im}(\pi\sqrt{50/3} < Y^1_2(1)Y^{-1}_2(2)>)$	$-\frac{25\sqrt{6}}{32}<\sin2\chi\ \sin2\theta\ \sin(\psi-\phi)>$
Re T^{22}_{11}	$\mathrm{Re}(\pi\sqrt{50/3} < Y^1_2(1)Y^1_2(2)>)$	$\frac{25\sqrt{6}}{32}<\sin2\chi\ \sin2\theta\ \cos(\psi+\phi)>$
Im T^{22}_{11}	$\mathrm{Im}(\pi\sqrt{50/3} < Y^1_2(1)Y^1_2(2)>)$	$\frac{25\sqrt{6}}{32}<\sin2\chi\ \sin2\theta\ \sin(\psi+\phi)>$
Re T^{20}_{20}	$\mathrm{Re}(-\pi\sqrt{10/3} < Y^2_2(1)Y^0_0(2)>)$	$-\frac{5}{8}\ <\sin^2\chi\ \cos2\psi>$
Im T^{20}_{20}	$\mathrm{Im}(-\pi\sqrt{10/3} < Y^2_2(1)Y^0_0(2)>)$	$-\frac{5}{8}\ <\sin^2\chi\ \sin2\psi>$
Re T^{22}_{2-2}	$\mathrm{Re}(\pi\sqrt{50/3} < Y^2_2(1)Y^{-2}_2(2)>)$	$-\frac{25\sqrt{6}}{32}<\sin^2\chi\ \sin^2\theta\ \cos(2\psi-2\phi)>$
Im T^{22}_{2-2}	$\mathrm{Im}(\pi\sqrt{50/3} < Y^2_2(1)Y^{-2}_2(2)>)$	$-\frac{25\sqrt{6}}{32}<\sin^2\chi\ \sin^2\theta\ \sin(2\psi-2\phi)>$
Re T^{22}_{20}	$\mathrm{Re}(\pi\sqrt{50/3} < Y^2_2(1)Y^0_2(2)>)$	$\frac{25}{16}\ <\sin^2\chi\ \cos2\psi\ (3\cos^2\theta-1)>$
Im T^{22}_{20}	$\mathrm{Im}(\pi\sqrt{50/3} < Y^2_2(1)Y^0_2(2)>)$	$\frac{25}{16}\ <\sin^2\chi\ \sin2\psi\ (3\cos^2\theta-1)>$
Re T^{22}_{22}	$\mathrm{Re}(\pi\sqrt{50/3} < Y^2_2(1)Y^2_2(2)>)$	$\frac{25\sqrt{6}}{32}<\sin^2\chi\ \sin^2\theta\ \cos(2\psi+2\phi)>$
Im T^{22}_{22}	$\mathrm{Im}(\pi\sqrt{50/3} < Y^2_2(1)Y^2_2(2)>)$	$\frac{25\sqrt{6}}{32}<\sin^2\chi\ \sin^2\theta\ \sin(2\psi+2\phi)>$

† $Y^M_J(1)$ and $Y^M_J(2)$ stand for $Y^M_J(\omega^o)$ and $Y^M_J(\Delta^{++})$ respectively.

χ and ψ are the polar and azimuthal angles for the ω^o.

θ and ϕ are the polar and azimuthal angles for the Δ^{++}.

Table (4.10)

Joint decay statistical tensor values for the $\omega\Delta^{++}$ for $|t| < 1.0$ $(GeV/c)^2$

Frame of reference	$\|t\|$ $(GeV/c)^2$ / Tensor	0.0-0.2	0.2-0.4	0.4-0.6
The t-channel helicity frame	T^{02}_{02}	-	0.10±0.05	-
	T^{20}_{10}	0.09±0.03	-	-
	T^{20}_{20}	0.11±0.03	0.19±0.03	-
	T^{22}_{01}	-0.16±0.08	-	-
The s-channel helicity frame	T^{02}_{00}	-	0.13±0.06	-
	T^{20}_{00}	-	0.19±0.04	-
	T^{20}_{20}	0.14±0.03	0.15±0.04	-
	T^{22}_{00}	0.27±0.13	-	-
	T^{22}_{01}	-	-	-0.32±0.15
	T^{22}_{10}	0.16±0.07	-	-
	T^{22}_{20}	-	-	0.36±0.14
The t-channel transversity frame	T^{20}_{00}	0.13±0.05	0.28±0.06	-
	T^{22}_{00}	-	0.33±0.14	-
	Re T^{20}_{20}	0.07±0.03	-	-
	Im T^{20}_{20}	0.09±0.03	-	-
	Im T^{22}_{2-2}	0.14±0.07	-	-
	Im T^{22}_{22}	-	-	0.35±0.14
The s-channel transversity frame	T^{20}_{00}	0.13±0.05	0.28±0.06	-
	T^{22}_{00}	-	0.33±0.14	-
	Re T^{20}_{20}	0.11±0.03	-0.04±0.02	-
	Re T^{22}_{22}	0.15±0.07	-	-
	Im T^{22}_{22}	-	-	0.36±0.14
No. of events		84	78	23

$$\left.\begin{aligned} |T_{11}^{22}| &\leq \left(\frac{1}{2}\rho_{00}\rho_{33}\right)^{\frac{1}{2}} && \text{(a)} \\ |T_{22}^{22}| &\leq \left(\rho_{33}\,(1-\rho_{00}-2\rho_{33})\right)^{\frac{1}{2}} && \text{(b)} \end{aligned}\right\} \quad (4.16)$$

Tables (4.11) and (4.12) give the values of these inequalities in the t- and the s-channel helicity frames for the $\omega\Delta^{++}$ events for different intervals of $|t|$. They are found to be experimentally satisfied except inequality (4.16(a)) for $|t|$ interval $0.2 - 0.3\ (\text{GeV/c})^2$ in both the t- and the s-channel helicity frames where ρ_{00} has a negative value in the s-channel helicity frame, as already discussed in Section 4.5. However, condition (4.16(b)) — which should be satisfied only at low value of $|t|$ — is not satisfied in the s-channel helicity frame for $|t|$ interval of $0.6 - 1.0\ (\text{GeV/c})^2$ (see page 72 for Tables (4.11)-(4.12)).

4.10 The Moduli of the Transversity Tensors

Martin [84] shows that the moduli of the transversity tensors are frame invariant. Inspection of Table (4.9) shows that the three real tensors are invariant in both the t- and the s-channel transversity frames. The moduli of the complex parameters are:

$$\left(\text{Re}\ T^{J_1J_2}_{M_1M_2}\right)^2 + \left(\text{Im}\ T^{J_1J_2}_{M_1M_2}\right)^2 = \text{Frame invariant.}$$

The values of Table (4.13) show that these moduli are invariant in both the t- and the s-channel transversity frames within the statistical errors as listed on page 73.

Table (4.11)

The Donohue inequalities in the t-channel helicity frame

$\lvert t\rvert$ (GeV/c)^2 / Inequality	0.0-0.1	0.1-0.2	0.2-0.3	0.3-0.4	0.4-0.6	0.6-1.0
$\lvert T_{11}^{22}\rvert \leqslant (\frac{1}{2}\rho_{00}\rho_{33})^{\frac{1}{2}}$	.11±.15 ⩽ .17±.09	.17±.10 ⩽ .18±.04	.14±.10 ⩽ .13±.06	.09±.10 ⩽ .15±.06	.05±.16 ⩽ .14±.06	.15±.16 ⩽ .21±.08
$\lvert T_{22}^{22}\rvert \leqslant (\rho_{33}(1-\rho_{00}-2\rho_{33}))^{\frac{1}{2}}$	.07±.11 ⩽ .16±.05	.13±.10 ⩽ .25±.06	.12±.12 ⩽ .26±.05	.20±.13 ⩽ .25±.11	.25±.14 ⩽ .29±.06	.03±.16 ⩽ .18±.12
No of events	31	53	40	38	23	19

Table (4.12)

The Donohue inequalities in the s-channel helicity frame

$\lvert t\rvert$ (GeV/c)^2 / Inequality	0.0-0.1	0.1-0.2	0.2-0.3	0.3-0.4	0.4-0.6	0.6-1.0
$\lvert T_{11}^{22}\rvert \leqslant (\frac{1}{2}\rho_{00}\rho_{33})^{\frac{1}{2}}$	.15±.14 ⩽ .15±.09	.07±.08 ⩽ .21±.05	.07±.10 ⩽ complex	.08±.13 ⩽ .18±.05	.07±.16 ⩽ .12±.16	.06±.17 ⩽ .22±.07
$\lvert T_{22}^{22}\rvert \leqslant (\rho_{33}(1-\rho_{00}-2\rho_{33}))^{\frac{1}{2}}$	.03±.09 ⩽ .15±.06	.19±.10 ⩽ .19±.09	.09±.14 ⩽ .37±.05	.14±.12 ⩽ .21±.13	.01±.12 ⩽ .13±.12	.07±.18 ⩽ .06±.73
No of events	31	53	40	38	23	19

Table (4.13)

The moduli of the t- and the s-channel transversity tensors

The t-channel transversity frame

$\|t\|$ (GeV/c)^2	0.0-0.2	0.2-0.4	0.4-0.6	0.6-1.0
$(\mathrm{Re}\ T^{02}_{02})^2+(\mathrm{Im}\ T^{02}_{02})^2$	0.009±0.009	0.003±0.006	0.031±0.034	0.047±0.046
$(\mathrm{Re}\ T^{22}_{02})^2+(\mathrm{Im}\ T^{22}_{02})^2$	0.004±0.011	0.018±0.025	0.068±0.078	0.009±0.027
$(\mathrm{Re}\ T^{22}_{1-1})^2+(\mathrm{Im}\ T^{22}_{1-1})^2$	0.026±0.026	0.007±0.013	0.006±0.018	0.013±0.039
$(\mathrm{Re}\ T^{22}_{11})^2+(\mathrm{Im}\ T^{22}_{11})^2$	0.002±0.008	0.017±0.023	0.007±0.019	0.005±0.020
$(\mathrm{Re}\ T^{20}_{20})^2+(\mathrm{Im}\ T^{20}_{20})^2$	0.012±0.007	0.002±0.003	0.019±0.018	0.007±0.012
$(\mathrm{Re}\ T^{22}_{2-2})^2+(\mathrm{Im}\ T^{22}_{2-2})^2$	0.023±0.022	0.001±0.005	0.006±0.025	0.002±0.014
$(\mathrm{Re}\ T^{22}_{20})^2+(\mathrm{Im}\ T^{22}_{20})^2$	0.004±0.008	0.005±0.010	0.004±0.016	0.022±0.049
$(\mathrm{Re}\ T^{22}_{22})^2+(\mathrm{Im}\ T^{22}_{22})^2$	0.020±0.021	0.001±0.003	0.125±0.103	0.048±0.071
No of events	84	78	23	19

The s-channel transversity frame

$\|t\|$ (GeV/c)^2	0.0-0.2	0.2-0.4	0.4-0.6	0.6-1.0
$(\mathrm{Re}\ T^{02}_{02})^2+(\mathrm{Im}\ T^{02}_{02})^2$	0.006±0.008	0.005±0.007	0.034±0.036	0.038±0.040
$(\mathrm{Re}\ T^{22}_{02})^2+(\mathrm{Im}\ T^{22}_{02})^2$	0.003±0.009	0.013±0.021	0.074±0.082	0.017±0.036
$(\mathrm{Re}\ T^{22}_{1-1})^2+(\mathrm{Im}\ T^{22}_{1-1})^2$	0.026±0.026	0.005±0.012	0.005±0.018	0.013±0.040
$(\mathrm{Re}\ T^{22}_{11})^2+(\mathrm{Im}\ T^{22}_{11})^2$	0.004±0.010	0.019±0.025	0.006±0.019	0.005±0.023
$(\mathrm{Re}\ T^{20}_{20})^2+(\mathrm{Im}\ T^{20}_{20})^2$	0.015±0.008	0.003±0.003	0.021±0.019	0.007±0.013
$(\mathrm{Re}\ T^{22}_{2-2})^2+(\mathrm{Im}\ T^{22}_{2-2})^2$	0.026±0.024	0.002±0.006	0.004±0.021	0.003±0.018
$(\mathrm{Re}\ T^{22}_{20})^2+(\mathrm{Im}\ T^{22}_{20})^2$	0.006±0.011	0.004±0.008	0.003±0.012	0.028±0.057
$(\mathrm{Re}\ T^{22}_{22})^2+(\mathrm{Im}\ T^{22}_{22})^2$	0.038±0.028	0.002±0.006	0.162±0.121	0.036±0.055
No of events	84	78	23	19

4.11 Discussion of Results and Conclusions

The mass and width of the Δ^{++} are 1234 ± 8 MeV/c^2 and 122 ± 32 MeV/c^2 respectively and these values are in good agreement with other experiments. The total cross-section $\sigma(\omega^o \Delta^{++}) = 53 \pm 10$ μb. The production cross-section decreases with the incident momentum as p_{inc}^{-n} with n = 1.85, which is consistent with a non-strange meson exchange reaction.

The $d\sigma/d|t|$ and $d\sigma/d|t'|$ distributions show dips at $|t|$ (or $|t'|$) $\longrightarrow$ 0, as were reported in other experiments. These distributions are consistent with an exponential behaviour with an exponent of ≈4 GeV^{-2}. The values of the exponent as obtained from other experiments remain fairly constant over a wide range of energy which implies that there is no energy dependence on the value of the exponent. However, the exponential shape of the $d\sigma/d|t'|$ distribution does not depend on the ρ-propagator alone.

The dip near $|t|$ or $|t'|$ ≈0.25 $(GeV/c)^2$ may be a statistical fluctuation since it is less than two standard deviations away from the exponential fit to the data points. However, another dip as expected at $|t| \approx 0.6$ $(GeV/c)^2$ according to the Regge pole calculations [85] appears to be more prominent since it is more than two standard deviations away from the exponential behaviour.

The predictions of the ρ-exchange model on the density matrix elements as discussed in Section 2.7.1 are:

$$\left.\begin{aligned} \rho_{00} &= 0.0, \qquad \rho_{11} = 0.5 \\ \rho_{33} &= 0.375, \quad \text{Re}\,\rho_{3,-1} = 0.216 \text{ and } \text{Re}\,\rho_{31} = 0 \end{aligned}\right\} \quad (4.17)$$

Almost similar predictions of the pure Regge pole model are [86]:

$$\left.\begin{aligned} &\rho_{00} = 0.0, \qquad \rho_{10} = 0, \qquad \rho_{1-1} = 0.5 \\ &\rho_{33} = 0.375, \text{ Re } \rho_{3,-1} = 0.216 \text{ and Re } \rho_{31} = 0 \ . \end{aligned}\right\} \tag{4.18}$$

Neither of these predictions agree with the present experimental results.

Svensson [87] who studied the reaction (4.1) suggested that the above disagreements could be explained by taking into account the absorptive effects. But Gottfried et al. [88,89] and Jackson et al. [90] on the basis of theoretical calculations point out that the predictions of ρ-exchange model with absorptive effects are inadequate.

Le Bellac and Plaut [91] have shown that at $|t| = 0.6$ (GeV/c)^2

$$\rho_{11} = \rho_{1-1} \ , \tag{4.19}$$

in the t-channel helicity frame. The relation (4.19) is also obtained by Jackson and Pilkuhn [30,31], if only the natural parity occurs and $s \longrightarrow \infty$. The experimental results are not consistent with the above prediction.

On the other hand, Högaasen et al. [92] predicted on the basis of a ρ + B Regge pole model that

$$\rho_{11} = -\rho_{1-1} \ , \tag{4.20}$$

in the t-channel helicity frame at $|t| \simeq 0.6$ (GeV/c)^2. The experimental values of ρ_{11} and ρ_{1-1} are unequal but have opposite signs.

Jones [93] and Bialas et al. [94], independently, on the calculations of the Regge pole couplings and the quark model respectively predicted the following relation:

$$\rho_{11} + \rho_{1-1} = (4/3)\,\rho_{33} + (4/\sqrt{3})\rho_{3-1} \,. \qquad (4.21)$$

The relation (4.21) does not agree with the experimental results.

The Minnaert positivity conditions on the density matrix elements are satisfied except for the value of ρ_{00} in the s-channel helicity frame for the $|t|$ interval 0.2 - 0.3 $(GeV/c)^2$, where it is negative by two standard deviations. The mass distribution of 3-pion and the ω-decay matrix element, λ_ω distribution do not seem to be different from those of the other bins. Therefore, the negative value of ρ_{00} cannot be ascribed to the background events.

Other experiments [95,96], where ρ-exchange dominates, have reported a dip at $|t| = 0$ and another dip at $|t| \approx 0.5$ $(GeV/c)^2$ in the value of $\sigma_1^+ = \rho_{11} + \rho_{1-1}$ in the t-channel helicity frame. These dips also appear in the present experiment as shown in Figure (4.7). Another dip in the value of $\sigma_1^- = \rho_{11} - \rho_{1-1}$ at $|t| \approx 0.2$ $(GeV/c)^2$ also appears in Figure (4.7b), as expected according to the Regge pole model calculations [85].

The Regge pole model [86] predicts that the double statistical tensors $T_{00}^{22} = \frac{1}{4\sqrt{6}}$, $T_{02}^{22} = T_{20}^{22}$, T_{2-2}^{22} and T_{22}^{22} should be non-zero both in the t- and the s-channel helicity frames. Only T_{00}^{22} and T_{20}^{22} for the $|t|$ intervals 0.0 - 0.2 and 0.4 - 0.6 $(GeV/c)^2$ in the s-channel helicity frame respectively are significantly different from zero as given in Table (4.10).

The quark model [94] predicts that the double statistical tensors T_{00}^{22}, Re T_{02}^{22}, Im T_{02}^{22}, Re T_{20}^{22} and Im T_{20}^{22} should be non-zero both for the t- and the s-channel transversity frames. Only values of T_{00}^{22} for the $|t|$ interval 0.2 - 0.4 $(GeV/c)^2$ both for the t- and the s-channel transversity frames (these two values are the same) are significantly different from zero as given in Table (4.10).

It is concluded that the agreement with the predicted values of the statistical tensors is not too good.

The Donohue inequalities are satisfied with the predicted values except for the $|t|$-bin where ρ_{00} is non-physical in the s-channel helicity frame. The moduli of the transversity tensors are frame invariant within the statistical errors.

In view of the above discussion of results, it is concluded that the reaction mechanism is not yet clear for the reaction $\pi^+ p \longrightarrow \omega \Delta^{++}$.

CHAPTER 5

THE pB^+ FINAL STATE

5.1 Introduction

In this Chapter the reaction:

$$\pi^+ p \longrightarrow pB^+ \tag{5.1}$$

will be discussed.

The B-meson with a mass of about 1235 MeV/c^2 has been observed in several $\pi^+ p$ [46,49,51,54-56,68,97,98,126], $\pi^- p$ [55, 99-105,127] and $\bar{p}p$ [106-109,128] collisions at different energies. It was first discovered by Abolins et al. [46] in the reaction $\pi^+ p \longrightarrow p\pi^+\pi^+\pi^-\pi^o$ at 3.43 and 3.54 GeV/c and subsequently by Bondar et al. [110] in the reaction $\pi^- p \longrightarrow p\pi^-\pi^+\pi^-\pi^o$ at 4 GeV/c and the former gave it the name of the B-meson. Maor et al. [111] suggested that the peak in the mass of the $\omega\pi$ could be the result of the Deck effect [112]. Doubts were raised by Goldhaber et al. [113] and Chung et al. [114] in the subsequent studies of the B in the reactions $\pi^\pm p \longrightarrow p\omega\pi^\pm$. But Baltay et al. [106] confirmed the existence of the B-meson in $\bar{p}p$ annihilations: $\bar{p}p \longrightarrow \omega^o\pi^+\pi^-$.

The only established decay mode is $B \longrightarrow \omega\pi$, and the ω^o subsequently decays into (3π). The quantum numbers and the production properties of the B-meson are not yet firmly established. The strong decay of the $B \longrightarrow \omega\pi$ implies $I^G = 1^+$ but the apparent absence of $K\bar{K}$ and $\pi\pi$ decay modes lends support against the natural spin parity series like 1^- and 3^-.

Ascoli et al. [115] studied the reaction $\pi^- p \longrightarrow pB^-$ at an incident momentum of 5 GeV/c and concluded that the probability $|F_o|^2$ for the decay of the B-meson into zero-helicity of the ω^o is small. On the other hand the simple quark model [116] predicts $|F_o|^2 = 1$, in contradiction with the experimental results.

Neglecting $J \gtrsim 4$, these authors ruled out all J^P assignments except 1^+, 2^+ and 3^-. Similar results were obtained by Werbrouck et al. [117] who studied the reaction: $\pi^+ p \longrightarrow pB^+$ at the incident momenta of 3 to 5 GeV/c. Due to relatively low incident pion momenta in these experiments, it was difficult to separate the B-meson from the reflection of other resonances, in particular, the $\Delta(1236)$. But it is comparatively easy to isolate the $\Delta(1236)$ from the B(1235) in the present experiment.

In the first two Sections of this Chapter the total and the differential cross sections for the B production are presented. The frames of reference for the sequential decay of the B to the ω^o are discussed and from the angular distribution of the ω^o, the helicity amplitude F_λ is determined in the s-channel helicity frame.

The next Section gives the details of the spin analysis of the B in the t- and the s-channel helicity frames for different J^P assignments. The possibility of spin = 3 for the B is ruled out due to unphysical values of the spin density matrix elements in the s-channel helicity frame and from the consistency of the value of $\langle J_z^2 \rangle$ as determined in two different ways (see Table (5.3)). Evidence favouring the two possibilities of $J^P = 1^+$ or 2^+ is given.

Towards the end of the Chapter, assuming the spin-parity assignment $J^P = 1^+$, the values of the spin density matrix elements in the t- and the s-channel helicity frames are determined and the ratio of $|D/S|$ wave decay is estimated.

Using the helicity amplitude $|F_o|^2$ and the spin density matrix elements, the different angular distributions of the B and the ω^o mesons are fitted with simple functions. Finally the results are discussed.

5.2 Total Cross Section

Figure (5.1) shows the mass distribution of $M(\pi^+\pi^+\pi^-\pi^o)$. There appears a shoulder around 1.3 GeV/c^2. The restriction of one of the neutral three-pion masses to the ω region (0.745 GeV/c^2 < M_ω < 0.825 GeV/c^2) shows the presence of the B^+ in the mass distribution of $M(\omega\pi^+)$.

Figure (5.2) shows the mass distribution of $M(\omega\pi^+)$ events (clear outline) and those that have $|t| \leq 1.0$ (GeV/c)^2 (cross-hatched) with 907 events and 753 events respectively. Here $|t|$ is four-momentum transfer from the incident pion to the B^+.

Figure (5.3) shows the mass distribution of $M(\omega\pi^+)$ events that have $|t| \leq 1.0$ (GeV/c)^2 and with Δ^{++} (1236) in the mass region (1.18 GeV/c^2 < $M(p\pi^+)$ < 1.32 GeV/c^2) antiselected to avoid reflection of the Δ isobar (see bottom right-hand corner on the Dalitz plot of Figure (3.11)).

Table (5.1) gives the mass and width of the B^+ as obtained by fitting the mass distribution of Figure (5.3) with an s-wave relativistic Breit-Wigner formula (see equations (2.2) to (2.4)), folded with a reoslution function (standard deviation, σ_{res} = 16 MeV) as described by Coyne et al. [73]. The shape of the background is estimated by eye.

Table (5.1)

Mass and width of the B^+

Reaction	Mass (MeV/c^2)	Γ (MeV/c^2)	σ (μb)	Background
$\pi^+p \longrightarrow pB^+$	1235 ± 12	120 ± 48	21 ± 6	∿ 30%

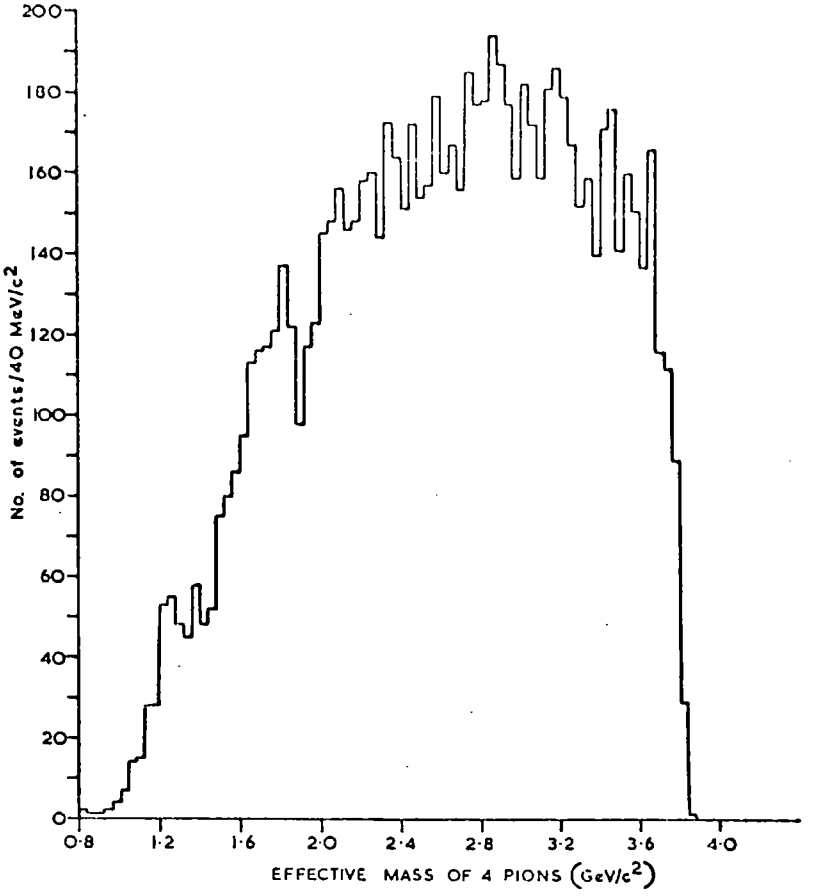

FIG. 5.1 $M(\pi^+\pi^+\pi^-\pi^0)$ FOR UNAMBIGUOUS AND 2-FOLD SELF-AMBIGUOUS EVENTS — 9081 EVENTS.

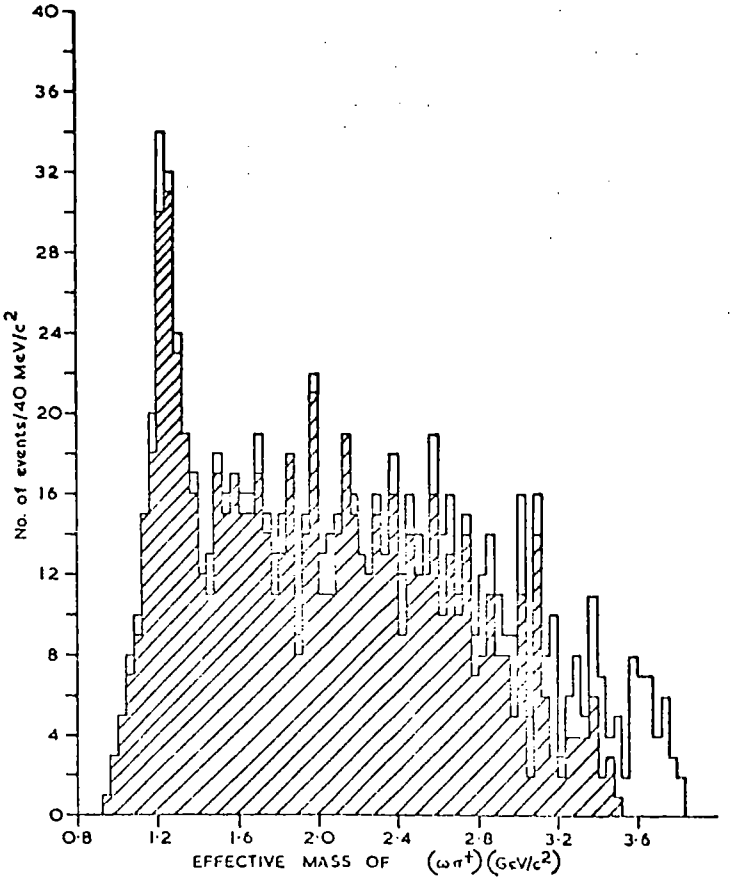

FIG. 5.2 $M(\omega\pi^+)$ FOR ALL EVENTS (CLEAR OUTLINE — 907 EVENTS) AND THOSE WITH $|t'_{\pi}/D^+| \leq 1.0 (GeV/c)^2$ (CROSS-HATCHED — 753 EVENTS).

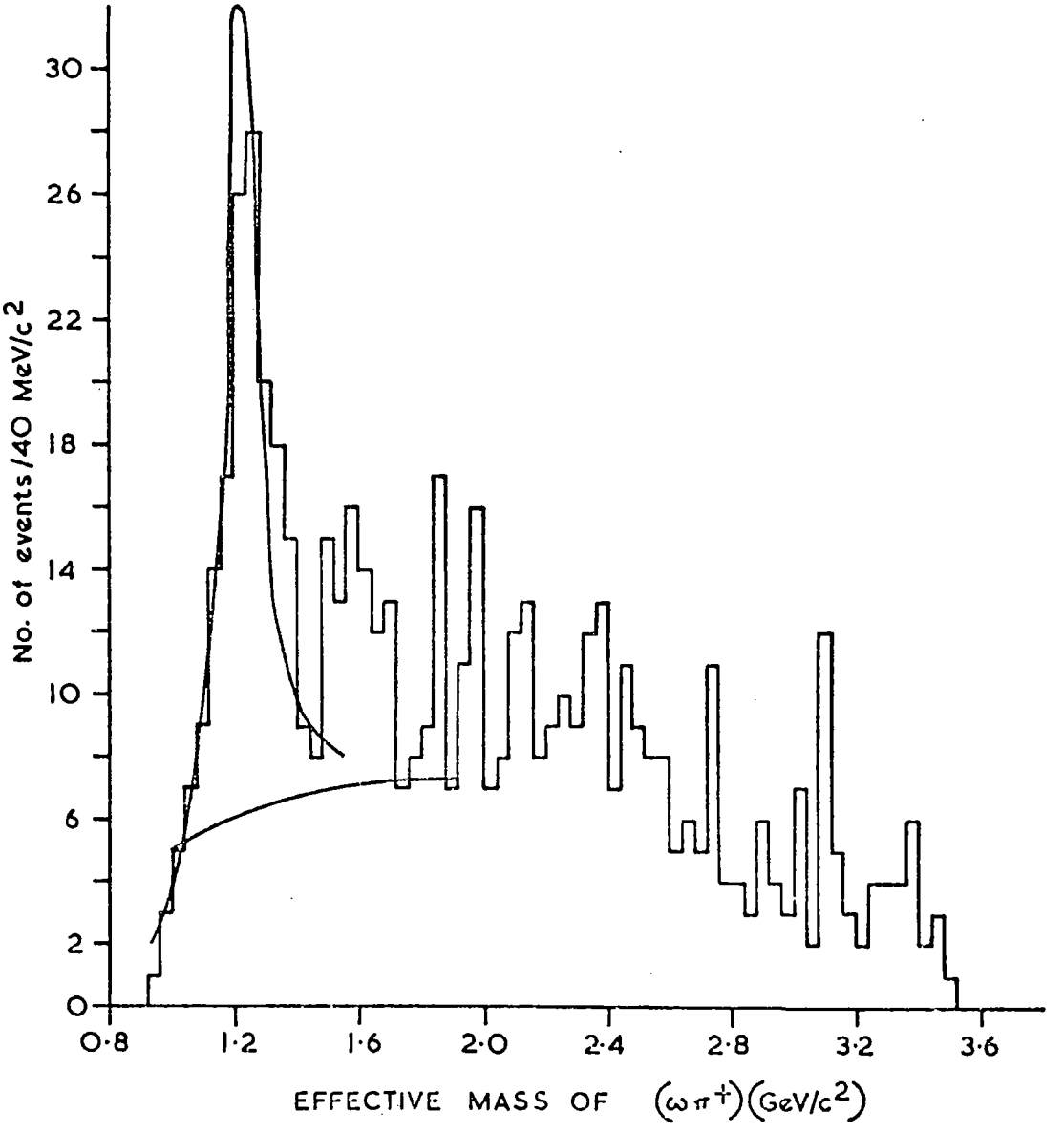

FIG. 5.3 $M(\omega\pi^+)$ FOR EVENTS WITH $|t_{\pi^+}/B^+| \leq 1{\cdot}0\ (\text{GeV/c})^2$ AND WITH Δ^{++} ANTISELECTED — 588 EVENTS. THE CURVE IS A FIT TO THE DATA AS EXPLAINED IN THE TEXT.

The errors on the mass and width are worked out by using equation (2.7). The fit was restricted to the $M(\omega\pi^+) < 1.48$ GeV/c^2. For the subsequent analysis, the mass interval of 1.16 to 1.32 GeV/c^2 was used for the B^+.

There are 100 events above the background. Thus the pB cross-section based on the total number of events in Figure (5.3) is (see Section 2.2):

$$\sigma\ (B^+) \quad = \quad 17 \pm 4\ \mu b.$$

The cross-section includes the statistical error on the number of events plus 10% for nomalization. Correcting 10% each for the $P(\chi^2)$ cut off and the unseen ω^o decay modes and 7% for the ω^o tails (see Section 3.3.2), the cross-section becomes:

$$\sigma\ (B^+) \quad = \quad 21 \pm 6\ (\mu b).$$

Figure (5.4) shows the comparison of this cross-section with those obtained at different incident momenta [46,49,51,55-56,68,97, 98]. The experimental errors are large, but assuming the cross-section varies as a power of the incident momentum, $\sigma = Kp_{inc}^{-n}$ (see equation(3.3)), a rough estimate for n is 1.5.

5.3 Differential Cross-Section

Figures (5.5 a-b) show the differential cross sections for the reaction (5.1) as functions of the four-momentum transfer $|t|$ and $|t'| = |t-t_{min}|$, where $|t|$ is the four-momentum transfer from the incident pion to the B^+ and t_{min} is the minimum value of the $|t|$. The events on which the graphs are based are selected in the B^+ mass band: $1.16\ \text{GeV}/c^2 < M(B^+) < 1.32\ \text{GeV}/c^2$ without background subtraction. The vertical error bars are only those due to statistics. The horizontal bars represent the interval chosen.

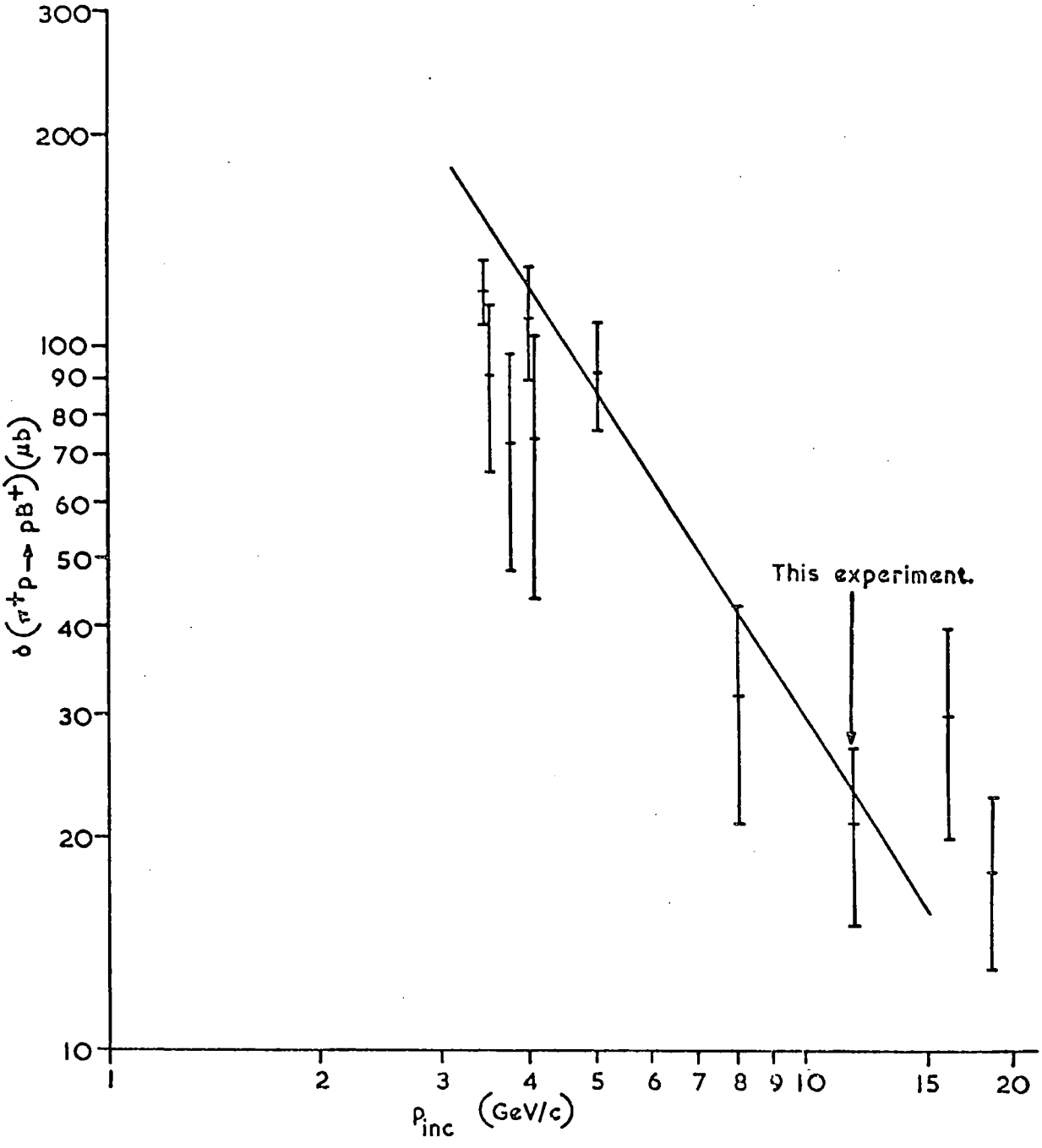

FIG. 5.4 TOTAL CROSS-SECTION FOR $\pi^+p \to pB^+$ AS A FUNCTION OF LABORATORY MOMENTUM (p_{inc}) OF INCIDENT PION.

Table (5.2) gives the differential cross sections normalised to the total pB cross-section of 21 μb. The transformation to a cross-section is obtained by normalising the total area to 21 μb which includes all the necessary corrections (see Sections 2.2 and 5.2).

Table (5.2)

Differential cross sections† for $\pi^+ p \longrightarrow pB^+$ normalised to the total pB^+ cross-section

$\|t\|$ or $\|t'\|$ $[(GeV/c)^2]$	$d\sigma/d\|t\|(pB^+)$ $[\mu b/(GeV/c)^2]$	$d\sigma/d\|t'\|(pB^+)$ $[\mu b/(GeV/c)^2]$
0.0 - 0.02	56 ± 22.9	56 ± 22.9
0.02 - 0.04	28 ± 16	84 ± 28
0.04 - 0.08	88.8 ± 20.4	70 ± 18
0.08 - 0.12	42 ± 14	32.7 ± 12
0.12 - 0.16	32.7 ± 12	37 + 13
0.16 - 0.20	37 ± 13	32.7 ± 12
0.20 - 0.24	28 ± 11	28 ± 11
0.24 - 0.32	18.7 ± 6.6	18.7 ± 6.6
0.32 - 0.40	18.7 ± 6.6	14.7 ± 6.6
0.40 - 0.48	14 ± 5.7	14 ± 5.7
0.48 - 0.56	11.7 ± 5.2	11.7 ± 5.2
0.56 - 0.86	3.7 ± 1.5	3.7 ± 1.5

† Errors quoted here are purely statistical, no allowance has been made for the noramlization errors.

Text continued on page 83.

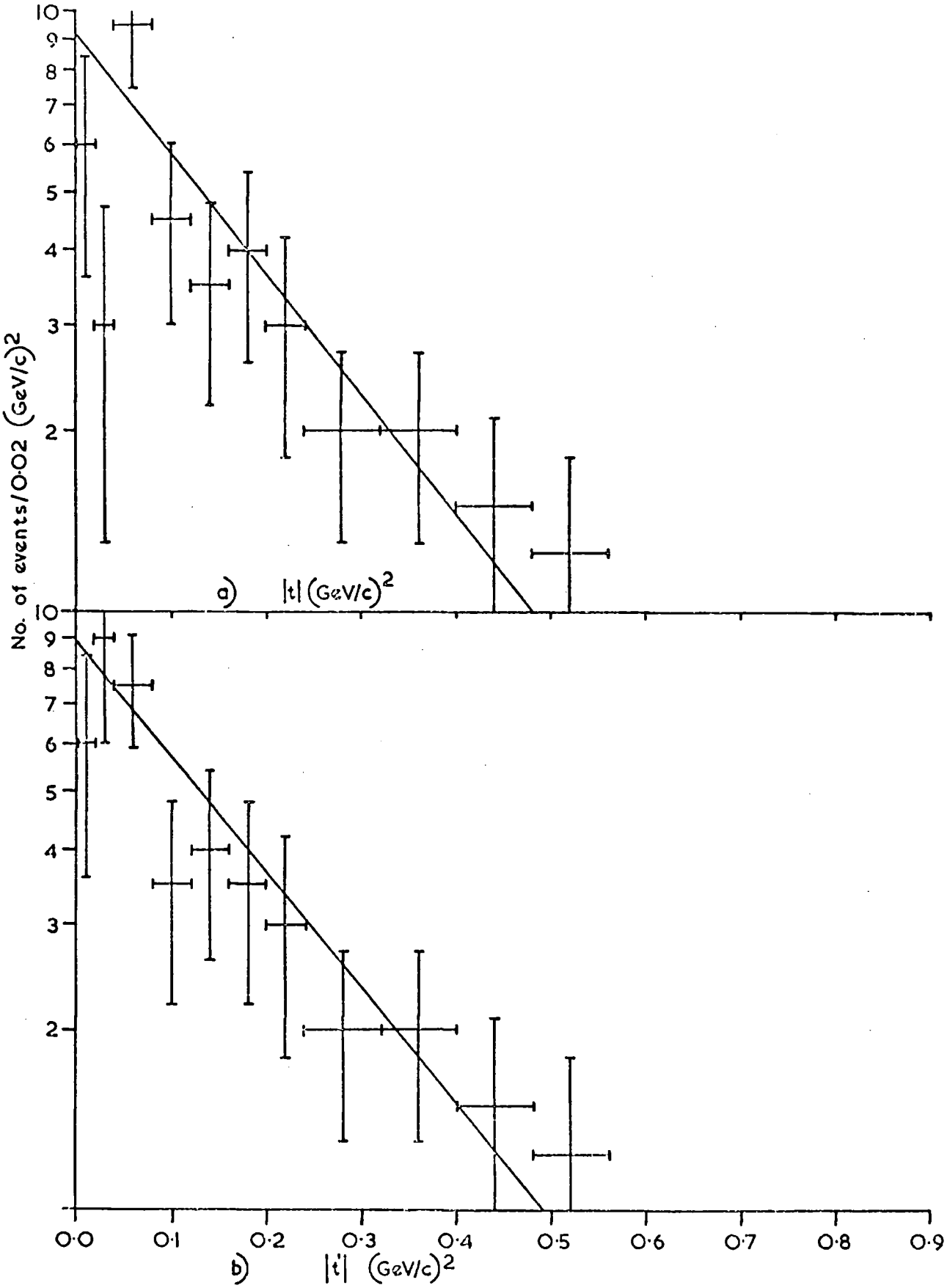

FIG. 5.5 DIFFERENTIAL CROSS-SECTION FOR $\pi^+p \rightarrow pB^+$ AS FUNCTIONS OF |t| AND |t'| : a) $(dN/d|t|)$, b) $(dN/d|t'|)$.

The errors shown in the table are only those due to statistics since an error in the normalisation will not change the shape of the differential cross-section as a function of $|t|$ (or $|t'|$).

The $|t|$ or $|t'|$ dependence of the differential cross-section for $|t|$ or $|t'| < 0.5$ $(GeV/c)^2$ is well described by the relations:

$$d\sigma/d|t| = a\, e^{-b|t|} ,$$

$$d\sigma/d|t'| = a\, e^{-b|t'|} .$$

The slope b is about 4 GeV^{-2} both for $|t|$ and $|t'|$. The values of b as obtained in other experiments at different energies over $|t'|$ range 0 - 0.6 $(GeV/c)^2$ are [68,51]: 2.4 and 4.7 GeV^{-2} at 5 and 8 GeV/c respectively. The energy dependence, if any, cannot be conclusively established because of lack of more data points.

The presence of dips in $d\sigma/d|t|$ or $d\sigma/d|t'|$ distributions is not clear in this experiment, due to the limited statistics. In the $|t'|$ region of $\lesssim 0.04$ $(GeV/c)^2$, the minimum proton momentum is 0.107 GeV/c, which corresponds to a range of about 3 mm. in liquid hydrogen. There may be some loss of events due to the difficulty of seeing the proton in unfavourable orientations, but the effect cannot be as large as the statistical uncertainty on the low $|t'|$ points.

5.4 Frames of Reference for the Sequential Decay

The frames of reference for determining the spin density matrix elements of the B are the same as discussed in Section 2.5. However, for the sequential decay:

$$B \longrightarrow \pi\omega^0$$
$$\qquad\quad \hookrightarrow \pi^+\pi^-\pi^0$$

the treatment of the ω decay requires additional information as given below with reference to Figure (5.6).

The analysis was done with the helicity-type axes. The right-handed coordinate systems xyz in the two categories of the helicity-type axes are:

(i) The t-channel helicity (or Gottfried-Jackson) frame for the B decay.

$$\left.\begin{aligned} \hat{y} &= \frac{\vec{p}_{inc} \times \vec{p}_{out}}{|\vec{p}_{inc}| \times |\vec{p}_{out}|} , && \text{(a)} \\ \hat{z} &= \frac{\vec{\pi}_{inc}}{|\vec{\pi}_{inc}|} , && \text{(b)} \\ \hat{x} &= \hat{y} \times \hat{z} . && \text{(c)} \end{aligned}\right\} \quad (5.2)$$

(ii) The s-channel helicity frame for the B decay.

$$\left.\begin{aligned} \hat{y} &= \frac{\vec{p}_{inc} \times \vec{p}_{out}}{|\vec{p}_{inc} \times \vec{p}_{out}|} , && \text{(a)} \\ \hat{z} &= -\frac{\vec{p}_{out}}{|\vec{p}_{out}|} , && \text{(b)} \\ \hat{x} &= \hat{y} \times \hat{z} . && \text{(c)} \end{aligned}\right\} \quad (5.3)$$

(iii) The s-channel helicity frame for the decay of the ω^o.

$$\left.\begin{aligned} \hat{y}' &= \frac{\vec{z} \times \vec{z}'}{|\vec{z} \times \vec{z}'|} , && \text{(a)} \\ \hat{z}' &= \text{momentum of the } \omega^o \text{ in rest system of the B} , && \text{(b)} \\ \hat{x}' &= \hat{y}' \times \hat{z}' , && \text{(c)} \\ \hat{n}_\omega &= \frac{\vec{\pi}^- \times \vec{\pi}^o}{|\vec{\pi}^- \times \vec{\pi}^o|} . && \text{(d)} \end{aligned}\right\} \quad (5.4)$$

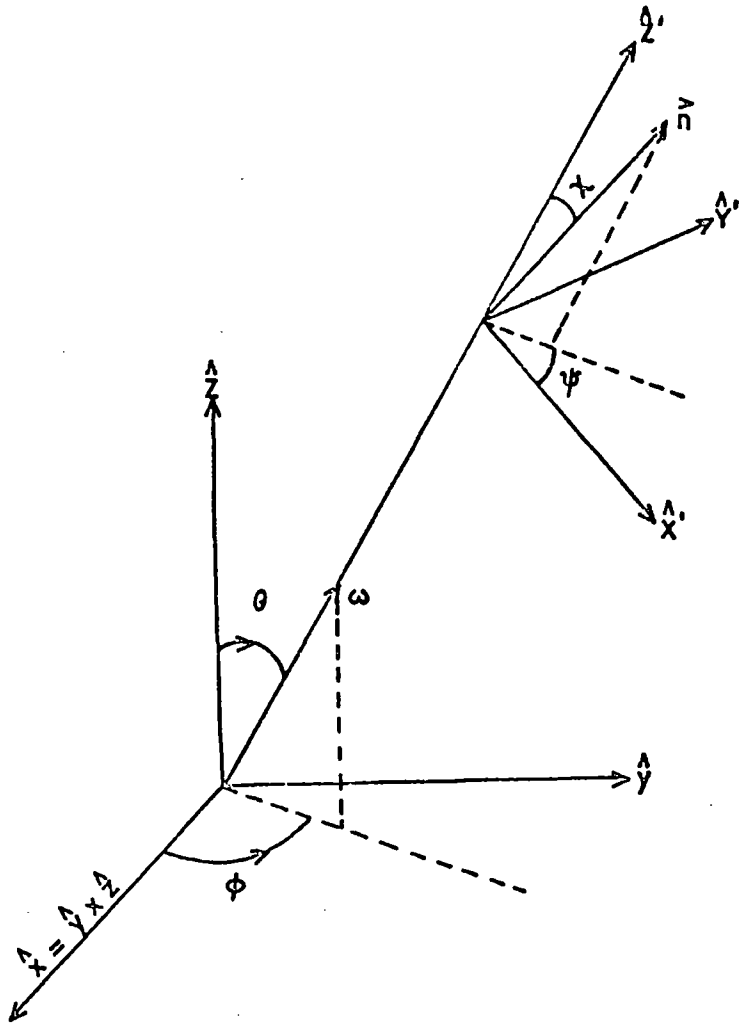

FIG. 5.6 THE POLAR AND AZIMUTHAL ANGLES FOR THE B DECAY IN THE t-AND s-CHANNEL HELICITY FRAMES REFERRED TO AXES $\hat{x}\,\hat{y}\,\hat{z}$ AND CORRESPONDING ANGLES OF THE NORMAL TO THE ω DECAY PLANE FOR THE ω DECAY IN THE s-CHANNEL HELICITY FRAME REFERRED TO AXES $\hat{X}'\,\hat{Y}'\,\hat{Z}'$.

The symbols in formulas (5.2) to (5.3) mean the momenta of the particles in the rest frame of the B except for equation (5.3(b)), where $\overrightarrow{p_{out}}$ denotes the momentum of the outgoing proton in the C.M.S. The z in equation (5.4(a)) is replaced by equation (5.2(b')) or equation (5.3(b)), depending on whether the B is being discussed in the t- or the s-channel helicity frame. The normal to the ω decay plane $\overrightarrow{n_{\omega}}$ in the ω rest system as given by equation (5.4(d)) is determined by the momenta of the decay particles π^- and π^o. The ω rest system is obtained first by transforming to the B rest frame and then to the ω rest frame as seen in the B rest system.

The decay angles θ and ϕ are the polar and the azimuthal angles of the ω in the B rest frame and χ and ψ are the corresponding angles of the normal to the ω decay plane. The polar and the azimuthal angles are then worked out in the same way as given in equation (2.21).†

5.5 Helicity Amplitudes of the ω^o

To describe the sequential decay of the $B \longrightarrow \omega\pi$, $\omega \longrightarrow (3\pi)$, the method outlined by Berman and Jacob [118] is used. The matrix element M for the decay of the B meson of spin J and z-component m into $\omega\pi$ and subsequent decay of the ω^o into 3-pion can be expressed in terms of the ω helicity amplitudes F_λ as:

$$M \propto \sum_{\lambda=0,\pm1} F_\lambda \, D^{*J}_{m,\lambda} (\phi \; \theta \; 0) \; D^{*O}_{\lambda 1} (\psi \; \chi \; 0) . \qquad (5.5)$$

---

† It can be shown that the polar angle χ for the sequential decay of the ω^o is invariant whether the B is in the t- or the s-channel helicity frame.

The angles θ and ϕ are the polar and azimuthal angles of the ω in the B rest frame, and χ and ψ are the corresponding angles of the normal to the ω decay plane in the s-channel helicity frame of the ω. The normalisation used is: $\sum_{\lambda} |F_\lambda|^2 = 1$.

The decay probability $W(\cos\theta,\phi;\ \cos\chi,\psi)$ can be written as [117]:

$$\left.\begin{aligned} W(\cos\theta,\phi;\ \cos\chi,\psi) = \frac{3(2J+1)}{16\pi^2} \sum_{L=0}^{2J} \sum_{\substack{mm' \\ \lambda\lambda'}} (-1)^m \rho_{mm'} F_\lambda F^*_{\lambda'} \cdot \\ .C(JJL;\ -mm')\ C(JJL;\ -\lambda\lambda')\ D^L_{m'-m,\lambda'-\lambda}(\phi\,\theta\,\psi) d^1_{-\lambda 0}(\chi) d^1_{\lambda' 0}(\chi). \end{aligned}\right\} \quad (5.6)$$

The width of the ω^o is neglected and the $\rho_{mm'}$ are the spin density matrix elements of the B-meson in equation (5.6). Parity conservation in the decay process gives the relation:
$F_\lambda = \varepsilon\, F_{-\lambda} (\lambda = 0, \pm 1)$, where $\varepsilon = P(-1)^{J+1}$ and P is the parity of the B meson.

The helicity amplitude F_o is allowed to be non-zero for the unnatural spin-parity series: 1^+, 2^-, 3^+ ..... . For $J^P = 0^-$ only the F_o amplitude is present. One obtains the distribution of $\cos\chi$ on integrating equation (5.6).

$$\left.\begin{aligned} W(\cos\chi) &= \tfrac{3}{2} \left(|F_o|^2 \cos^2\chi + |F_1|^2 \sin^2\chi\right) , && \text{(a)} \\ &= \tfrac{3}{4} \left(1-|F_o|^2 + (3|F_o|^2 - 1) \cos^2\chi\right), && \text{(b)} \\ &= \tfrac{1}{2} \left(1+ (3|F_o|^2 - 1)\ P_2\ (\cos\chi)\right) , && \text{(c)} \end{aligned}\right\} \quad (5.7)$$

where $P_2\ (\cos\chi)$ is a Legendre polynomial. Then it follows that:

$$|F_o|^2 = \tfrac{1}{3} \left(5 < P_2\ (\cos\chi) > + 1\right), \quad (5.8)$$

where $< P_2\ (\cos\chi) >$ is the average value of $P_2\ (\cos\chi)$.

Figure (5.10e) shows the distribution of cosχ of all $(\omega\pi^+)$ events within the B mass region. It clearly shows the dominance of $\sin^2\chi$ contribution which implies a small value of $|F_o|^2$. This rules out $J^P = 0^-$ for the B meson. The helicity-zero decay probability $|F_o|^2$ calculated from the mean value of $P_2(\cos\chi)$ using the formula (5.8) gives $|F_o|^2 = 0.09 \pm 0.07$.

Figure (5.7a) shows the $|F_o|^2$ as a function of $M(\omega\pi^+)$. Figure (5.7b) shows the dependence of $\Sigma P_2(\cos\chi)$ on the $(\omega\pi^+)$ mass. In both these figures the upper mass limit is 1.96 MeV/c^2 in the 160 MeV/c^2 intervals. The horizontal and vertical error bars respectively are the mass interval chosen and the statistical errors. In both these figures, a structure appears in the B region due to a more or less abrupt change in the angular distributions there.

The value of $|F_o|^2$ has been evaluated both by the method of moments and by fitting formula (5.7c) by the maximum likelihood fit. The results are consistent with each other and as found by other workers the value of $|F_o|^2$ is small. These results are summarised in Figure (5.8).

5.6 Spin and Parity Analysis

The following two different methods were used to get further information on the spin and parity of the B meson.

(i) The first method uses the fact that the expectation value:

$$\langle J_z^2 \rangle = \sum_{m=-J}^{m=J} m^2 \rho_{mm} \quad , \tag{5.9}$$

can be obtained from the observed moments. Here ρ_{mm} are the diagonal spin matrix elements of the B meson.

The ρ_{mm} can be calculated from the distribution of $W(\cos\theta)$ which is obtained by integration of equation (5.6).

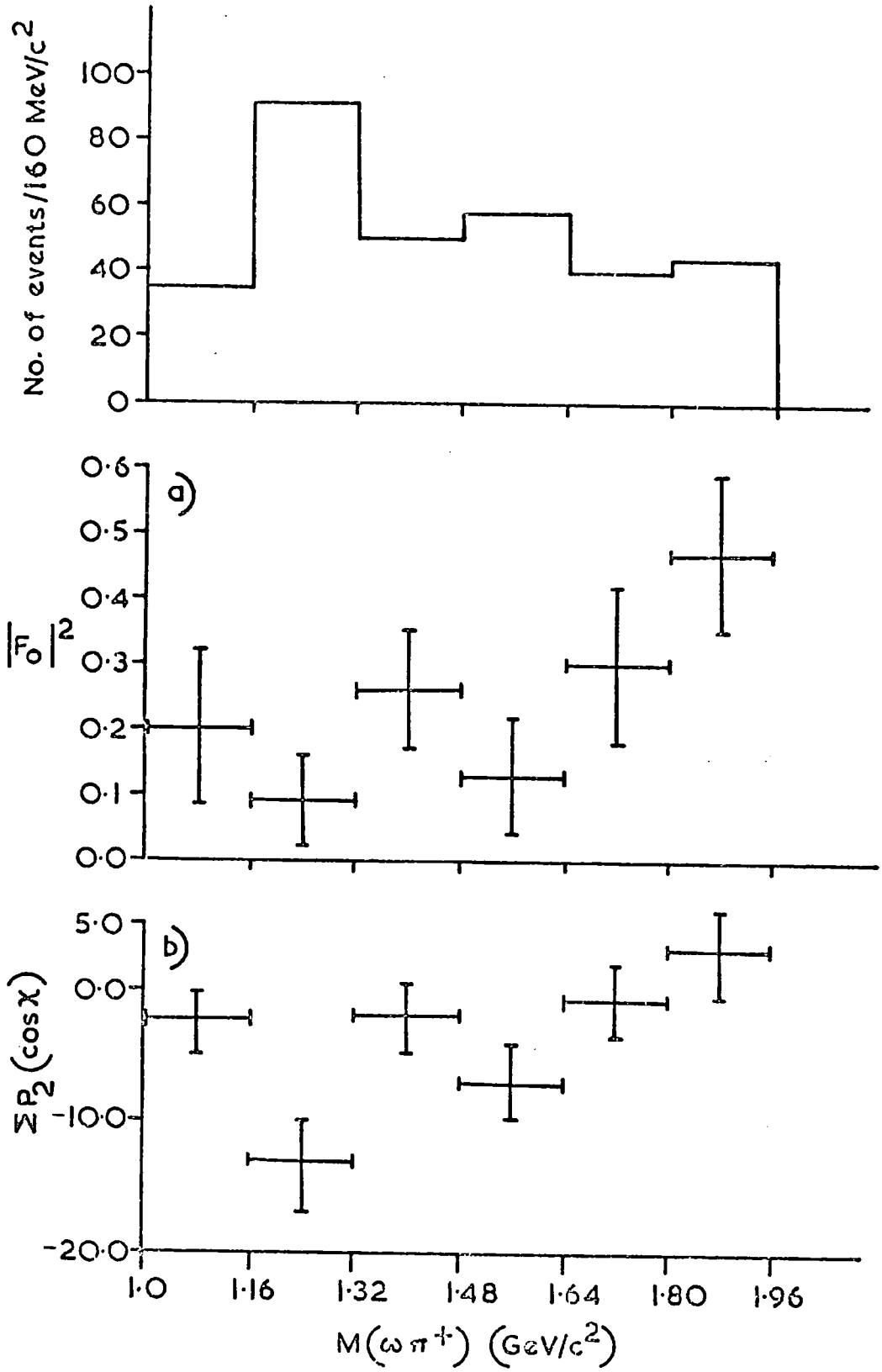

FIG. 5.7 a) $|F_0|^2$ AS A FUNCTION OF $M(\omega\pi^+)$.

b) $\Sigma P_2(\cos\chi)$ AS A FUNCTION OF $M(\omega\pi^+)$.

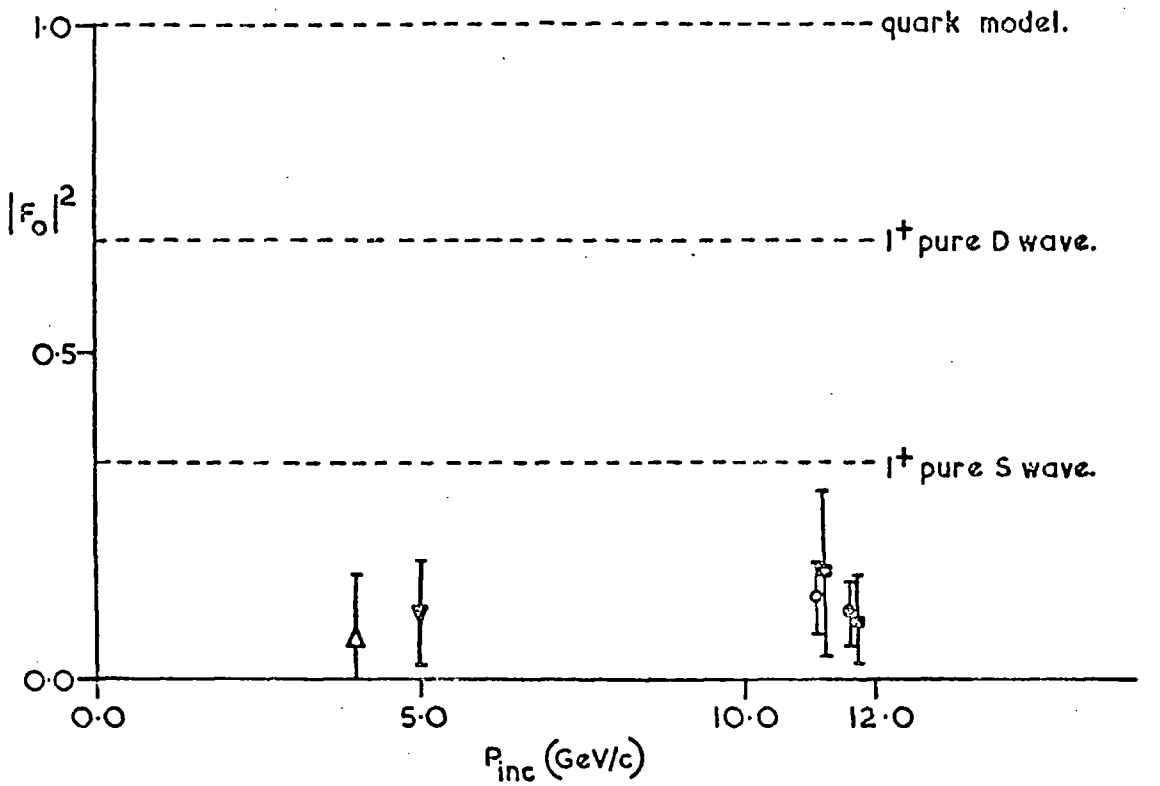

FIG. 5.8 $|F_0|^2$ FOR VARIOUS EXPERIMENTS AND PREDICTIONS ON ITS VALUE.

▼ REF. [115] , Δ REF. [117]

▣ BY MOMENTS , ⊙ BY FIT IN THIS EXPERIMENT .

□ BY MOMENTS REF. [2] , ○ BY FIT REF. [2].

$$W(\cos\theta) = \frac{2J+1}{2} \sum_{\substack{L=0 \\ \lambda,m}}^{2J} (-1)^{m-\lambda} \rho_{mm} |F_\lambda|^2 \, C(JJL,-mm)\, C(JJL,-\lambda\lambda)\, P_L(\cos\theta). \quad (5.10)$$

One obtains the ρ_{mm} from the $\cos\theta$ distribution alone. The explicit formulae for $J = 1, 2, 3$ are† (see Appendix C for derivation).

$$\left.\begin{aligned}
J = 1: \quad \rho_{11} &= \frac{1}{3} + \frac{5\langle P_2(\cos\theta)\rangle}{3(1-3|F_o|^2)} ; && \text{(a)} \\
J = 2: \quad \rho_{11} &= \frac{1}{5} + \frac{\langle P_2(\cos\theta)\rangle}{(1+|F_o|^2)} - \frac{18\langle P_4(\cos\theta)\rangle}{5(5|F_o|^2-2)} , && \text{(b)} \\
\rho_{22} &= \frac{1}{5} - \frac{2\langle P_2(\cos\theta)\rangle}{(1+|F_o|^2)} + \frac{9\langle P_4(\cos\theta)\rangle}{10(5|F_o|^2-2)} ; && \text{(c)} \\
J = 3: \quad \rho_{11} &= \frac{1}{7} + \frac{15\langle P_2(\cos\theta)\rangle}{7(3+|F_o|^2)} + \frac{9\langle P_4(\cos\theta)\rangle}{7(5|F_o|^2+1)} - \frac{39\langle P_6(\cos\theta)\rangle}{7(7|F_o|^2-3)} , && \text{(d)} \\
\rho_{22} &= \frac{1}{7} - \frac{9\langle P_4(\cos\theta)\rangle}{(5|F_o|^2+1)} + \frac{78\langle P_6(\cos\theta)\rangle}{35(7|F_o|^2-3)} , && \text{(e)} \\
\rho_{33} &= \frac{1}{7} - \frac{25\langle P_2(\cos\theta)\rangle}{7(3+|F_o|^2)} + \frac{27\langle P_4(\cos\theta)\rangle}{7(5|F_o|^2+1)} - \frac{13\langle P_6(\cos\theta)\rangle}{25(7|F_o|^2-3)} . && \text{(f)}
\end{aligned}\right\} \quad (5.11)$$

ρ_{00} is always fixed by the trace condition: $\sum_{m=-J}^{J} \rho_{mm} = 1$.

(ii) The second method is by using the following formula. Integration of equation (5.6) for $L = 2$, $M = 0$ gives the following expectation values: [115]:

---

† One gets the unnatural spin parity series: 1^+, 2^-, 3^+ .... by putting the measured value of $|F_o|^2$ and the natural spin parity series: 1^-, 2^+, 3^-.... by setting the value of $|F_o|^2 = 0$ in the different formulae (5.11) to obtain values as listed in Table(5.3).

$$\langle 2\ \mathrm{Re}\ D^{2}_{O2}\ (\phi\ \theta\ \psi)\rangle = 4|F_1|^2 \left(\frac{3}{8}\right)^{\frac{1}{2}} \epsilon \left\{ \frac{J(J+1) - 3\langle J_z^2\rangle}{(2J+3)(2J-1)} \right\}, \qquad (5.12)$$

$$\langle D^{2}_{OO}\ (\phi\ \theta\ \psi)\rangle = 2|F_1|^2 \left\{ \frac{1}{2|F_1|^2} - \frac{3}{J(J+1)} \right\} \left\{ \frac{J(J+1) - 3\langle J_z^2\rangle}{(2J+3)\ (2J-1)} \right\}. \qquad (5.13)$$

Dividing equation (5.12) by equation (5.13) and substituting the values of $\langle D^{2}_{OO}\ (\phi\ \theta\ \psi)\rangle$, ϵ and $|F_1|^2$ gives:

$$\langle J_z^2\rangle = J(J+1)/3 + \frac{(2J+3)(2J-1)\sqrt{6}}{9(1-|F_o|^2)} \cdot (-1)^J \cdot P \cdot 2\langle \mathrm{Re}\ D^{2}_{O2}\ (\phi\ \theta\ \psi)\rangle . \qquad (5.14)$$

The results from the above two methods for the t- and the s-channel helicity frames are listed in Table (5.3) on page 90.

There is evidence against J = 3 when one calculates ρ_{mm} in the s-channel helicity frame. The condition $0 \leqslant \rho_{mm} \leqslant \frac{1}{2}$ for m = 1,.....J should hold due to parity conservation. But values obtained are unphysical for J = 3 by several standard deviations (see last two lines of Table (5.3)). Therefore the possibility for J = 3 is ruled out.

Berman and Jacob [118] have shown that certain ratios of $\langle D^{L}_{mm'}\rangle$ are independent of the ω helicity states and of the $\rho_{mm'}$ of the parent particle, where L = 0,....2J, and M = m' - m. Following are the relations independent of $\rho_{mm'}$.

$$\frac{\langle \mathrm{Re}\ D^{2}_{M2}\rangle + \langle \mathrm{Re}\ D^{2}_{M-2}\rangle}{\langle 2\mathrm{Re}\ D^{2}_{MO}\ \frac{1}{2}\ (3-5\cos^2\chi)\rangle} = (-1)^{J+1}\ P\sqrt{3/8}\ \frac{J(J+1)}{J(J+1)-3} . \qquad (5.15)$$

The experimental values of the left-hand side of equation (5.15) both for M = 0 and M = 2 together with the calculated values of the right-hand side of equation (5.15) for different J^P assignments are listed in Table (5.4) on page 91.

Table (5.3)

$\langle J_z^2 \rangle$ in the t- and the s-channel helicity frames

using equations (5.11) and (5.14)

Frame of reference	J	P	ρ_{mm} using Eq.(5.11)			$\langle J_z^2 \rangle$	
			ρ_{11}	ρ_{22}	ρ_{33}	from $\Sigma_m^2 \rho_{mm}$	from Eq.(5.14)
The t-channel helicity frame	1	+	0.20±0.09	-	-	0.40±0.18	0.50±0.10
		-	0.22±0.09	-	-	0.44±0.18	0.84±0.10
	2	+	0.08±0.08	0.33±0.08	-	2.8 ±0.6	2.7 ±0.4
		-	0.07±0.08	0.33±0.08	-	2.8 ±0.6	1.2 ±0.4
	3	+	0.12±0.08	0.31±0.25	0.13±0.13	5.1 ±0.9	2.3 ±0.9
		-	0.10±0.08	0.41±0.25	0.09±0.15	5.2 ±0.9	5.5 ±0.9
The s-channel helicity frame	1	+	0.36±0.08	-	-	0.72±0.17	0.80±0.10
		-	0.40±0.08	-	-	0.80±0.17	0.66±0.10
	2	+	-0.02±0.06	0.19±0.07	-	1.50±0.7	1.5 ±0.4
		-	-0.04±0.06	0.21±0.07	-	1.6 ±0.6	2.0 ±0.4
	3	+	-0.04±0.04	1.0 ±0.2	-0.27±0.12	3.9 ±0.8	3.0 ±0.9
		-	-0.03±0.04	1.1 ±0.2	-0.29±0.12	2.7 ±0.8	4.9 ±0.9

Table (5.4)

Values of equation (5.15)

J^P	1^+	2^+	1^-	2^-	3^-	3^+
Calculated values of R.H.S. of equation (5.15) for different J^P assignments	-1.2	-1.2	+1.2	+1.2	-0.8	+0.8
Experimental values of L.H.S. of equation (5.15) for M = 0 and M = 2	-1.3 ± 2.3					

The experimental values of L.H.S. of equation (5.15) have large errors but are negative both for M = 2 and M = 0. Therefore $J^P = 1^+$ and 2^+ are favoured. For odd M the moments vanish due to conservation of parity. The ratio for M = 0 uses the moments $\langle D^2_{00}(3-5\cos^2\chi)\rangle$, assuming no structure in the B region and hence simply gives the sign of the ratio.

The relevant moments are shown in Figure (5.9) as functions of $M(\omega\pi^+)$ per 160 MeV/c^2 intervals of mass. The horizontal and vertical error bars respectively are the mass interval chosen and the statistical errors. A structure appears in the B region due to an abrupt change in the angular distribution there regardless of the large errors in the values of these functions.

To summarise the results of this Section, J = 3 is ruled out from the consistency of $\langle J_z^2\rangle$ evaluated from two different methods as listed in Table (5.3) and from the experimental negative values of equation (5.15), $J^P = 1^+, 2^+$ are favoured over $J^P = 1^-, 2^-$ for the spin and parity of the B meson.

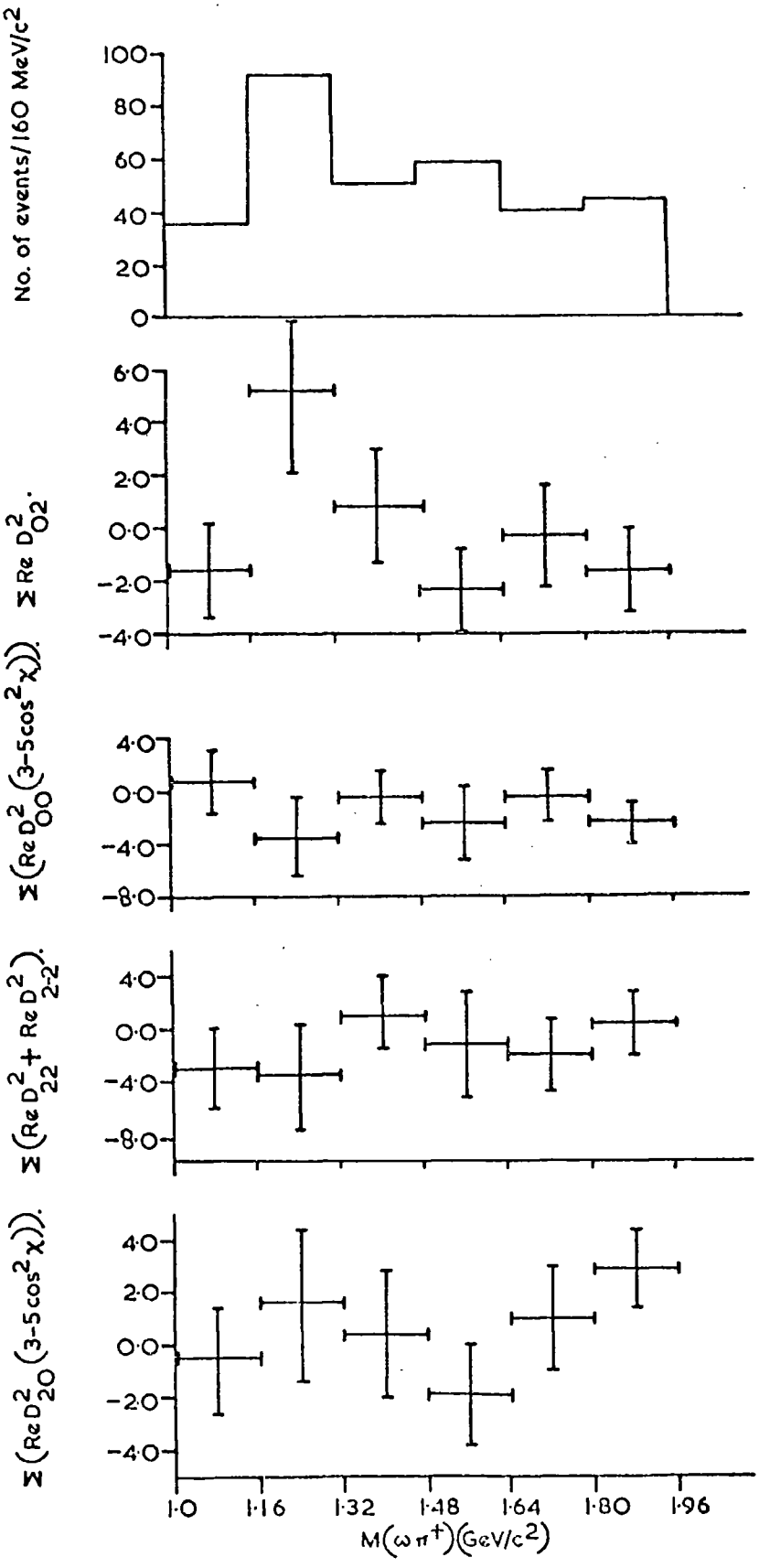

FIG. 5.9 $\Sigma\left(\mathrm{Re}\, D^2_{M2} + \mathrm{Re}\, D^2_{M-2}\right)$ AND $\Sigma\left(\mathrm{Re}\, D^2_{M0}\left(3-5\cos^2\chi\right)\right)$ FOR EVENTS PER 160 MeV/c^2 BINS AS FUNCTIONS OF $M(\omega\pi^+)$M IN D MATRICES= 0,2.

5.7 Spin Density Matrix Elements and |D/S| Wave Ratio

Assuming the spin-parity assignment of $J^P = 1^+$ for the B meson, an estimate of the spin density matrix elements and the ratio of D- to S- wave decay will be presented in this Section.

The decay angular distribution of the B in the t- and s-channel helicity frames is given by (see Appendix C for derivation):

$$W(\cos\theta,\phi) = \frac{3}{4\pi}\left[\frac{1-3|F_o|^2}{4}(1-3\,\rho_{00})\cos^2\theta + \frac{1}{4}(1+|F_o|^2 + \rho_{00}(1-3|F_o|^2)) + \frac{1-3|F_o|^2}{2}(\rho_{1-1}\sin^2\theta\cos2\phi + \sqrt{2}\,\mathrm{Re}\rho_{10}\sin2\theta\cos\phi)\right] \tag{5.16}$$

Integrating equation (5.16) first over ϕ and then over $\cos\theta$ gives:

$$\left.\begin{aligned} W(\cos\theta) &= \frac{3}{4}\left[\frac{1-3|F_o|^2}{2}(1-3\rho_{00})\cos^2\theta + \frac{1+|F_o|^2}{2} + \frac{1-3|F_o|^2}{2}\rho_{00}\right] && \text{(a)} \\ W(\phi) &= \frac{1}{2\pi}\left[1-(1-3|F_o|^2)\rho_{1-1} + 2(1-3|F_o|^2)\,\rho_{1-1}\cos^2\phi\right] && \text{(b)} \end{aligned}\right\} \tag{5.17}$$

By a suitable choice of $f(\cos\theta,\phi)$ and replacing $W(\cos\theta,\phi)$ in equation (4.2) by equation (5.16) one obtains the following relations:

$$\left.\begin{aligned} \rho_{00} &= \frac{2 - |F_o|^2 - 5\langle\cos^2\theta\rangle}{1 - 3|F_o|^2}\,, && \text{(a)} \\ \rho_{1-1} &= \frac{5}{2(1-3|F_o|^2)}\langle\sin^2\theta\cos2\phi\rangle\,, && \text{(b)} \\ \mathrm{Re}\,\rho_{10} &= \frac{5\sqrt{2}}{4(1-3|F_o|^2)}\langle\sin2\theta\cos\phi\rangle\,. && \text{(c)} \end{aligned}\right\} \tag{5.18}$$

Further relations for ρ_{1-1} can be obtained from equations (5.16) and (5.6) which depend only on the azimuthal angles, e.g.,

$$\left.\begin{aligned} \rho_{1-1} &= \frac{2}{1 - 3|F_o|^2} \langle \cos 2\phi \rangle , \qquad \text{(d)} \\ \rho_{1-1} &= \frac{2}{|F_o|^2 - 1} \langle \cos 2(\phi + \psi) \rangle . \qquad \text{(e)} \end{aligned}\right\} \quad (5.18)$$

The values of the spin density matrix elements have been obtained in the t- and the s-channel helicity frames both by fitting formula (5.16) and by using formulae (5.18) using the value of $|F_o|^2 = 0.09 \pm 0.07$. The precise value of ρ_{00} was obtained from $\langle J_z^2 \rangle$ (see Table(5.3)).

The spin density matrix elements of the B^+ in both the t- and the s-channel helicity frames are listed in Table (5.5).

Table (5.5)

Spin density matrix elements of the B^+ for $J^P = 1^+$.

The element	The t-channel helicity frame	The s-channel helicity frame
ρ_{00}	0.5 ± 0.1	0.2 ± 0.1
Re ρ_{10}	0.12 ± 0.12	0.0 ± 0.2
ρ_{1-1}	0.0 ± 0.2	0.0 ± 0.2

The value of ρ_{1-1} is sensitive to the method used (e.g., equations (5.18 b,d,e) give different values). These values vary between 0.15 and -0.16 with very large errors, e.g., ± 0.16. It is, therefore, concluded that ρ_{1-1} is very small being compatible with zero.

Inspection of Table (5.5) shows that the B is not strongly aligned in both the t- and the s-channel helicity frames.

Assuming $J^P = 1^+$ for the B, only D and the S waves are present for the decay of $B \longrightarrow \omega\pi$. The relations between the helicity amplitudes F_λ and the orbital angular momentum amplitudes $\tilde{F}_L$ are (see Appendix C for derivation):

$$\left.\begin{aligned} \tilde{F}_D &= \frac{\sqrt{2}}{3}\ (F_1 - F_o)\,, && \text{(a)} \\ \tilde{F}_S &= \frac{1}{3}\ (F_o + 2F_1)\,. && \text{(b)} \end{aligned}\right\} \quad (5.19)$$

Then the $|D/S|$ ratio is:

$$\frac{|\tilde{F}_D|}{|\tilde{F}_S|} = \sqrt{\frac{1 + |F_o|^2 - 4\mathrm{Re}\ F_o^* F_1}{2 - |F_o|^2 + 4\mathrm{Re}\ F_o^* F_1}}\,. \quad (5.20)$$

In order to determine the value of $\mathrm{Re}\ F_o^* F_1$, the following moments were used:

$$\left.\begin{aligned} \mathrm{Re}\ F_o^* F_1 &= \frac{5\sqrt{6}\ (1-|F_o|^2) < \mathrm{Re}\ D^2_{M1}\ (\phi\ \theta\ \psi)\ d^2_{10}(\chi) >}{12 < \mathrm{Re}\ D^2_{M2} < (\phi\ \theta\ \psi) >}\,, && \text{(a)} \\ &= \frac{5\sqrt{2}}{4\ \mathrm{Re}\rho_{10}} < \sin 2\theta \cos(\psi + \phi) >\,, && \text{(b)} \\ &= -\frac{5\sqrt{2}}{\mathrm{Re}\rho_{10}} < \cos\theta \sin 2\theta \cos(\phi + \psi) >\,. && \text{(c)} \end{aligned}\right\} \quad (5.21)$$

Equation (5.21a) is independent of M[117] and the most precise value obtained from this expression is:

$$\mathrm{Re}\ F_o^* F_1 = 0.5 \pm 0.4\,.$$

Substituting the value of $|F_o|^2$ within one standard deviation $|F_o|^2 = 0.09 \pm 0.07$ and that of $\mathrm{Re}\ F_o^* F_1$ in equation (5.20) gives values of $(|\tilde{F}_D|/|\tilde{F}_S|)$ ranging from 0.2 to 1.7

Finally Table (5.6) gives the Lengendre polynomials and D matrices used in this Chapter to evaluate various equations in

terms of the polar and azimuthal angles for the decays of the B and the ω^o.

Table (5.6)

Legendre polynomials and D matrices

Symbol	Value
$P_2(\cos\theta)$	$1/2(3\cos^2\theta-1)$
$P_4(\cos\theta)$	$1/8(35\cos^4\theta-30\cos^2\theta+3)$
$P_6(\cos\theta)$	$1/16(231\cos^6\theta-315\cos^4\theta+105\cos^2\theta-5)$
$\text{Re } D^2_{O2}(\phi\theta\psi)=\text{Re } D^2_{O-2}(\phi\theta\psi)$	$\sqrt{6}/4(\sin^2\theta\cos2\psi)$
$2\text{Re } D^2_{OO}(\phi\theta\psi)\frac{1}{2}(3-5\cos^2\chi)$	$1/2(3\cos^2\theta-1)(3-5\cos^2\chi)$
$\text{Re } D^2_{22}(\phi\theta\psi)$	$\cos^4(\theta/2)\cos2(\phi+\psi)$ or $\left(\frac{1+\cos\theta}{2}\right)^2\cos2(\phi+\psi)$
$\text{Re } D^2_{2-2}(\phi\theta\psi)$	$\sin^4(\theta/2)\cos2(\phi-\psi)$ or $\left(\frac{1-\cos\theta}{2}\right)^2\cos2(\phi-\psi)$
$2\text{Re } D^2_{2O}(\phi\theta\psi)\frac{1}{2}(3-5\cos^2\chi)$	$(\sqrt{6}/4)\sin^2\theta\cos2\phi(3-5\cos^2\chi)$
$\text{Re } D^2_{O1}(\phi\theta\psi)d^2_{1O}(\chi)$	$(-3/2)\sin\theta\cos\theta\cos\psi\sin\chi\cos\chi$
$\text{Re } D^2_{21}(\phi\theta\psi)d^2_{1O}(\chi)$	$(\sqrt{6}/4)\sin\theta(1+\cos\theta)\sin\chi\cos(2\phi+\psi)\cos\chi$

5.8 Decay Angular Distributions for the B and the ω^o Spectra

The frames of reference are described in Section 5.4. The decay angles θ and ϕ are the polar and the azimuthal angles of the ω in the rest frame of the B and χ and ψ are the corresponding angles of the normal to the ω decay plane.

Figures (5.10) show the distributions of the B^+ decay angles $\cos\theta$ and ϕ in the t- and the s-channel helicity frames and the corresponding distributions of the sequential ω^o decay angles $\cos\chi$ and ψ in the s-channel helicity frames for the reaction:

$$B^+ \longrightarrow \pi^+\omega^o$$
$$\omega^o \longrightarrow \pi^+\pi^-\pi^o$$

for the events in the B region. Only the polar angle χ is invariant to whether the B is in the t- or the s-channel helicity frame. The distributions were obtained without the background subtraction. The curves are the fits to the distributions of Figures (5.10) of the forms given in Table (5.7). The values of the coefficients together with the fitted functions for the different distributions are listed in Table (5.7) on page 97.

5.9 Discussion of Results and Conclusions

The mass and width of the B^+ are 1235 ± 12 MeV/c^2 and 120 ± 48 MeV/c^2 respectively, and these values are in good agreement with other experiments. The total cross-section $\sigma(B^+) = 21 \pm 6$ μb. The production cross-section decreases with the incident momentum as p_{inc}^{-n} with n about 1.5. The slope of differential cross sections $d\sigma/d|t|$ and $d\sigma/d|t'|$ is about 4 GeV^{-2} which is compatible with ω^o exchange (see Section 2.7.1), although it cannot be taken as proof that the production process is not more complicated.

Text continued on page 98.

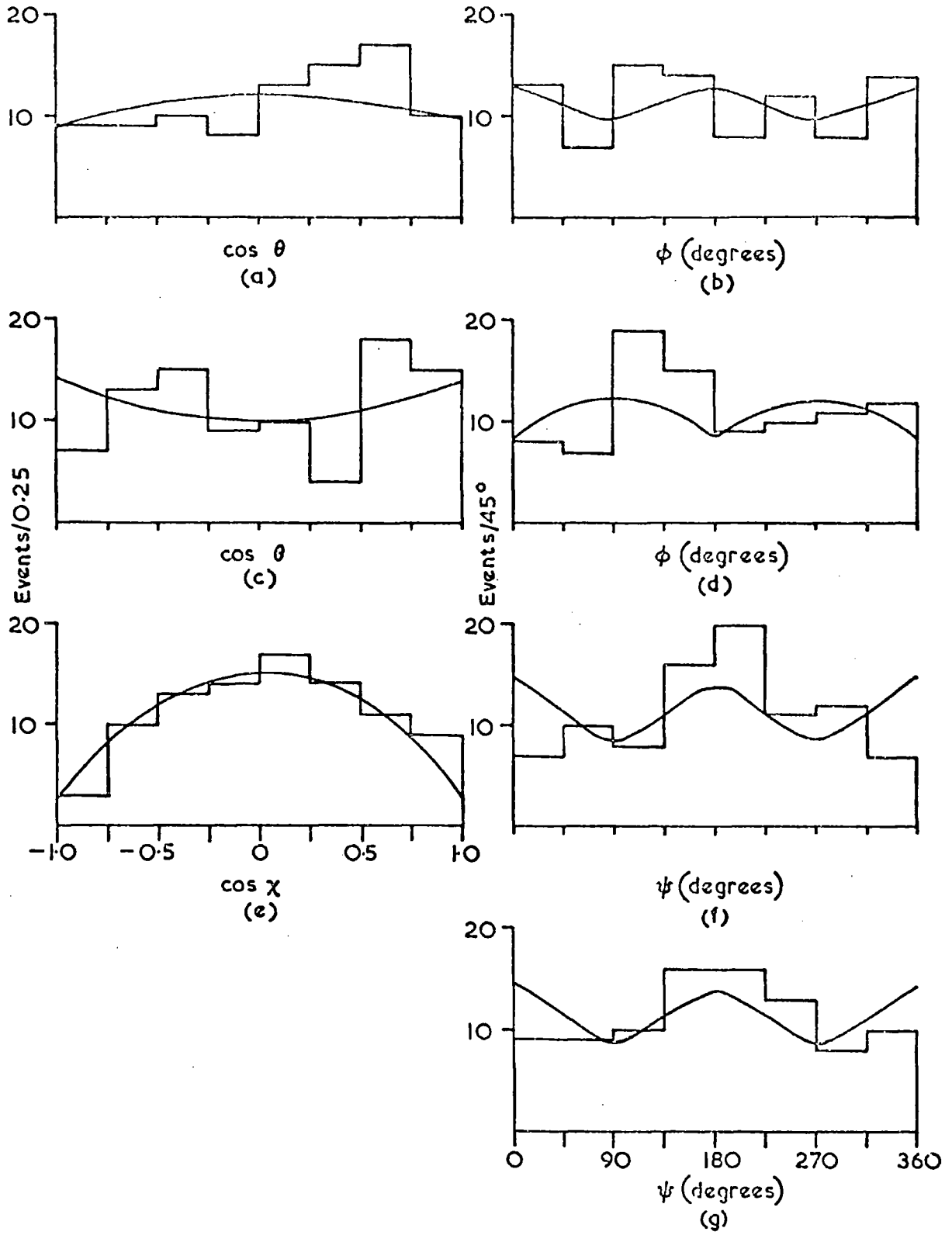

FIG.5.10 (a) DISTRIBUTION OF COSθ FOR THE B IN THE t-CHANNEL HELICITY FRAME
(b) DISTRIBUTION OF ϕ FOR THE B IN THE t-CHANNEL HELICITY FRAME
(c) DISTRIBUTION OF COSθ FOR THE B IN THE s-CHANNEL HELICITY FRAME
(d) DISTRIBUTION OF ϕ FOR THE B IN THE s-CHANNEL HELICITY FRAME
(e) DISTRIBUTION OF COSχ FOR THE ω^o IN THE s-CHANNEL HELICITY FRAME
(f) DISTRIBUTION OF ψ FOR THE ω^o IN THE s-CHANNEL HELICITY FRAME (B IN THE t-CHANNEL HELICITY FRAME)
(g) DISTRIBUTION OF ψ FOR ω^o IN THE s-CHANNEL HELICITY FRAME (B IN THE s-CHANNEL HELICITY FRAME)

THE CURVES ARE FITS TO THE DATA AS EXPLAINED IN THE TEXT—— 91 events.

Table (5.7)

Parameters of fits to the decay distributions of the B^{+} and the ω^{o} spectra

Reaction	Frame of reference	Fitted function	Coefficients		χ^2/NDF
			A	B	
$\pi^+ p \longrightarrow p B^+$	The t-channel helicity frame	$A+B\cos^2\theta$	0.22	-0.04	6/6
		$A+B\cos^2\phi$	0.55	0.11	5.9/6
	The s-channel helicity frame	$A+B\cos^2\theta$	0.16	0.06	12/6
		$A+B\cos^2\phi$	0.14	-0.02	9/6
$\pi^+ p \longrightarrow p B^+$ ↳ $\omega\pi^+$ ↳ (3π)	The s-channel helicity frame for the ω^o when B^+ in the t-channel helicity frame	$A+B\cos^2\chi^{\dagger}$	0.23	-0.17	3.3/6
		$A+B\cos^2\psi$	0. 61	0.30	10/6
	The s-channel helicity frame for the ω^o when B^+ in the s-channel helicity frame	$A+B\cos^2\chi^{\dagger}$	0.23	-0.17	3.3/6
		$A+B\cos^2\psi$	0.75	0.33	4.7/6

† These distributions are the same.

The probability for helicity zero for the ω^o from the $B^+ \longrightarrow \omega\pi^+$ decay, $|F_o|^2 = 0.09 \pm 0.07$ and therefore there is a strong dominance of helicity $\lambda = \pm 1$ states. The value of $|F_o|^2$ contradicts the prediction of a simple quark model.

The values of $\langle J_z^2 \rangle$ determined in two different ways are consistent. The possibility of $J=3$ for the B is ruled out because values of ρ_{mm} in the s-channel helicity frame are several standard deviations away from the expected values. The test of equation (5.15) giving the negative value of the ratio favours $J^P = 1^+$ or 2^+.

Assuming the assignment $J^P = 1^+$ and then from the determination of the spin density matrix elements it appears that the B^+ is weakly aligned both in the t- and the s-channel helicity frames. The modulus of the ratio $|D/S|$ amplitudes is in the range 0.2 and 1.7 for the evaluated value of $|F_o|^2 = 0.09 \pm 0.07$ within one standard deviation.

CHAPTER 6

SEARCH FOR OTHER RESONANCES

6.1 Introduction

In this Chapter the data will be discussed in terms of the possible resonances other than the Δ^{++} and the B^{+}. The first Section deals with the possibility for the higher mass Δ^{++} and it is found that their production, if it occurs, has cross sections which are too small to observe with the statistics of the present experiment. One finds no evidence for higher mass mesons decaying into $\omega\pi^{+}$ in the second Section. The next Section deals with a broad enhancement having a structure around 1860 MeV/c^2 and a smaller shoulder near 2190 MeV/c^2 in the mass distribution of M(ωp). It is concluded that these cannot be considered as resonances. Finally the results are discussed.

6.2 Higher Mass ($p\pi^{+}$) Combinations

A $p\pi^{+}$ combination can only arise from isospin 3/2 and hence any resonance belongs to the Δ series.

Figures (6.1a) and (6.1b) show the mass distributions of M($p\pi^{+}$) with M(ωp) $\leq$ 2.0 GeV/c^2 antiselected and where the decay π^{+} in the rest system of the ($p\pi^{+}$) goes backward and forward respectively with respect to the direction of flight of the ($p\pi^{+}$) system in the C.M. These two figures occupy the bands parallel to the lower and the upper right-side of the boundary on the Dalitz plot of Figure (6.2) respectively. Since Figure (6.1a) overlaps with the B^{+} in the bottom right-hand corner on the Dalitz plot of Figure (6.2), events with 1.16 GeV/c^2 < M($\omega\pi^{+}$) < 1.32 GeV/c^2 are antiselected to avoid the overlap of the B^{+} mass bands.

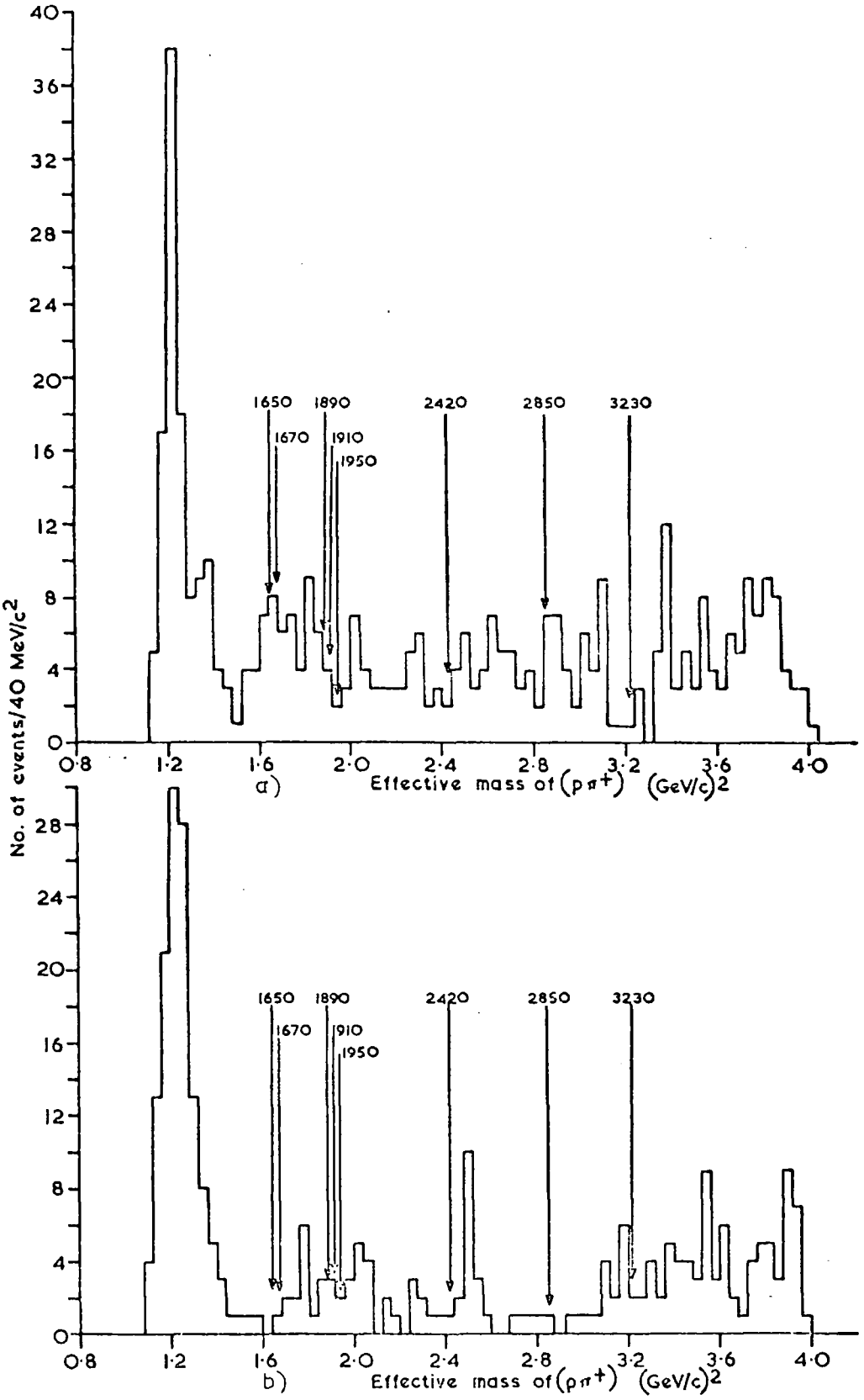

FIG. 6.1 a) $M(p\pi^+)$ WHERE THE DECAY π^+ IN THE R.S. OF $(p\pi^+)$ GOES BACKWARD ω.r.t. THE DIRECTION OF $(p\pi^+)$ IN THE C.M.S. $M(\omega p) \leq 2.0$ GeV/c² AND $1.16 < M(\omega\pi^+) < 1.32$ ARE ANTISELECTED — 404 EVENTS.

b) $M(p\pi^+)$ WHERE THE DECAY π^+ IN THE R.S. OF $(p\pi^+)$ GOES FORWARD ω.r.t. THE DIRECTION OF $(p\pi^+)$ IN THE C.M.S. $M(\omega p) \leq 2.0$ GeV/c² ANTISELECTED — 290 EVENTS.

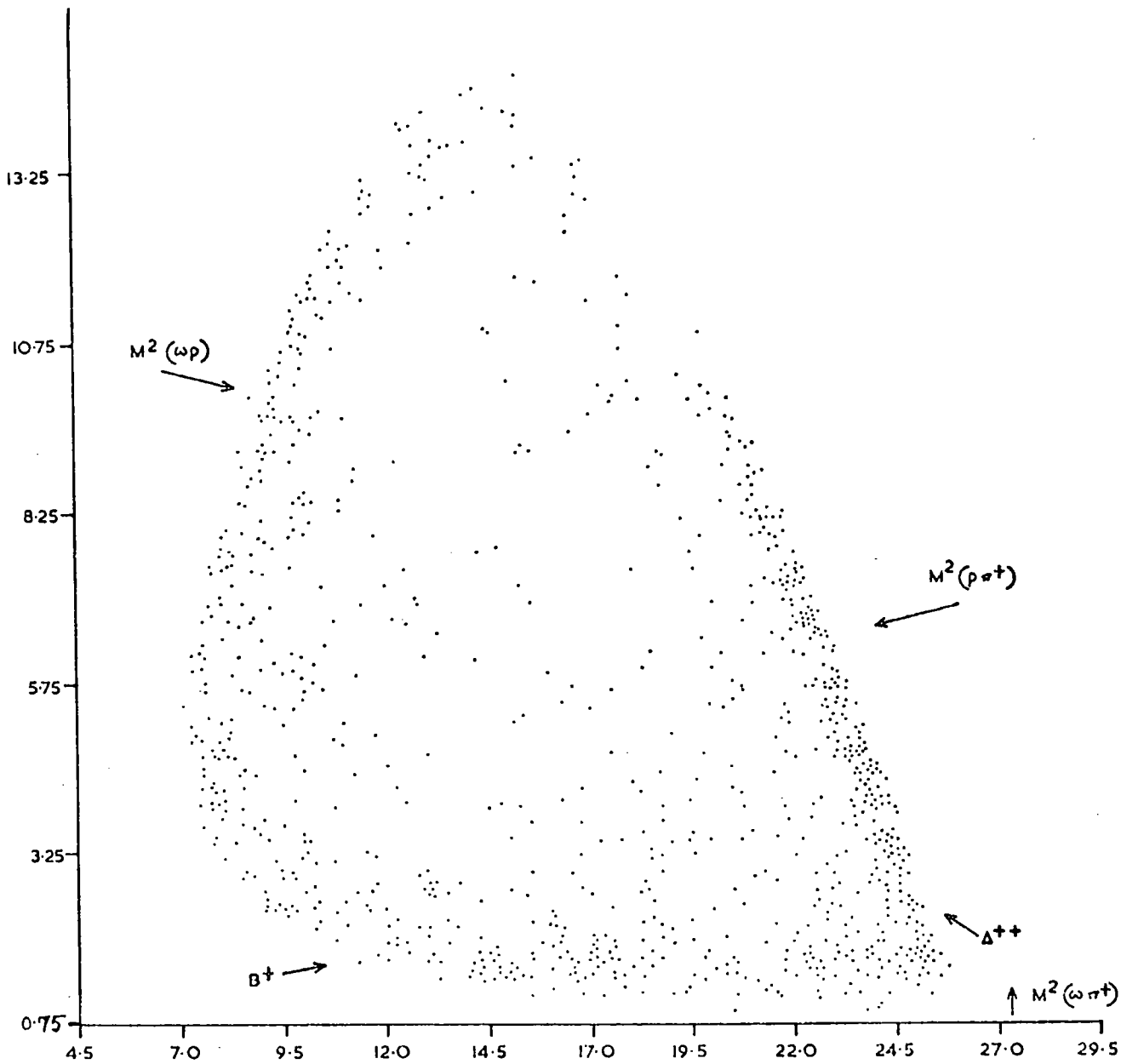

FIG. 6.2 DALITZ PLOT FOR $p\omega\pi^+$ CHANNEL (907 EVENTS).

Inspection of Figures (6.1a) and (6.1b) shows that apart from the Δ^{++} (1236), already discussed in Chapter 4, there is no structure that can be considered statistically significant. The Δ resonances are marked in the figure. In Figure (6.1a) there is some correspondence of accumulation of events with the marked regions. However, the pattern is not reinforced by Figure (6.1b), which should have identical intensities for resonances decaying symmetrically forwards backwards in their own rest systems.

If Δ resonances higher in mass than the Δ (1236) are formed, clearly their production cross sections are too small for their observation with the statistics of the present experiment.

6.3 Higher Mass $(\omega\pi^+)$ Combinations

Figures (6.3a) and (6.3b) show the mass distributions of $M(\omega\pi^+)$ with $M(\omega p) \leq 2.0$ GeV/c^2 antiselected and where the decay π^+ in the rest system of the $(\omega\pi^+)$ goes forward and backward respectively with respect to the direction of flight of the $(\omega\pi^+)$ system in the C.M. These two figures occupy the horizontal bands on the left and the right sides respectively on the Dalitz plot of Figure (6.2). Since Figure (6.3b) overlaps with the Δ^{++} in the bottom right-hand corner on the Dalitz plot of Figure (6.2), events with $M(p\pi^+) \leq 1.4$ GeV/c^2 are antiselected to avoid the overlap of the Δ^{++} mass bands.

Inspection of Figures (6.3a) and (6.3b) shows that apart from the B^+ (1235), already discussed in Chapter 5, there appears to be just background except some accumulation of events between 1.4 and 1.6 GeV/c^2 in Figure (6.3a), but the same pattern is not repeated in Figure (6.3b). Hence, there is no evidence for the higher mass mesons decaying into $\omega\pi^+$.

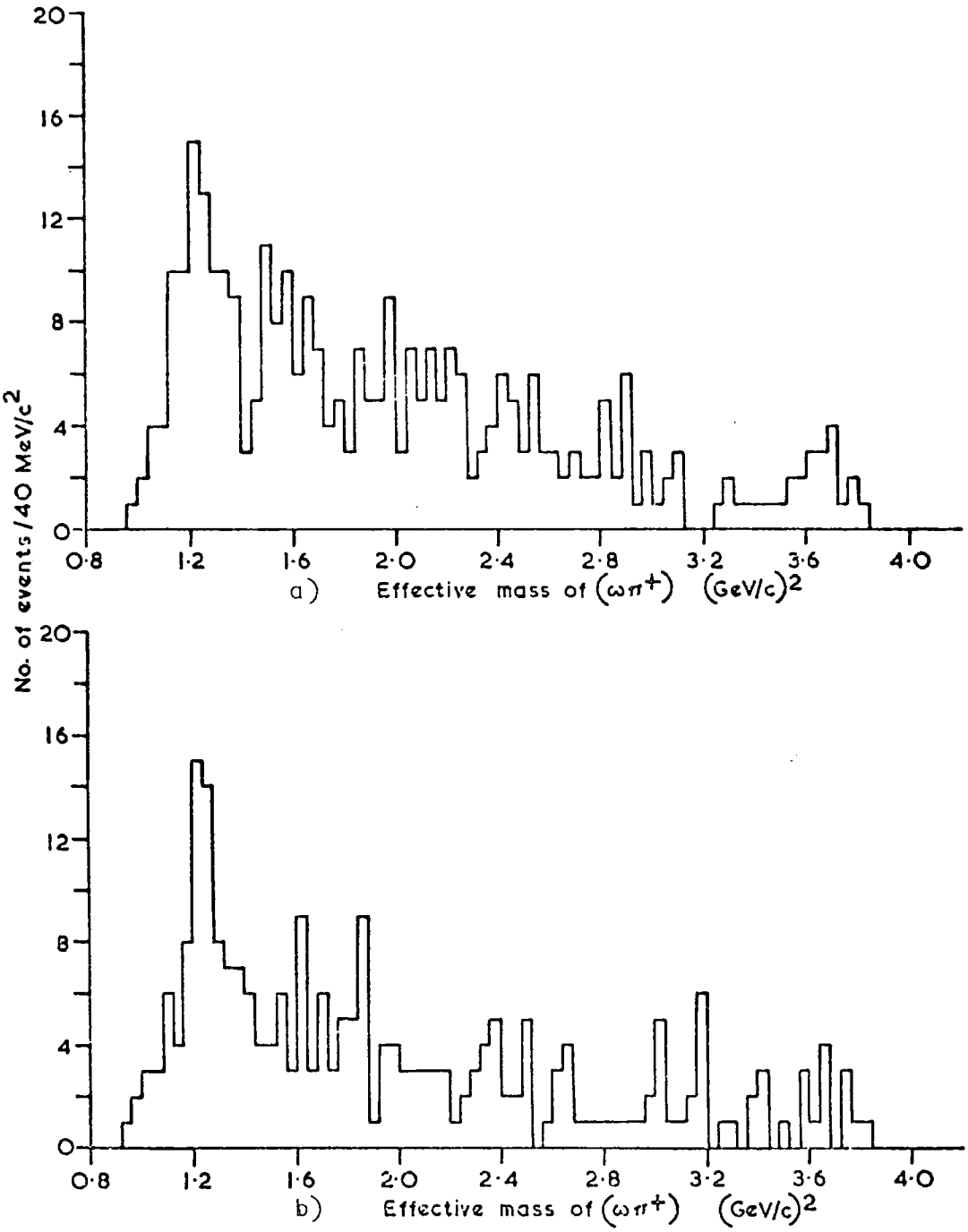

FIG. 6.3 a) $M(\omega\pi^+)$ WHERE THE DECAY π^+ IN THE R.S. OF $(\omega\pi^+)$ GOES FORWARD ω.r.t. THE DIRECTION OF $(\omega\pi^+)$ IN THE C.M.S.—318 EVENTS.

b) $M(\omega\pi^+)$ WHERE THE DECAY π^+ IN THE R.S. OF $(\omega\pi^+)$ GOES BACKWARD ω.r.t. THE DIRECTION OF $(\omega\pi^+)$ IN THE C.M.S. THE Δ^{++} ANTISELECTED — 242 EVENTS.

6.4 The (ωp) Mass Combinations

Figure (6.4) shows the mass distribution of the ωp combinations. The antiselection of the Δ^{++} (1236) and the B^{+} (1235) shows that the increase in intensity beyond 3.4 GeV/c^2 is mainly due to these resonances. There appears to be a threshold peak in Figure (6.4) around 1860 MeV/c^2 and perhaps an accumulation of events around 2190 MeV/c^2.

Figures (6.5a) and (6.5b) show the mass distributions of M(ωp) with the Δ (1236) and the B^{+} (1235) antiselected and where the decay proton in the rest system of the (ωp) goes forward and backward respectively with respect to the direction of flight of the (ωp) system in the C.M. These two figures occupy the bands parallel to the lower and the upper left-side of the boundary on the Dalitz plot of Figure (6.2).

The accumulation of events between 2100 and 2300 MeV/c^2 in Figure (6.5a) cannot be considered as a candidate for resonance because the same intensity does not show up in Figure (6.5b).

The isospin of a pω combination is 1/2. The N^* (1780) and N^* (1860) with the established $J^P = 1/2^+$ and $3/2^+$ respectively exist close to the same mass as the threshold enhancement in the ωp mass distribution. But a decay mode of $N^* \longrightarrow$ ωp has not been hitherto observed. However, if one imagines that the enhancement is produced due to any one of the N^* resonances, it can then be described by a Feynman diagram shown in Figure (6.6a). The ρ^o exchange would be consistent with both the above p-wave N^* resonances decaying into ωp. But other experiments [49,119] at lower energies do not find evidence for such a process.

However, if one assumes that the enhancement is produced by the diffractive dissociation process, it can then be described by

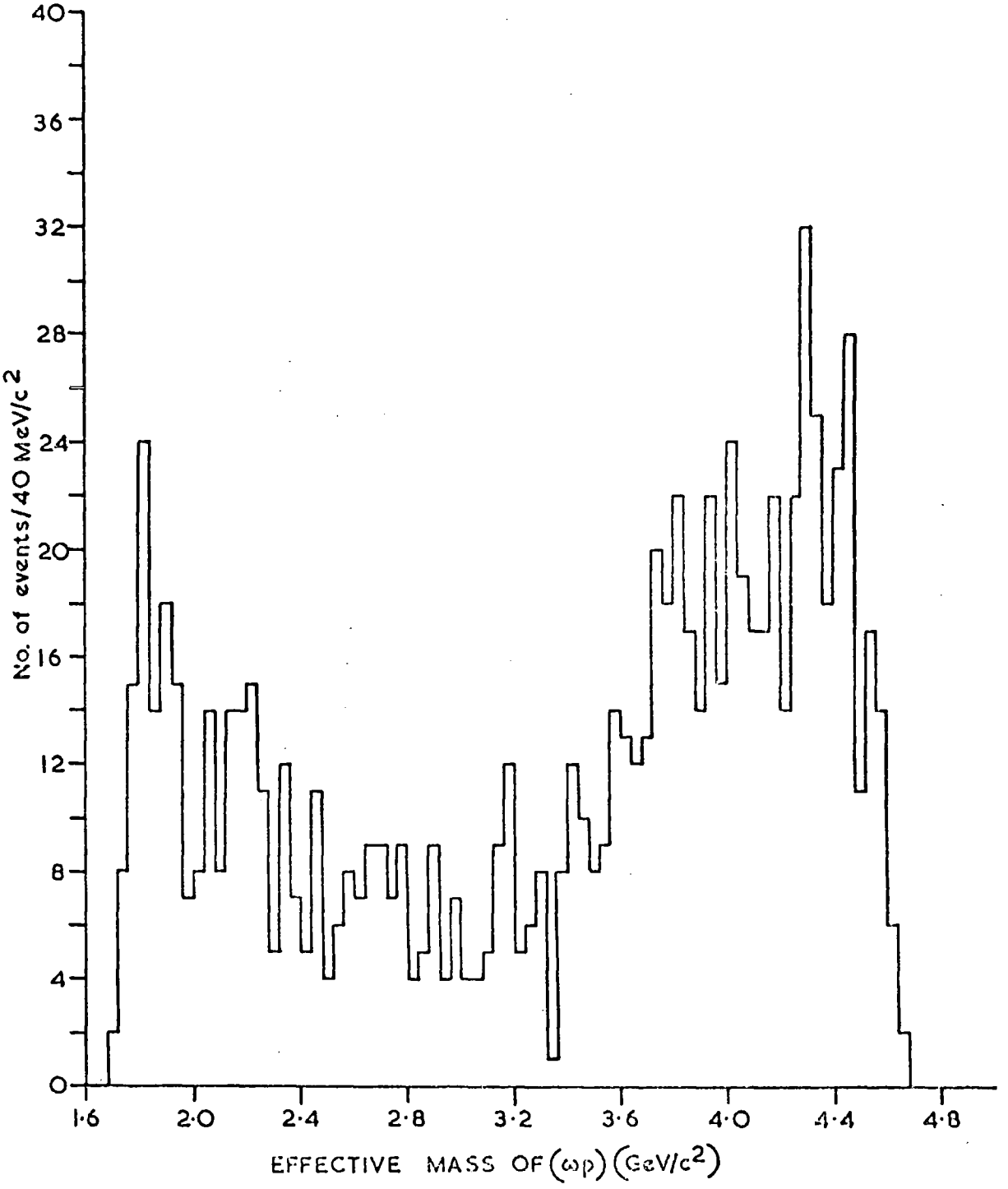

FIG. 6.4 M(ωp) —— 907 EVENTS.

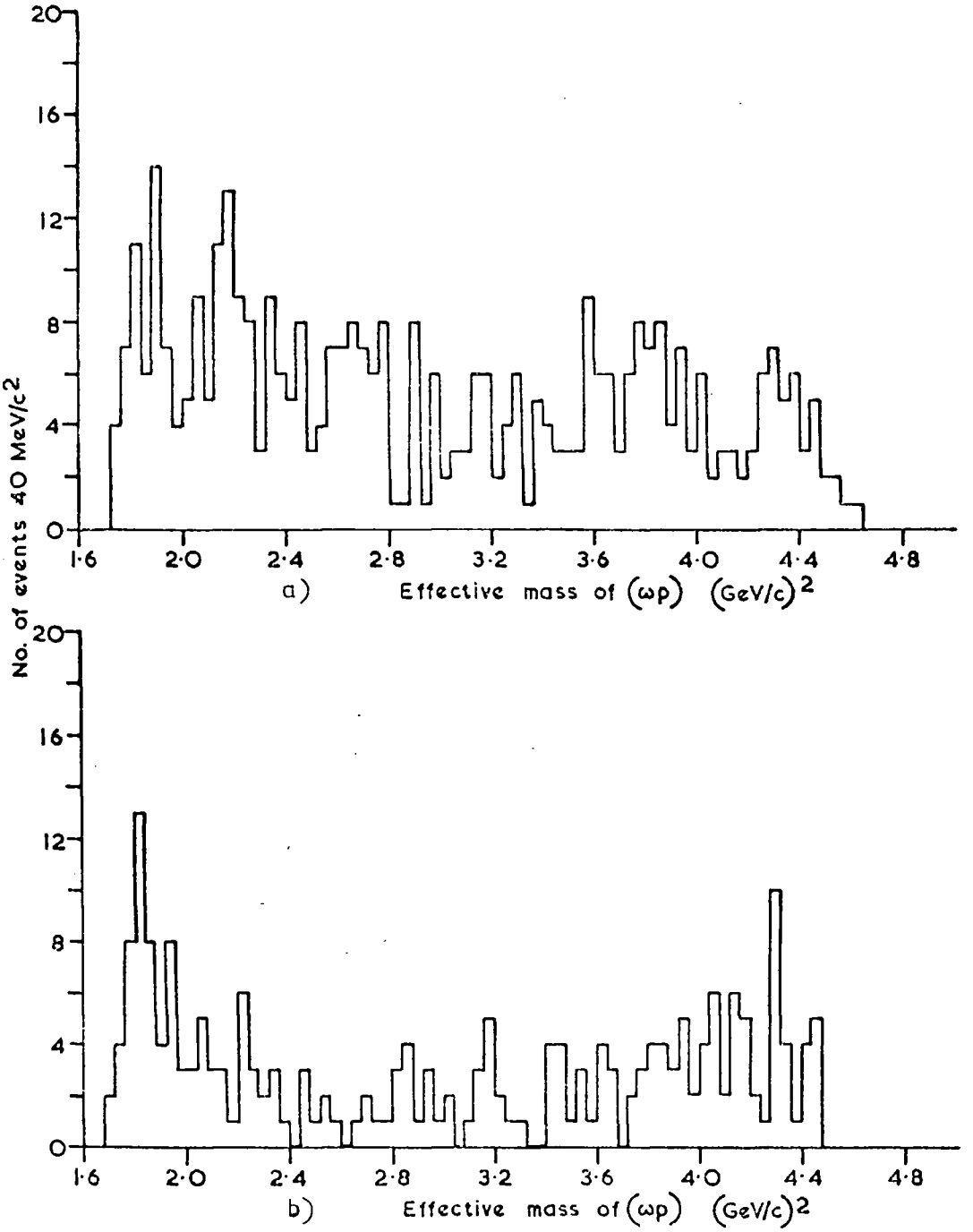

FIG. 6.5 a) M(ωp) WHERE THE DECAY PROTON IN THE R.S. OF (ωp) GOES FORWARD ω.r.t. THE DIRECTION OF(ωp) IN THE C.M.S. — 386 EVENTS.

b) M(ωp) WHERE THE DECAY PROTON IN THE R.S. OF(ωp) GOES BACKWARD ω.r.t. THE DIRECTION OF(ωp) IN THE C.M.S. — 212 EVENTS.

a diagram shown in Figure (6.6b). Here the proton p dissociates into the ω^o and a proton, then the ω^o is scattered elastically from the pion and finally the ω^o and the proton recombine to give an ωp combination.

Diffraction dissociation processes obey the empirical rule of Morrison given below [76,120]:

$$P_f = P_i (-1)^{\Delta J} , \qquad (6.1)$$

where P_f and P_i are the parities of the final state and the initial state particles and ΔJ is the difference in spin between the initial and the final state particles. This implies that the ωp should have J^P belonging to the series $1/2^+$, $3/2^-$, $5/2^+$, $7/2^-$ etc. which is incompatible with the $3/2^+$ of the N^* (1860) but could be the $1/2^+$ of the N^* (1780), if the final state produces an ωp resonance.

The structure is not likely to be due to a diffractive process, however. Aderholz et al. [49] and Satterblom et al. [119] looked at the effective mass distributions of $M(\omega p)$ in the reactions $\pi^+ p \longrightarrow p\omega\pi^+$ and $\pi^- p \longrightarrow p\omega\pi^-$ at 4 GeV/c and 2.1 GeV/c respectively. But they did not observe any structure. If this mass enhancement were produced by diffraction dissociation, they should have observed the peak since the cross sections above the threshold remain about constant with increasing beam momentum in a diffraction process [121,122]. Further, Figure (6.7) shows the differential cross-section for the reaction $\pi^+ p \longrightarrow (\omega p)\pi^+$ as a function of $|t'| = |t - t_{min}|$, where $|t|$ is the four-momentum transfer from the target proton to the (ωp), and t_{min} is the minimum value of the $|t|$. The events on which the graph is based are selected in (ωp) mass band $1.76\ \text{GeV}/c^2 < M(\omega p) < 1.96\ \text{GeV}/c^2$. The vertical error bars shown are only those due to statistics and the horizontal bars represent the

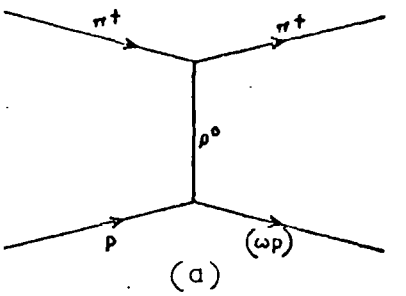

(a)

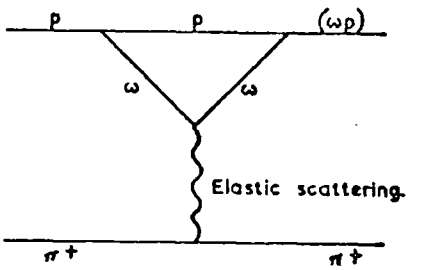

(b)

FIG. 6.6 a) FEYNMAN DIAGRAM FOR THE REACTION $\pi^+ p \rightarrow \pi^+ (\omega p)$.
b) THE DIFFRACTION DISSOCIATION PROCESS.

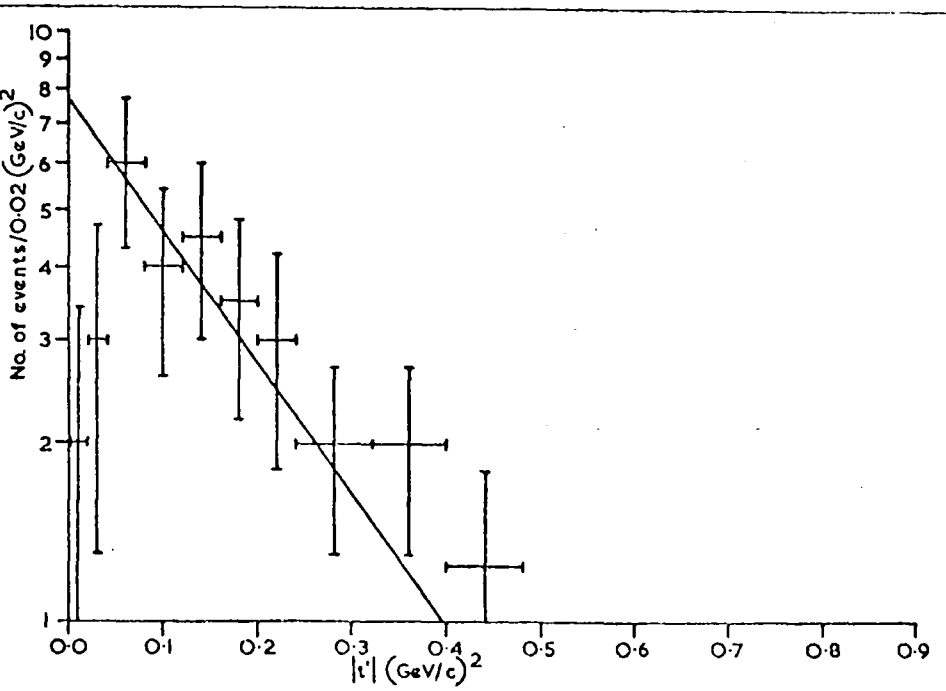

FIG. 6.7 DIFFERENTIAL CROSS-SECTION FOR $\pi^+ p \rightarrow \pi^+ (\omega p)$ AS A FUNCTION OF $|t'|$: $(dN/d|t'|)$.

interval chosen. The distribution does not show the sharp fall off with increasing $|t'|$ characteristic of a diffractive process. Indeed there is a dip at very small values of $|t'|$ and the exponential fall has an exponent at higher $|t'|$ of about 4 GeV^{-2} which is much smaller than that for diffraction scattering, more compatible with a ρ-exchange process.

Clearly with such small statistics a determination of the spin and parity of the ωp system from the data is not possible. The negative evidence for structure at lower energies does not make it easy to make a definite statement about the present data, particularly since the available phase space at lower energies might obscure possible effects. It must be remembered, however, that an enhancement of intensity at the periphery of a Dalitz plot would not be unreasonable at high energies due to the presence of high orbital angular momenta. If such angular momenta remained as high partial waves of quasi-two-body final states, the relative angular momentum between particles produced in one hemisphere (forward or backward) in the centre of mass would be small. This would inevitably lead to enhancements of intensity at low effective masses between pairs of particles in the final state. It is possible that Figures (6.4) and (6.5) merely reflect this effect.

CHAPTER 7

SUMMARY AND CONCLUSIONS

7.1 Introduction

In this Chapter summary and conclusions will be presented. The first Section deals with the total cross sections of the 4-prong $1C\pi^o$ events, the $p\omega\pi^+$ final state, the $\omega\Delta^{++}$ and the pB^+ channels. The next Section deals with the differential cross sections of the $\omega\Delta^{++}$ and the pB^+, the quasi-two-body reactions discussed in this thesis. Finally the last Section gives the decay correlations of the $\omega\Delta^{++}$ and the pB^+ channels.

7.2 Total Cross Sections

It is possible to determine an absolute total cross-section with a bubble chamber experiment. But it was decided that the present experiment would not be used to determine an absolute cross-section but that the counter measurements would be used to determine the cross-section equivalent of the scanned events.

One event for 4-prong DST = 0.17 μb.

The total cross sections for 4-prong $1C\pi^o$ events $\sigma(\pi^+p \longrightarrow p\pi^+\pi^+\pi^-\pi^o)$ and for the $p\omega\pi^+$ final state $\sigma(\pi^+p \longrightarrow p\omega\pi^+)$ respectively are 1.31 ± 0.13 mb and 0.134 ± 0.013 mb. These cross sections when compared with those published at different energies gave slopes of 0.82 and 1.41 respectively. These values are in good agreement with those obtained by other workers.

For the double resonance production of the $\omega\Delta^{++}$, fitting of mass distribution of $M(p\pi^+)$ with a p-wave relativistic Breit-Wigner function gave values of mass and width of the Δ^{++} as 1234 ± 8 MeV/c^2 and 122 ± 32 MeV/c^2 respectively. These values are in good agreement

with those obtained by other workers.

After making all the necessary corrections, the $\omega\Delta^{++}$ cross-section $\sigma(\pi^+p \longrightarrow \omega\Delta^{++})$ is 53 ± 10 μb. This cross-section when compared with those published for different energies gave a slope of 1.85 which is in good agreement with those obtained by other workers for non-strange meson exchange reactions.

For the reaction $\pi^+p \longrightarrow pB^+$, fitting of mass distribution of $M(\omega\pi^+)$ with an s-wave relativistic Breit-Wigner function gave values of mass and width of the B^+ as 1235 ± 12 MeV/c^2 and 120 ± 48 MeV/c^2 respectively. These values are in good agreement with those obtained by other workers.

After making all the necessary corrections, the pB^+ cross-section $\sigma(\pi^+p \longrightarrow pB^+)$ is 21 ± 6 μb. This cross-section when compared with those published for different energies gave a rough estimate of slope of 1.5.

Thus at 11.7 GeV/c the $p\omega\pi^+$ final state from π^+p collisions represents 0.93% of the inelastic cross-section of 14.395 mb. About 40% of this final state consists of an $\omega^o\Delta^{++}$ and 16% of a pB^+. A further 10% has a concentration of ωp mass in a region 1.76 to 1.96 GeV/c^2. This leaves about 34% of the $p\omega\pi^+$ final state which is not compatible with any quasi-two-body process, there being no evidence of the presence of higher mass Δ^{++} or higher mass $\omega^o\pi^+$ resonances. This fraction is too high to be reasonably accounted for by background which has been erroneously interpreted as the ω^o mesons and seems to represent a genuine signal of non-quasi-two-body final states. The percentage of such states increases to 44% if it is assumed that the ωp enhancement is only a kinematical effect of high orbital angular momentum.

7.3 Differential Cross Sections

For the reaction $\pi^+ p \longrightarrow \omega\Delta^{++}$, $d\sigma/d|t|$ and $d\sigma/d|t'|$ show dips as $|t|$ (or $|t'|$) $\longrightarrow$ 0. Dips also appear in these distributions near $|t|$ (or $|t'|$) ~ 0.6 $(GeV/c)^2$. The exponential fall off of the differential cross sections with increasing $|t|$ (or $|t'|$) above the region $|t|$ (or $|t'|$) ~ 0.2 $(GeV/c)^2$ has an exponent of ≈ 4 GeV^{-2}. The values of the exponents as obtained by different workers for this reaction remain fairly constant over a large range of energy. This shows there is no energy dependence on the value of the exponent. However the exponential shape of the differential cross sections does not depend only on the ρ propagator.

For the reaction $\pi^+ p \longrightarrow pB^+$, dips or breaks in $d\sigma/d|t|$ or $d\sigma/d|t'|$ distributions are not clear due to limited statistics. The exponential fall off of the differential cross sections with increasing $|t|$ (or $|t'|$) has an exponent of ≈ 4 GeV^{-2}. The values of the exponents as obtained by different workers at different energies for this reaction are too limited to establish any energy dependence.

7.4 The Decay Correlations

For the $\omega\Delta^{++}$ channel, the prediction of the ρ-exchange or those of the pure Regge pole model on the density matrix elements do not agree with the present experimental results. The value of ρ_{00} in the $|t|$ interval 0.2 to 0.3 $(GeV/c)^2$ for s-channel helicity frame is negative by two standard deviations. This is most likely a statistical fluctuation. The values of ρ_{11} and ρ_{1-1} in the t-channel helicity frame for $|t| = 0.6$ $(GeV/c)^2$ are unequal and have opposite signs which is not consistent with a ρ + B Regge pole model. There are dips at $|t| \approx 0$ and $|t| \approx 0.5$ $(GeV/c)^2$ for

$\sigma_1^+ = \rho_{11} + \rho_{1-1}$ in the t-channel helicity frame. Another dip in the value of $\sigma_1^- = \rho_{11} - \rho_{1-1}$ at $|t| \approx 0.2$ $(GeV/c)^2$ appears as expected according to the Regge pole model calculations. Values of most of the double statistical tensors in the t- and the s-channel helicity and the t- and the s-channel transversity frames are compatible with zero. Thus the agreement with the predicted values of these tensors is not too good.

For the reaction $\pi^+ p \longrightarrow p B^+$, the value of the helicity amplitude of the ω^o from the sequential decay of the B^+, $|F_o|^2 = 0.09 \pm 0.07$ which shows a strong dominance of the helicity $\lambda = \pm 1$ states. This value of $|F_o|^2$ disagrees with the prediction of a simple quark model. The values of $\langle J_z^2 \rangle$ as determined by two different methods are consistent. The possibility of $J = 3$ for the B is ruled out because values of ρ_{mm} in the s-channel helicity frame are several standard deviations away from the expected values. However, evidence favouring $J^P = 1^+$ or 2^+ assignment is obtained from the values of $\langle J_z^2 \rangle$. The determination of the spin density matrix elements for $J^P = 1^+$ assignment shows that the B^+ is weakly aligned both in the t- and the s-channel helicity frames. The $|D/S|$ ratio is in the range 0.2 and 1.7 for the value of $|F_o|^2 = 0.09 \pm 0.07$ within one standard deviation.

APPENDIX A

COMPARISON OF PRESENT ANALYSIS WITH THAT PUBLISHED

In this Appendix the comparative tables of the results of the present analysis with those published on the same data [3] for the $\omega\Delta^{++}$ channel will be presented. The main results of interest are the total channel cross-section and the spin density matrix elements. The differences, although present, are never large enough to consider either determination of a quantity to be erroneous. On the other hand, it illustrates the variation that occurs when two different but equally reasonable schemes of analysis are applied to the raw data. The results are summarised in Tables (A.1), (A.2) and (A.3).

Table (A.1)

Total cross-section

Reaction	Reference	$\sigma(\omega\Delta^{++})$ μb
$\pi^+ p \longrightarrow \omega\Delta^{++}$	[3]	61 ± 12
	Thesis	53 ± 10

Table (A.2)

Spin density matrix elements for the $\omega\Delta^{++}$ in the t-channel helicity frame

Quantity	$\lvert t \rvert$ (GeV/c)^2 / Ref.	0.0-0.1	0.1-0.2	0.2-0.3	0.3-0.4	0.4-0.6	0.6-1.0
ρ_{00}	[3]	.40±.13	.30±.09	.29±.12	.18±.11	.12±.12	.43±.17
	Thesis	.55±.15	.25±.10	.25±.13	.13±.11	.18±.13	.45±.18
Re ρ_{10}	[3]	-.10±.05	-.09±.05	.00±.05	-.05±.06	-.15±.08	-.10±.09
	Thesis	-.11±.06	-.13±.06	.06±.06	-.04±.06	-.15±.09	-.10±.10
ρ_{1-1}	[3]	.34±.08	.14±.08	.47±.08	.25±.10	-.02±.15	.05±.13
	Thesis	.37±.08	.15±.09	.51±.08	.26±.10	-.11±.16	-.04±.12
ρ_{33}	[3]	.06±.09	.24±.07	.13±.08	.32±.09	.25±.11	.23±.12
	Thesis	.11±.11	.25±.07	.14±.10	.34±.09	.23±.12	.19±.12
Re ρ_{31}	[3]	-.13±.07	-.17±.07	.07±.08	-.12±.07	-.17±.11	-.23±.12
	Thesis	-.14±.09	-.08±.07	.11±.09	-.11±.07	-.20±.12	-.25±.13
Re ρ_{3-1}	[3]	.03±.07	-.02±.07	.02±.08	.16±.08	-.15±.10	.11±.12
	Thesis	-.01±.08	.01±.08	.05±.08	.19±.08	-.18±.11	.07±.12

Table (A.3)

Spin density matrix elements for the $\omega\Delta^{++}$ in the s-channel helicity frame

Quantity	$\|t\|$ $(GeV/c)^2$ / Ref.	0.0-0.1	0.1-0.2	0.2-0.3	0.3-0.4	0.4-0.6	0.6-1.0
ρ_{00}	[3]	.40±.12	.35±.10	-.07±.07	.20±.10	.41±.17	.17±.14
	Thesis	.54±.14	.40±.11	-.13±.07	.19±.10	.58±.18	.29±.15
Re ρ_{10}	[3]	.09±.06	.06±.05	.08±.07	.06±.06	.18±.08	.04±.11
	Thesis	.15±.06	.02±.05	.08±.06	.02±.07	.12±.09	.10±.10
ρ_{1-1}	[3]	.34±.08	.17±.07	.29±.11	.26±.10	.14±.12	-.08±.14
	Thesis	.36±.09	.22±.08	.32±.12	.30±.10	.09±.12	-.12±.14
ρ_{33}	[3]	.04±.09	.10±.08	.32±.08	.25±.08	.02±.12	.20±.12
	Thesis	.08±.10	.22±.08	.38±.08	.34±.08	.05±.13	.35±.10
Re ρ_{31}	[3]	.09±.09	.01±.06	.08±.08	.08±.08	.04±.11	.19±.12
	Thesis	.09±.11	.04±.07	.00±.09	.10±.08	.18±.11	.22±.13
Re ρ_{3-1}	[3]	.04±.06	.05±.06	-.09±.08	.20±.07	-.02±.09	.13±.12
	Thesis	.01±.07	.02±.07	-.09±.09	.19±.09	-.07±.10	-.02±.14

APPENDIX B

THE JOINT DECAY CORRELATIONS

In this Appendix the joint decay correlations for the reaction $\pi^+ p \longrightarrow \omega\Delta^{++}$ in the t- and the s-channel helicity frames and in the t- and the s-channel transversity frames will be derived. For a production process, the number of statistical tensors depends on $J_i \leq 2\, s_i$, $|M_i| \leq J_i$ after taking into account the symmetry properties of the tensors. These properties are summarised in Table (B.1). [84].

Table (B.1)

Symmetry properties of the statistical tensors

	Helicity axes	Transversity axes
Hermiticity of the density matrix	$(T^{J_1J_2}_{M_1M_2})^* = (-1)^{M_1+M_2}\, T^{J_1J_2}_{-M_1,-M_2}$	
Parity conservation in the production process (unpolarized target)	Real for J_1+J_2 even Pure imag. for J_1+J_2 odd	$M_1 + M_2$ even $T^{J_1J_2}_{M_1M_2}=0$ for M_1+M_2 odd
Parity conservation in the decay of resonance i	J_i even $F_i(J_i) = 0$ for J_i odd	

Now in the $\omega\Delta^{++}$ channel the spins of the resonances are: $s(\omega)=1$, $s(\Delta^{++}) = 3/2$. Therefore, $J_1 \leq 2$; $J_2 \leq 3$; $M_1 \leq 2$ and $M_2 \leq 3$.

B.1 The Joint Decay Correlations in the t- or the s-Channel Helicity Frame

Only J_i even is allowed due to parity conservation in the decay of resonance i and (J_1+J_2) should be even for the real values of $T^{J_1J_2}_{M_2M_2}$ due to parity conservation in the production process (see Table (B.1).

Expansion of equation (4.13) gives:

$$
\begin{aligned}
W(\cos\chi,\psi;\cos\theta,\phi) = {} & F_1(0)F_2(0)\, T^{00}_{00}\, Y^{0*}_0(1)\, Y^{0*}_0(2) + \\
& F_1(2)F_2(0)\Big\{T^{20}_{10}\, Y^{1*}_2(1)\, Y^{0*}_0(2) + T^{20}_{-10} Y^{-1*}_2(1) Y^{0*}_0(2) + \\
& \quad T^{20}_{20}\, Y^{2*}_2(1)\, Y^{0*}_0(2) + T^{20}_{-20} Y^{-2*}_2(1) Y^{0*}_0(2) + \\
& \quad T^{20}_{00}\, Y^{0*}_2(1)\, Y^{0*}_0(2)\Big\} + \\
& F_1(0)F_2(2)\Big\{T^{02}_{01}\, Y^{0*}_0(1)\, Y^{1*}_2(2) + T^{02}_{0-1} Y^{0*}_0(1) Y^{-1*}_2(2) + \\
& \quad T^{02}_{02}\, Y^{0*}_0(1)\, Y^{2*}_2(2) + T^{02}_{0-2} Y^{0*}_0(1) Y^{-2*}_2(2) + \\
& \quad T^{02}_{00}\, Y^{0*}_0(1)\, Y^{0*}_2(2)\Big\} + \\
& F_1(2)F_2(2)\Big\{T^{22}_{22}\, Y^{2*}_2(1)\, Y^{2*}_2(2) + T^{22}_{-2-2} Y^{-2*}_2(1) Y^{-2*}_2(2) + \\
& \quad T^{22}_{12}\, Y^{1*}_2(1)\, Y^{2*}_2(2) + T^{22}_{-1-2} Y^{-1*}_2(1) Y^{-2*}_2(2) + \\
& \quad T^{22}_{02}\, Y^{0*}_2(1)\, Y^{2*}_2(2) + T^{22}_{0-2} Y^{0*}_2(1) Y^{-2*}_2(2) + \\
& \quad T^{22}_{1-2} Y^{1*}_2(1)\, Y^{-2*}_2(2) + T^{22}_{-12} Y^{-1*}_2(1) Y^{2*}_2(2) + \\
& \quad T^{22}_{2-2} Y^{2*}_2(1)\, Y^{-2*}_2(2) + T^{22}_{-22} Y^{-2*}_2(1) Y^{2*}_2(2) + \\
& \quad T^{22}_{21}\, Y^{2*}_2(1)\, Y^{1*}_2(2) + T^{22}_{-2-1} Y^{-2*}_2(1) Y^{-1*}_2(2) + \\
& \quad T^{22}_{20}\, Y^{2*}_2(1)\, Y^{0*}_2(2) + T^{22}_{-20} Y^{-2*}_2(1) Y^{0*}_2(2) + \\
& \quad T^{22}_{2-1} Y^{2*}_2(1)\, Y^{-1*}_2(2) + T^{22}_{-21} Y^{-2*}_2(1) Y^{1*}_2(2) + \\
& \quad T^{22}_{11}\, Y^{1*}_2(1)\, Y^{1*}_2(2) + T^{22}_{-1-1} Y^{-1*}_2(1) Y^{-1*}_2(2) + \\
& \quad T^{22}_{01}\, Y^{0*}_2(1)\, Y^{1*}_2(2) + T^{22}_{0-1} Y^{-1*}_2(1) Y^{1*}_2(2) + \\
& \quad T^{22}_{1-1} Y^{1*}_2(1)\, Y^{-1*}_2(2) + T^{22}_{-11} Y^{-1*}_2(1) Y^{1*}_2(2) + \\
& \quad T^{22}_{10}\, Y^{1*}_2(1)\, Y^{0*}_2(2) + T^{22}_{-10} Y^{-1*}_2(1) Y^{0*}_2(2) + \\
& \quad T^{22}_{00}\, Y^{0*}_2(1)\, Y^{0*}_2(2)\Big\}.
\end{aligned}
\tag{B.1}
$$

B.2 The Joint Decay Correlations in the t- or the s-Channel Transversity Frame

Only J_i even is allowed due to parity conservation in the decay of resonance i and (M_1+M_2) should be even due to parity conservation in the production process. Due to hermiticity condition:

$(T^{J_1J_2}_{M_1M_2})^* = T^{J_1J_2}_{0\,0}$, if $M_1 = M_2 = 0$ and hence $T^{J_1J_2}_{0\,0}$ will be real (see Table (B.1)). Hence one gets four real and eight complex statistical tensors for the transversity axes.

Expansion of equation (4.13) gives:

$$
\begin{aligned}
W(\cos\chi,\psi;\cos\theta,\phi) = {} & F_1(0)F_2(0)\; T^{00}_{00} Y^{0*}_0(1) Y^{0*}_0(2) + \\
& F_1(2)F_2(0)\left\{T^{20}_{20} Y^{2*}_2(1) Y^{0*}_0(2) + T^{20}_{-20} Y^{-2*}_2(1) Y^{0*}_0(2) + T^{20}_{00} Y^{0*}_2(1)\, Y^{0*}_0(2)\right\} \\
& + F_1(0)F_2(2)\left\{T^{02}_{02} Y^{0*}_0(1) Y^{2*}_2(2) + T^{02}_{0-2} Y^{0*}_0(1) Y^{-2*}_2(2) + T^{02}_{00} Y^{0*}_0(1)\, Y^{0*}_2(2)\right\} \\
& + F_1(2)F_2(2)\Big\{T^{22}_{22} Y^{2*}_2(1) Y^{2*}_2(2) + T^{22}_{-2-2} Y^{-2*}_2(1) Y^{-2*}_2(2) + T^{22}_{2-2} Y^{2*}_2(1)\, Y^{-2*}_2(2) \\
& \quad + T^{22}_{-22} Y^{-2*}_2(1) Y^{2*}_2(2) + T^{22}_{11} Y^{1*}_2(1) Y^{1*}_2(2) + T^{22}_{-1-1} Y^{-1*}_2(1)\, Y^{-1*}_2(2) \\
& \quad + T^{22}_{1-1} Y^{1*}_2(1) Y^{-1*}_2(2) + T^{22}_{-11} Y^{-1*}_2(1) Y^{1*}_2(2) + T^{22}_{00} Y^{0*}_2(1) Y^{0*}_2(2) \\
& \quad + T^{22}_{02} Y^{0*}_2(1) Y^{2*}_2(2) + T^{22}_{0-2} Y^{0*}_2(1) Y^{-2*}_2(2) \\
& \quad + T^{22}_{20} Y^{2*}_2(1) Y^{0*}_2(2) + T^{22}_{-20} Y^{-2*}_2(1) Y^{0*}_2(2)\Big\}
\end{aligned}
\qquad \ldots\ldots(B.4)
$$

Using equation (B.2) for the values of constants, applying the hermiticity condition as given in Table (B.1) and using the condition:

$$
T^{J_1J_2}_{M_1M_2}\, Y^{M_1*}_{J_1}(1)\, Y^{M_2*}_{J_2}(2) + T^{J_1J_2*}_{M_1M_2}\, Y^{M_1}_{J_1}(1)\, Y^{M_2}_{J_2}(2) =
$$

$$
2\,\mathrm{Re}\, T^{J_1J_2}_{M_1M_2}\left(\mathrm{Re}\, Y^{M_1}_{J_1}(1)\, \mathrm{Re} Y^{M_2}_{J_2}(2) - \mathrm{Im}\, Y^{M_1}_{J_1}(1)\, \mathrm{Im}\, Y^{M_2}_{J_2}(2)\right) +
$$

$$
2\,\mathrm{Im}\, T^{J_1J_2}_{M_1M_2}\left(\mathrm{Re}\, Y^{M_1}_{J_1}(1)\, \mathrm{Im}\, Y^{M_2}_{J_2}(2) + \mathrm{Im}\, Y^{M_1}_{J_1}(1)\, \mathrm{Re}\, Y^{M_2}_{J_2}(2)\right)
$$

for the complex statistical tensors, equation (B.4) becomes:

$$W(\cos\chi,\psi;\cos\theta,\phi)= \frac{1}{16\pi^2} - \sqrt{\frac{3}{10\pi^2}}\{2(\mathrm{ReT}^{20}_{20}\mathrm{ReY}^2_2(1)Y^O_O(2)+\mathrm{ImT}^{20}_{20}\mathrm{ImY}^2_2(1)Y^O_O(2))$$

$$+T^{20}_{20}Y^O_2(1)Y^O_O(2)\}$$

$$-\sqrt{\frac{3}{20\pi^2}}\{2(\mathrm{ReT}^{O2}_{O2}Y^O_O(1)\mathrm{ReY}^2_2(2)+\mathrm{ImT}^{O2}_{O2}Y^O_O(1)\mathrm{ImY}^2_2(2))$$

$$+T^{O2}_{OO}Y^O_O(1)Y^O_2(2)\}$$

$$+\sqrt{\frac{3}{50\pi^2}}\{2\mathrm{ReT}^{22}_{22}(\mathrm{ReY}^2_2(1)\mathrm{ReY}^2_2(2)-\mathrm{ImY}^2_2(1)\mathrm{ImY}^2_2(2))$$

$$+2\mathrm{ImT}^{22}_{22}(\mathrm{ReY}^2_2(1)\mathrm{ImY}^2_2(2)+\mathrm{ImY}^2_2(1)\mathrm{ReY}^2_2(2))$$

$$+2\mathrm{ReT}^{22}_{2-2}(\mathrm{ReY}^2_2(1)\mathrm{ReY}^{-2}_2(2)-\mathrm{ImY}^2_2(1)\mathrm{ImY}^{-2}_2(2))$$

$$+2\mathrm{ImT}^{22}_{2-2}(\mathrm{ReY}^2_2(1)\mathrm{ImY}^{-2}_2(2)+\mathrm{ImY}^2_2(1)\mathrm{ReY}^{-2}_2(2))$$

$$+2\mathrm{ReT}^{22}_{11}(\mathrm{ReY}^1_2(1)\mathrm{ReY}^1_2(2)-\mathrm{ImY}^1_2(1)\mathrm{ImY}^1_2(2))$$

$$+2\mathrm{ImT}^{22}_{11}(\mathrm{ReY}^1_2(1)\mathrm{ImY}^1_2(2)+\mathrm{ImY}^1_2(1)\mathrm{ReY}^1_2(2))$$

$$+2\mathrm{ReT}^{22}_{1-1}(\mathrm{ReY}^1_2(1)\mathrm{ReY}^{-1}_2(2)-\mathrm{ImY}^1_2(1)\mathrm{ImY}^{-1}_2(2))$$

$$+2\mathrm{ImT}^{22}_{1-1}(\mathrm{ReY}^1_2(1)\mathrm{ImY}^{-1}_2(2)+\mathrm{ImY}^1_2(1)\mathrm{ReY}^{-1}_2(2))$$

$$+T^{22}_{OO}Y^O_2(1)Y^O_2(2)$$

$$+2(\mathrm{ReT}^{22}_{O2}Y^O_2(1)\mathrm{ReY}^2_2(2)+\mathrm{ImT}^{22}_{O2}Y^O_2(1)\mathrm{ImY}^2_2(2))$$

$$+2(\mathrm{ReT}^{22}_{20}\mathrm{ReY}^2_2(1)Y^O_2(2)+\mathrm{ImT}^{22}_{20}\mathrm{ImY}^2_2(1)Y^O_2(2))\}$$

.....(B.5)

Substituting the values of $Y^{M_1}_{J_1}(1)$ and $Y^{M_2}_{J_2}(2)$ in equation (B.5) and after simplification and rearrangement of terms, one gets equation (4.15).

APPENDIX C

THE ρ_{mm}, DECAY ANGULAR DISTRIBUTION FOR $J^P=1^+$ AND $|D/S|$ RATIO FOR THE B

In this Appendix the diagonal elements of the density matrix for different J assignments, the decay angular distribution for $J^P=1^+$ assignment and the $|D/S|$ Ratio for the B meson will be derived.

C.1 The Diagonal Elements of the Density Matrix for the B

Expansion of equation (5.10) for J=1 gives:

$$W(\cos\theta)= \frac{3}{2}\Bigg[\Bigg\{ \sum_{L=0} \sum_{\lambda,m} (-1)^{m-\lambda} \rho_{mm} |F_\lambda|^2 \, C(JJO, -mm) \cdot C(JJO, -\lambda\lambda) \, P_o(\cos\theta) \Bigg\} + \Bigg\{ \sum_{L=1} \sum_{\lambda,m} (-1)^{m-\lambda} \rho_{mm} |F_\lambda|^2 \, C(JJ1, -mm) \cdot C(JJ1, -\lambda\lambda) \, P_1(\cos\theta) \Bigg\} + \Bigg\{ \sum_{L=2} \sum_{\lambda,m} (-1)^{m-\lambda} \rho_{mm} |F_\lambda|^2 \, C(JJ2, -mm) \cdot C(JJ2, -\lambda\lambda) \, P_2(\cos\theta) \Bigg\} \Bigg] . \tag{C.1}$$

$$\begin{aligned} W(\cos\theta)= \frac{3}{2}\Bigg[& P_o(\cos\theta) \Bigg\{ \sum_m (-1)^{m+1} \rho_{mm} |F_{-1}|^2 \, C(JJO,-mm) \, C(JJO, 1, -1) \\ & + \sum_m (-1)^m \rho_{mm} |F_o|^2 \, C(JJO,-mm) \, C(JJO, O, O) \\ & + \sum_m (-1)^{m-1} \rho_{mm} |F_1|^2 \, C(JJO,-mm) \, C(JJO, -1, 1) \Bigg\} \\ & + P_1(\cos\theta) \Bigg\{ \sum_m (-1)^{m+1} \rho_{mm} |F_{-1}|^2 \, C(JJ1,-mm) \, C(JJ1, 1, -1) \\ & + \sum_m (-1)^m \rho_{mm} |F_o|^2 \, C(JJ1,-mm) \, C(JJ1, O, O) \\ & + \sum_m (-1)^{m-1} \rho_{mm} |F_1|^2 \, C(JJ1,-mm) \, C(JJ1, -1, 1) \Bigg\} \\ & + P_2(\cos\theta) \Bigg\{ \sum_m (-1)^{m+1} \rho_{mm} |F_{-1}|^2 \, C(JJ2,-mm) \, C(JJ2, 1, -1) \\ & + \sum_m (-1)^m \rho_{mm} |F_o|^2 \, C(JJ2,-mm) \, C(JJ2, O, O) \\ & + \sum_m (-1)^{m-1} \rho_{mm} |F_1|^2 \, C(JJ2,-mm) \, C(JJ2, -1, 1) \Bigg\} \Bigg] \end{aligned} \tag{C.2}$$

Summing over m = 0, ±1, one gets 27 terms and substituting the values of Clebsch-Gordan coefficients and the normalizations $\sum_{\lambda} |F_\lambda|^2 = 1$ and $\sum_{m=-1}^{m=1} \rho_{mm} = 1$ in equation (C.2) gives:

$$W(\cos\theta) = \frac{1}{2} + \frac{1}{2} P_2(\cos\theta) \left[3\rho_{11} - 9\,\rho_{11}|F_o|^2 + 3|F_o|^2 - 1 \right]. \quad (C.3)$$

The expectation value of $P_2(\cos\theta)$ becomes:

$$\langle P_2(\cos\theta) \rangle = \frac{3\,\rho_{11} - 9\,\rho_{11}|F_o|^2 + 3|F_o|^2 - 1}{5} \quad (C.4)$$

$$\rho_{11} = \frac{1}{3} + \frac{5 \langle P_2(\cos\theta) \rangle}{3\,(1 - 3|F_o|^2)} \quad (C.5)$$

Thus equation (C.5) is the same as equation (5.11a).

Similarly, expansion of equation (5.10) for J = 2 and J = 3 leads to 75 and 147 terms respectively. On simplification and integration of these terms, one gets equations (5.11 b-f).

C.2 Decay Angular Distribution of the B Meson for $J^P = 1^+$

The angular distribution of a system γ of angular momentum j and parity P_γ into two particles α and β, with spins s_α, s_β and intrinsic parities P_α, P_β respectively is given by [123]:

$$W(\cos\theta,\phi) = N \sum_{\substack{\lambda_\alpha \geq 0, \lambda_\beta \\ mm'}} |F(\lambda_\alpha,\lambda_\beta)|^2 \, Z^{j\lambda+}_{m,m'}(\theta)\, \mathrm{Re}\,(\rho_{mm'} \exp(i(m-m')\phi)), \quad (C.6)$$

where λ_α and λ_β are the helicities of decay products, m,m' are the angular momentum projections on the z-axis, N is a normalization constant = $\frac{2J+1}{4\pi}$ and $F(\lambda_\alpha,\lambda_\beta)$ is a constant characterizing the decay.

If parity is conserved in the decay

$$F(-\lambda_\alpha, -\lambda_\beta) = P_\alpha P_\beta P_\gamma (-1)^{j-s_\alpha-s_\beta} F(\lambda_\alpha,\lambda_\beta) \quad . \tag{C.7}$$

Following Berman and Jacob [118], the function $Z^{j\lambda\pm}_{mm'}(\theta)$ is given by:

$$Z^{j\lambda\pm}_{mm'}(\theta) = d^j_{m\lambda}(\theta)\, d^j_{m'\lambda}(\theta) \pm d^j_{m,-\lambda}(\theta)\, d^j_{m',-\lambda}(\theta), \tag{C.8}$$

and $\lambda = \lambda_\alpha - \lambda_\beta$

The Z functions are symmetric in m and m'.

The other symmetry is

$$Z_{-m,-m'} = \pm (-1)^{m-m'} Z_{mm'} \tag{C.9}$$

If both α and β have integer spins, then the term in equation (C.6) with $\lambda_\alpha = 0 = \lambda_\beta$ has a coefficient $\frac{1}{2}|F(0,0)|^2$, instead of $|F(\lambda_\alpha,\lambda_\beta)|^2$ for all others. Using the symmetry (C.9), equation (C.6) can be modified with corresponding replacement as given below:

$$\mathrm{Re}\,(\rho_{mm'} \exp(i(m-m')\phi)) = \frac{1}{2}\,\mathrm{Re}\,(\exp(i(m-m')\phi)\,(\rho_{mm'} + (-1)^{m-m'} \rho^*_{-m,-m'})) \tag{C.10}$$

If the quantization axis is chosen in the production plane (i.e., the t- or the s-channel helicity frame), the parity conservation restricts the density matrix elements to

$$\rho_{mm'} = (-1)^{m-m'} \rho_{-m,-m'} \tag{C.11}$$

Then the right-hand side of equation (C.10) becomes $\cos[(m,-m')\phi]\,\mathrm{Re}\rho_{mm'}$, and on substitution this relation in equation (C.6), one gets:

$$W(\cos\theta,\phi) = 3/4\pi \sum_{\substack{\lambda_\alpha \geq 0,\lambda_\beta \\ mm'}} |F(\lambda_\alpha,\lambda_\beta)|^2 \, Z^{j\lambda+}_{mm'}(\theta)\cos((m-m')\phi)\,\mathrm{Re}\rho_{mm'} \qquad (C.12)$$

As $B \longrightarrow \omega\pi$.

Now $\lambda_\alpha = \lambda_\omega = +1,0,-1$ and $\lambda_\beta = \lambda_\pi = 0$;

$P_\alpha = P_\omega = -1$ and $P_\beta = P_\pi = -1$.

Using equation (C.7) one gets:

$$F_{-1} = F_1 \quad \text{and} \quad F_o \neq 0$$

Then equation (C.12) becomes:

$$W(\cos\theta,\phi) = 3/4\pi \sum_{m,m'} \left\{ \left[|F_1|^2 \, Z^{11}_{mm'}(\theta)\cos((m-m')\phi)\,\mathrm{Re}\rho_{mm'} + \tfrac{1}{2}|F_o|^2 \, Z^{10}_{mm'}(\theta)\cos((m-m')\phi)\,\mathrm{Re}\rho_{mm'} \right] \right\} \qquad (C.13)$$

Now $m = 0, \pm1$ and $m' = 0, \pm1$.

Using symmetry relation (C.9) and equation (C.8), one gets:

$$\left.\begin{aligned} Z_{1,-1} &= Z_{-1,1} \\ Z_{1,0} &= Z_{0,1} = -Z_{-1,0} = -Z_{0,-1} \\ Z_{-1,-1} &= Z_{1,1} \end{aligned}\right\} \qquad (C.14)$$

Using relations (C.14) and properties of the density matrix (see Section 2.4.1) in equation (C.13), one gets:

$$\begin{aligned} W(\cos\theta,\phi) = 3/4\pi \Big[& 2|F_1|^2 Z^{11}_{1,-1}(\theta)\cos 2\phi\,\mathrm{Re}\rho_{1,-1} + |F_o|^2 Z^{10}_{1,-1}(\theta)\cos 2\phi\,\mathrm{Re}\rho_{1,-1} \\ & + 4|F_1|^2 Z^{11}_{1,0}(\theta)\cos\phi\,\mathrm{Re}\rho_{1,0} + 2|F_o|^2 Z^{10}_{1,0}(\theta)\cos\phi\,\mathrm{Re}\rho_{1,0} \\ & + |F_1|^2 Z^{11}_{0,0}(\theta)\rho_{00} + \tfrac{1}{2}|F_o|^2 Z^{10}_{0,0}(\theta)\rho_{00} \\ & + |F_1|^2 Z^{11}_{1,1}(\theta)(1-\rho_{00}) + |F_o|^2 Z^{10}_{1,1}(\theta)\frac{1-\rho_{00}}{2} \Big] \end{aligned} \qquad \ldots (C.15)$$

Using relations (C.8) and (C.14) and explicit expressions for $d^{j}_{mm'}$, as given by Brinck and Satchler [124], one gets:

$$\left.\begin{aligned}
Z^{11}_{1,-1}(\theta) &= Z^{11}_{-1,1}(\theta) = 1/2(1-\cos^2\theta) \\
Z^{11}_{1,0}(\theta) &= Z^{11}_{0,1}(\theta) = -Z^{11}_{-1,0}(\theta) = -Z^{11}_{0,-1}(\theta) = \cos\theta\left(\frac{1-\cos^2\theta}{2}\right)^{\frac{1}{2}} \\
Z^{11}_{0,0}(\theta) &= 1 - \cos^2\theta \\
Z^{11}_{1,1}(\theta) &= Z^{11}_{-1,-1}(\theta) = 1/2(1+\cos^2\theta) \\
Z^{10}_{1,-1}(\theta) &= Z^{10}_{-1,1}(\theta) = -(1-\cos^2\theta) \\
Z^{10}_{1,0}(\theta) &= Z^{10}_{0,1}(\theta) = -Z^{10}_{-1,0}(\theta) = -Z^{10}_{0,-1}(\theta) = -2\cos\theta\left(\frac{1-\cos^2\theta}{2}\right)^{\frac{1}{2}} \\
Z^{10}_{0,0}(\theta) &= 2\cos^2\theta \\
Z^{10}_{1,1}(\theta) &= Z^{10}_{-1,-1}(\theta) = 1-\cos^2\theta
\end{aligned}\right\} \quad (C.16)$$

Using relations (C.16) in equation (C.15), one gets:

$$\begin{aligned}
W(\cos\theta,\phi) = 3/4\pi \Big[& |F_1|^2 (1-\cos^2\theta)\cos 2\phi \mathrm{Re}\rho_{1,-1} + |F_o|^2 (-(1-\cos^2\theta))\cos 2\phi \mathrm{Re}\rho_{1,-1} \\
& + 4|F_1|^2 \cos\theta \left(\frac{1-\cos^2\theta}{2}\right)^{\frac{1}{2}} \cos\phi \mathrm{Re}\rho_{1,0} + 2|F_o|^2 \left(-2\cos\theta\sqrt{\frac{1-\cos^2\theta}{2}}\right)\cos\phi \mathrm{Re}\rho_{10} \\
& + |F_1|^2 (1-\cos^2\theta)\rho_{00} + |F_o|^2 \cos^2\theta \rho_{00} \\
& + |F_1|^2 \tfrac{1}{2}(1+\cos^2\theta)(1-\rho_{00}) + |F_o|^2 (1-\cos^2\theta)\left(\frac{1-\rho_{00}}{2}\right) \Big]
\end{aligned} \quad \ldots\ldots \quad (C.17)$$

$$\left.\begin{aligned}
W(\cos\theta,\phi) = 3/4\pi \Big[& (|F_1|^2 - |F_o|^2)(1-\cos^2\theta)\cos 2\phi \mathrm{Re}\rho_{1,-1} \\
& + 4\,(|F_1|^2 - |F_o|^2)\cos\theta\sqrt{\frac{1-\cos^2\theta}{2}}\cos\phi \mathrm{Re}\rho_{1,0} \\
& + \frac{1}{2}\,(1-3\cos^2\theta)\rho_{00}\,(|F_1|^2 - |F_o|^2) \\
& + \frac{1}{2}\,(|F_1|^2 + |F_o|^2) + \frac{1}{2}\cos^2\theta\,(|F_1|^2 - |F_o|^2) \Big]
\end{aligned}\right\} \quad (C.18)$$

Using the normalization $\sum_{\lambda} |F_{\lambda}|^2 = 1$ [115] in equation (C.18), one gets:

$$W(\cos\theta,\phi) = 3/4\pi \left[\frac{1-3|F_o|^2}{4} (1-3\rho_{00})\cos^2\theta + \frac{1}{4}(1+|F_o|^2+\rho_{00}(1-3|F_o|^2)) + \frac{1-3|F_o|^2}{2} (\rho_{1,-1}\sin^2\theta\cos 2\phi+\sqrt{2}\mathrm{Re}\rho_{10}\sin 2\theta\cos\phi) \right] \quad (C.19)$$

Hence equation (C.19) is the same as equation (5.16).

C.3 The |D/S| Ratio

The helicity amplitudes F_{λ} may be expanded in terms of the partial-wave amplitudes [100,125]:

$$|F_{\lambda}| = \sum_{L} \tilde{F}_{L} (2L+1)^{\frac{1}{2}} \langle L0|\lambda|J\lambda\rangle \ , \quad (C.20)$$

where $\tilde{F}_L$ is the L-wave amplitude and $\langle j_1,m_2,j_2,m_2|J,M\rangle$ are the Clebsch-Gordan coefficients.

For the assignment $J^P = 1^+$ for the B meson L = 0 or 2, then one gets:

$$F_{\pm 1} = \tilde{F}_S\langle 0,0|\pm 1|1,\pm 1\rangle + \tilde{F}_D\sqrt{5}\langle 2,0|\pm 1|1,\pm 1\rangle = \tilde{F}_S + \frac{1}{\sqrt{2}}\tilde{F}_D \quad (C.21)$$

$$F_o = \tilde{F}_S\langle 0,0|0|1,0\rangle + \tilde{F}_D\sqrt{5}\langle 2,0|0|1,0\rangle = \tilde{F}_S - \sqrt{2}\,\tilde{F}_D \quad (C.22)$$

$$\tilde{F}_D = \frac{\sqrt{2}}{3}(F_1 - F_o) \quad (a)$$

$$\tilde{F}_S = \frac{1}{3}(2F_1 + F_o) \quad (b) \quad (C.23)$$

Hence equation (C.23) is the same as equation (5.19).

ACKNOWLEDGMENTS

The author's gratitude starts far back —— to his late mother who encouraged and taught him how to write; to his father who saw that he received an education; and to everyone responsible for educating him.

The author wishes to thank Professor G.D. Rochester and Professor A.W. Wolfendale for their encouragement and interest in the work. He wishes to acknowledge his indebtedness to his supervisor Dr. D. Evans for his guidance, assistance and many helpful suggestions. He would like to thank his colleagues in the High Energy Nuclear Physics Group of this University and his collaborators in other Universities for their assistance and for many useful discussions. He expresses his gratitude to Drs. J.V. Major, F.D. Gault, G.F. Pinter, P. Söding and Mr. P.J. Walters for many stimulating discussions.

His thanks are due to the technical staff of the Physics Department, in particular to Mrs. D.C. Pickles and Mrs. J. Gibson for their help in drawing the figures. He would also like to thank the computing staff of this University, in particular Mr. R. Gawley for his assistance in the use of the CERN MINUITS fitting programme.

The research project has been financed by the Science Research Council.

REFERENCES

[1] Particle Data Group, Reviews of Modern Physics, 45, No.2, Part II (1973).

[2] Afzal, M. et al., Nuovo Cimento, 15A, 61 (1973).

[3] Evans, D. et al., Nuclear Physics, B51, 205 (1973).

[4] Lazeyras, P., CERN/TC/Beam 66-7 (1967).

[5] Bernard, P. et al., CERN 68-29 (1968).

[6] Ronne, B., CERN 64-13, Vol.I (1964).

[7] Hahn, B. et al., Proceedings of the International Conference on Instrumentation for High Energy Physics, Interscience Publishers, N.Y., 1961, p.143.

[8] Biswas, N.N. et al., Nuclear Instruments and Methods, 20, 135 (1963).

[9] Fabian, B.N. et al., Review of Scientific Instruments, 34, 484, (1963).

[10] Pearson, G.E., Ph.D. Thesis, Durham University (1969).

[11] Foley, K.J. et al., Physical Review Letters, 19, 330 (1967).

[12] Jackson, J.D., Nuovo Cimento, 34, 1664 (1964).

[13] Davis, P.J. et al., Physical Review Letters, 23, 1071 (1969).

[14] Particle Data Group, Reviews of Modern Physics, 43, No.2, Part II (1971), pp.90-91.

[15] Koch, W., CERN 64-13, Vol. II (1964).

[16] Donohue, J.T., and Högaasen, H., Physics Letters, 25B, 554 (1967).

[17] Gottfried, K., and Jackson, J.D., Nuovo Cimento, 33, 309 (1964).

[18] Gottfried, K., and Jackson, J.D., Physics Letters, 8, 144 (1964).

[19] Trieman, S.B., and Yang, C.N., Physical Review Letters, 8, 140 (1962).

[20] Kotanski, A., Acta Physica Polonica, 29, 699 (1966).

[21] Kotanski, A., Acta Physica Polonica, 30, 629 (1966).

[22] Schmitz, N., CERN 65-24, Vol.I (1965).

[23] Montanet, L., CERN 67-23, (1967).

[24] Jackson, J.D., Reviews of Modern Physics, 37, 484 (1965).

[25] Mandelstam, S., Physical Review, 112, 1344 (1958).

[26] Mandelstam, S., Physical Review, 115, 1741 (1959).

[27] Jackson, J.D., Reviews of Modern Physics, 42, 12 (1970).

[28] Goebel, C., Physical Review Letters, 1, 337 (1958).

[29] Chew, G.F., and Low, F.E., Physical Review, 113, 1640 (1959).

[30] Jackson, J.D., and Pilkuhn, H., Nuovo Cimento, 33, 906 (1964).

[31] Jackson, J.D., and Pilkuhn, H., Nuovo Cimento, 34, 1841 (1964).

[32] Stodolsky, L., and Sakurai, J.J., Physical Review Letters, 11, 90 (1963).

[33] Stodolsky, L., Physical Review, 134B, 1099 (1964).

[34] Pilkuhn, H., and Svensson, B.E.Y., Nuovo Cimento, 38, 518 (1965).

[35] Regge, T., Nuovo Cimento, 14, 951 (1959).

[36] Regge, T., Nuovo Cimento, 18, 947 (1960).

[37] Gell-Mann, M., Physics Letters, 8, 214 (1964).

[38] Lynch, G., UCRL, 10335 (1962).

[39] Foelsche, H.W.J. et al., Physical Review, 134B, 1138 (1964), at 1.04, 1.22 and 1.39 GeV/c.

[40] Daronian, P. et al., Nuovo Cimento, 41A, 503 (1966), at 1.58 GeV/c.

[41] Johnson, J.A. et al., Bulletin of the American Physical Society, 9, 70 (1964), at 1.65 GeV/c.

[42] James, F.E. et al., Physical Review, 142, 896 (1966) at 2.08 GeV/c.

[43] Alff-Steinberger, C. et al., Physical Review, 145, 1072 (1966), at 2.35, 2.62 and 2.9 GeV/c.

[44] Armenise, N. et al., Nuovo Cimento, 37, 361 (1965), at 2.75 GeV/c.

[45] Yamamoto, S.S. et al., Physical Review, 140B, 730 (1965), at 2.77 GeV/c.

[46] Abolins, M. et al., Physical Review Letters, 11, 381 (1963), at 3.43 and 3.54 GeV/c.

[47] Goldhaber, G. et al., Physical Review Letters, 12, 336 (1964), at 3.65 GeV/c.

[48] Pless, Vienna Conference, 735 (1968), at 3.9 GeV/c as quoted in Reference [57].

[49] Aderholz, M. et al., Physical Review, 138B, 897 (1965), at 4 GeV/c.

[50] Slattery, P. et al., Nuovo Cimento, 50A, 377 (1967), at 7 GeV/c.

[51] Aderholz, M. et al., Nuclear Physics, B8, 45 (1968), at 8 GeV/c.

[52] Kung, Nevis Cyclotron Lab., Columbia University, 171 (1969), at 8.5 GeV/c as quoted in Reference [57].

[53] Bruckner, Vienna Conference, 327 (1968), at 11.0 GeV/c as quoted in Reference [57].

[54] Ballam, J. et al., Bulletin of the American Physical Society, 13, 612 (1968), at 16 GeV/c.

[55] Ballam, J. et al., Physical Review, D3, 2606 (1971), at 16 GeV/c.

[56] Hones, M.J. et al., Physical Review, D2, 827 (1970), at 18.5 GeV/c.

[57] Flaminio, E. et al., CERN/HERA 70-5 (1970).

[58] Goldhaber, G., CERN 67-27, Vol. III (1967).

[59] Shen, UCRL 1617, at 3.65 GeV/c as quoted in Reference [57].

[60] Aderholz, M. et al., Nuclear Physics, B14, 255 (1969), at 8 GeV/c.

[61] Rabin, State University, Rutgers (1967), at 8.5 GeV/c as quoted in Reference [57].

[62] Gelfand, Columbia University, at 2.62 GeV/c as quoted in Reference [57].

[63] Armenise, N. et al., Nuovo Cimento, 40A, 273 (1965), at 2.75 GeV/c.

[64] Brown, D. et al., Physical Review Letters, 19, 664 (1967), at 2.95, 3.2, 3.5, 3.75 and 4.08 GeV/c.

[65] Trilling, G.H. et al., Physics Letters, 19, 427 (1965), at 3.65 GeV/c.

[66] Abrams, G.S. et al., Physical Review Letters, 25, 617 (1970).

[67] Aderholz, M. et al., Nuovo Cimento, 35, 659 (1965), at 4.0 GeV/c.

[68] Pols, C.L. et al., Nuclear Physics, B25, 109 (1970), at 5 GeV/c.

[69] Böckmann, K. et al., Nuclear Physics, B7, 681 (1968), at 5 GeV/c.

[70] Bloodworth, I.J. et al., Nuclear Physics, B35, 79 (1971), at 5.45 GeV/c.

[71] Ferbel, Rochester University, 875, 153 (1966), at 7 GeV/c as quoted in Reference [57].

[72] Biswas, N.N. et al., Physical Review, D2, 2529 (1970), at 18.5 GeV/c.

[73] Coyne, D.G. et al., Nuclear Physics, B32, 333 (1971).

[74] Morrison, D.R.O., Physics Letters, 22, 528 (1966).

[75] Hensen, J.D. et al., Nuclear Physics, B25, 605 (1971).

[76] Morrison, D.R.O., CERN/D.Ph. II/PHYS 71-10.

[77] Minnaert, P., Physical Review, 151, 1306 (1966).

[78] Minnaert, P., Physical Review Letters, 16, 672 (1966).

[79] Ader, J.P. et al., Nuovo Cimento, A56, 952 (1968).

[80] Jacob, M., and Wick, G.C., Annals of Physics, 7, 404 (1959).

[81] Kotanski, A., and Zalewski, K., Nuclear Physics, B4, 559 (1968).

[82] Kotanski, A., and Zalewski, K., Nuclear Physics, B20, 236 (1970).

[83] Donohue, J.T., Nuovo Cimento, 52A, 1152 (1967).

[84] Van, J.T.T. (ed.), Martin, A.D., Proceedings of the 1972 Recontre de Moriond, (1972), p.439.

[85] Van, J.T.T., Lettere Al Nuovo Cimento, 3, 678 (1970).

[86] Kajantie, K. et al., Nuclear Physics, B13, 437 (1969).

[87] Svensson, B.E.Y., Nuovo Cimento, 37, 714 (1965).

[88] Gottfried, K., and Jackson, J.D., Nuovo Cimento, 34, 735 (1964).

[89] Gottfried, K., and Jackson, J.D., Nuovo Cimento, 34, 1843 (1964).

[90] Jackson, J.D. et al., Physical Review, 139B, 428 (1965).

[91] LE Bellac, M., and Plaut, G., Lettere Al Nuovo Cimento, 1, 721 (1969).

[92] Högassen, H. et al., Physics Letters, 26B, 166 (1968).

[93] Jones, L., Physical Review, 163, 1530 (1967).

[94] Bialas, A., and Zalewski, K., Nuclear Physics, B6, 465 (1968).

[95] Goldhaber, G. et al., Physical Review Letters, 23, 1351 (1969).

[96] Armenise, N. et al., Nuovo Cimento, 65A, 637 (1970).

[97] Gidal, G. et al., UCRL - 17984 (1967), at 3.07, 3.5, 3.75 and 4.05 GeV/c as quoted in Reference [57].

[98] Aderholz, M. et al., Physics Letters, 10, 226 (1964).

[99] Klein, P.R. et al., Physical Review, 150, 1123 (1966), at 2.7 GeV/c.

[100] Chung, S.U. et al., Physical Review, 165, 1491 (1968), at 3.2 and 4.2 GeV/c.

[101] Erofeev, I.A. et al., Soviet Journal of Nuclear Physics, 11, 450 (1970), at 3.25 GeV/c.

[102] Lee, Y.Y. et al., Physical Review, 159, 1156 (1967), at 3.63 GeV/c.

[103] Miyashita, S. et al, Physical Review, D1, 771 (1970), at 6.7 GeV/c.

[104] Cason, N.M. et al., Physical Review, D1, 851 (1970), at 8 GeV/c.

[105] Caso, C. et al., Lettere Al Nuovo Cimento, 3, 707 (1970), at 11.2 GeV/c.

[106] Baltay, C. et al., Physical Review Letters, 18, 93 (1967).

[107] Bizzari, R. et al., Nuclear Physics, B14, 169 (1969).

[108] Donald, R.A. et al., Nuclear Physics, B11, 551 (1969).

[109] Diaz, J. et al., CERN/D.PR II/Phys. 72-9.

[110] Bondar, L. et al., Physics Letters, 5, 209 (1963).

[111] Maor, U. et al., Physics Letters, 15, 281 (1965).

[112] Deck, R.T., Physical Review Letters, 13, 169 (1964).

[113] Goldhaber, G. et al., Physical Review Letters, 15, 118 (1965), at 3.65 GeV/c.

[114] Chung, S.U. et al., Physical Review Letters, 16, 481 (1966).

[115] Ascoli, G. et al., Physical Review Letters, 20, 1411 (1968).

[116] Lipkin, H.J., Physical Review, 159, 1303 (1967).

[117] Werbrouck, A. et al., Lettere Al Nuovo Cimento, 4, 1267 (1970).

[118] Berman, S.M., and Jacob, M., Physical Review, 139B, 1023 (1965).

[119] Satterblom, P.H. et al., Physical Review, 134B, 207 (1964).

[120] Morrison, D.R.O., Physical Review, 165, 1699 (1968).

[121] Morrison, D.R.O., Physics Letters, 22, 226 (1966).

[122] Morrison, D.R.O., Physics Letters, B25, 238 (1967).

[123] De Witt, C., and Jacob, M. (eds.), Jackson, J.D., High Energy Physics, Gordon and Breach Science Publishers, London, 1965.

[124] Brink, D.M., and Satchler, G.R., Angular Momentum, Clarendon Press, Oxford, 1968.

[125] Ballam, J. et al., Physical Review, D1, 94 (1970).

[126] Chung, S.U. et al., BNL 18340 (1973) (Preprint).

[127] Armenise, N. et al., Lettere Al Nuovo Cimento, 8, 425 (1973).

[128] Frenkiel, P. et al., Nuclear Physics, B47, 61 (1972).